KU LEUVEN

ARENBERG DOCTORAL SCHOOL
Faculty of Sciences

Stability of Bimetallic Clusters and Development of a Magnetic Deflection Setup

Nguyen Thanh Tung

Supervisors:

Prof. dr. P. Lievens, supervisor
Prof. dr. E. Janssens, co-supervisor
Prof. dr. M. J. Van Bael, co-supervisor

Dissertation presented in partial fulfillment of the requirements for the degree of Doctor in Science

May 2014

Stability of Bimetallic Clusters and Development of a Magnetic Deflection Setup

Nguyen Thanh TUNG

Supervisory Committee:
Prof. dr. K. Temst, chair
Prof. dr. P. Lievens, supervisor
Prof. dr. E. Janssens, co-supervisor
Prof. dr. M. J. Van Bael, co-supervisor
Prof. dr. M. T. Nguyen, jury
Prof. dr. H. De Gersem, jury
Prof. dr. K. Hansen, external jury
Prof. dr. V. D. Lam, external jury

Dissertation presented in partial
fulfillment of the requirements for
the degree of Doctor
in Science

May 2014

Geel Huis, Kasteelpark Arenberg 11 - bus 2100, 3001 Leuven (Belgium)

D/2014/10.705/16
ISBN 978-90-8649-707-2

Acknowledgments

About four years ago, I was inspired by Prof. Peter Lievens and Prof. Ewald Janssens to join in a project that pursuing the showing-up of the smallest Kondo-like systems. And it turned out to be a fantastic adventure with tiny particles and a big machine. Within few sentences, it for sure is unable to express those long days spent in the lab, battling shoulder to shoulder with my colleagues, the joy for experiments, the hope for good results, and also the sadness for failed attempts. However, I do hope to take this opportunity for expressing my thanks to many people that without them, this thesis would not have been possible.

First and foremost, I would like to thank my beloved parents for their endless love and great care to me. Thank you for giving me my life and everything of which I can be here today to write all of this for a reason.

I would like to thank my supervisors: Prof. Peter Lievens, Prof. Ewald Janssens, and Prof. Margriet Van Bael. It cannot be argued with that the most influential person to this thesis is Peter. His inspiration and guidance have been indispensable to my growth as a scientist over these past four years. Whatever the reason of why you offered me this opportunity, I would thank you for believing in me, even if it was only the first moment. I am especially grateful to Ewald for his devotion to his students' education and success, and to Margriet for her warmest encouragement and constant support. I am very proud of studying under your tutelage.

I am especially indebted to my thesis committee members: Prof. Kristiaan Temst, Prof. Minh Tho Nguyen, Prof. Herbert De Gersem, Prof. Klavs Hansen, and Prof. Vu Dinh Lam, who have been very gracious and generous with their time, ideas, and advices.

I would like to acknowledge the HRTOF, a home-built mass spectrometer, for your essential support in thousands of experiments. You might be just a hard-to-please machine to someone else, but to me, you are an extension of my being. Without you, it is hard to be me today.

It would be a great regret if I do not jump at this chance to express my deep gratitude to Soumen Bhattacharyya for helping me to speed up with photofragmentation experiments, and Jorg De Haeck for sharing a plenty of experiences in the mass spectrometry with me. I also thank Tam Nguyen Minh and Bert Masschaele for your fruitful collaboration.

I would like to express my acknowledge to the best administrative and technical staffs I have ever met: Liliane Goffin, Monique Van Meerbeek, Philippe Mispelter, Philippe Muylaert, Philip de Greef, Stijn Vandezande, and Lucien Coekaerts, for making the annoying parts of lab life running more smoothly. I must also extend my thanks to the current and former CLASS members: Vladimir, Kenneth, Milan, Yejun, Kelly, Tobias, Zhe ... who have made my years at Leuven unforgettable.

I would thank my sister, Nguyen Le Minh Tam, for her constant love and care to me. I would also like to thank Le Ngoc, Nguyen Thanh Nga, and Ha Minh Anh for not only sharing beautiful moments but also supporting me through difficulties. A special thank to Hai Thuy Le for being a true friend over the years. There also is a long list of my close friends and colleagues, whether old or new, far away or nearby, to feel their encouragement to my life. I cannot thank you enough.

Tung,
May 2014

Abstract

In macroscopic physics, many properties of bulk materials are usually independent of the sample size. Nature, however, reveals a not only different but also fascinating picture of the world of atomic clusters, that are made up by tiny pieces of matter containing up to several thousands of atoms: adding or removing one atom from a cluster changes its properties dramatically. The motivation behind cluster research arises, on one hand, from fundamental interest in the evolution of physical properties from a single atom to the solid-state limit, and on the other hand, from the desire of using smaller and smaller structures for technological applications.

From the beginning of the 1980s, numerous exciting cluster properties, which change non-monotonically with the number and type of constituent atoms, have been revealed. In our group, the size- and composition-dependent properties of different cluster systems have been investigated using mass spectrometric and laser spectroscopic techniques. My Ph.D. research has been inspired by the long-term goal of designing and synthesizing particularly stable binary cluster species composed of ferromagnetic metals, which can be used as functional building blocks for novel nanostructured materials. In the first goal of this work, we have systematically studied the changes on bonding, stability, and structure of bimetallic cluster systems, by carefully manipulating the cluster size as well as constituent. The second goal is devoted to designing and constructing a novel magnetic deflection apparatus, which enables to detect and measure the magnetic properties of ferromagnetic clusters from few to several tens of atoms.

In particular, size- and composition-dependent stabilities of bimetallic (Pb_nAl^+, Co_nTM^+, with $n = 7 - 18$ and TM = Ti, V, Cr, Mn) and bimetallic oxide ($Co_{n-1}CrO_m^+$ with $n = 1 - 4$ and $m = 2 - 8$) clusters are studied in the molecular beam. The clusters are produced by a laser vaporization source and mass-selectively photofragmented by laser light to examine their dissociation behavior, stability, and bond strength. Relative stabilities of clusters are extracted from size-dependent photofragmentation spectra. Constraints imposed by the theory of unimolecular decay combined with the measured laser fluence-dependent photofragmentation spectra are used to bracket dissociation energies. Density functional theory is applied to predict the cluster structures and to calculate dissociation energies for different evaporation channels of oxide species.

We found that the smallest Pb_nAl^+ ($n = 7 - 11$) clusters favor atomic Pb evaporation, whereas the preferred dissociation pathway of the larger ones involves Pb_2 and Pb_3 fragments. For Co_nTM^+ clusters, the evaporation of a cobalt atom is the most facile dissociation channel for Ti and V doped species. In contrast, for TM = Cr and Mn the split-off of the dopant atom is seen to be the preferred dissociation channel with an exception of $Co_{13}Cr^+$. It indicates an enhanced stability of the doped clusters over the pure ones except for Cr and Mn dopants. This is explained by the differences between heterogeneous and homogeneous bond dissociation energies. Notably, the theoretically believed icosahedral $Pb_{12}Al^+$, $Co_{12}V^+$, and $Co_{12}Cr^+$ clusters are exceptionally stable among the studied species, which is in good agreement with previous mass spectroscopic discoveries. For oxide species, substitution of a Co by a Cr atom alters the dissociation behavior of pure cobalt oxide clusters. $Co_2O_2^+$, $Co_4O_3^+$, $Co_4O_4^+$, and $CoCrO_2^+$ are found to be particularly stable.

The study of the size- and constituent-dependent magnetism of bimetallic clusters needs an appropriate experimental technique. The second goal of this thesis is the development of a Stern-Gerlach magnetic deflection experiment in which the free clusters interact with an applied inhomogeneous magnetic field. The magnetic properties of clusters can be determined from the deflection with regard to the original beam trajectory. The Stern-Gerlach magnetic deflection system consists of a beam chopper, a dual-stage collimator system, a Stern-Gerlach magnet, a drift tube, and a position sensitive detector. The chopper wheel is used to measure the cluster velocity. Two collimators define a beam shape of 0.3×3.0 mm^2. The collimated beam is deflected in the magnet and has a free flight before entering the extraction. Information on cluster size distribution and deflection is measured by the position-sensitive detector installed in the high resolution time-of-flight mass spectrometer. Analytical calculations and extensive simulations have been carried out to understand the magnet performance and to optimize the beam deflection. A magnetic deflection measurement has been demonstrated for Cr atoms.

Beknopte samenvatting

De meeste fysische eigenschappen van bulk materialen zijn schaalbaar met de grootte van het sample. In de fascinerende wereld van atomaire clusters, kleine materiedeeltjes bestaande uit maximaal enkele duizenden atomen, gedraagt de natuur zich totaal anders: het toevoegen of verwijderen van één enkel atoom wijzigt de eigenschappen op discontinue wijze. Clusteronderzoek is enerzijds gemotiveerd vanuit een fundamentele interesse in de evolutie van fysische eigenschappen met de afmetingen van materiedeeltjes (van één enkel atoom tot bulkmaterialen) en anderzijds vanuit micro- en nanotechnologische toepassingen waarin steeds kleinere en kleinere structuren gebruikt worden.

Onderzoek vanaf het begin van de jaren 1980 toont aan dat de eigenschappen van clusters op een niet-monotone wijze veranderen met het aantal en de aard van de samenstellende atomen. In onze onderzoeksgroep worden grootte- en samenstellingsafhankelijke eigenschappen van verschillende soorten clusters onderzocht met behulp van massaspectrometrie en laserspectroscopische technieken. Mijn doctoraatsonderzoek is geïnspireerd door de ambitie om stabiele binaire clusters te creëren uit ferromagnetische metalen die kunnen dienen als functionele bouwstenen voor nieuwe nanogestructureerde materialen. De eerste doelstelling van dit werk betreft een systematische studie van de chemische binding, stabiliteit en structuur van bimetallische clusters door het gecontrolleerd wijzigen van de grootte en de compositie van de clusters. Een tweede doelstelling betreft het ontwerpen en bouwen van een apparaat voor magnetische deflectie-experimenten op clusters. Dit apparaat zal het mogelijk maken om de magnetische eigenschappen van ferromagnetische clusters bestaande uit enkele tot enkel tientallen atomen op te meten.

In deze thesis worden de grootte- en samenstellingsafhankelijke stabiliteiten van bimetallische ($\mathrm{Pb}_n\mathrm{Al}^+$, $\mathrm{Co}_n\mathrm{TM}^+$, met $n = 7 - 18$ en TM = Ti, V, Cr, Mn) en bimetaaloxide ($\mathrm{Co}_{n-1}\mathrm{CrO}_m^+$ met $n = 1 - 4$ en $m = 2 - 8$) clusters in

een moleculaire bundel bestudeerd. De clusters worden geproduceerd met een laservaporisatiebron, massageselecteerd, en gefotofragmenteerd door middel van laserlicht om hun dissociatiegedrag en hun stabiliteit te onderzoeken. Relatieve stabiliteiten van de clusters worden bekomen uit de grootte-afhankelijke fotofragmentatiespectra. Interpretatie op basis van statische theorieën voor unimoleculaire dissociatie laten toe uit fotofragmentatiespectra, opgemeten als functie van de laserflux, boven- en ondergrenzen te bepalen voor de dissociatie-energie. Dichtheidsfunctionaaltheorie werd gebruikt om de geometrische structuren van de bimetaaloxide clusters te voorspellen. Ook het energetisch meest voordelige dissociatiekanaal werd berekend. We vonden experimenteel dat de kleinste $\mathrm{Pb}_n\mathrm{Al}^+$ ($n = 7 - 11$) clusters preferentieel fragmenteren via de verdamping van een Pb atoom, terwijl voor grotere clusters de evaporatie van Pb_2 en Pb_3 waargenomen werd. Voor $\mathrm{Co}_n\mathrm{TM}^+$ clusters met TM = Ti en V is de evaporatie van een kobaltatoom het energetisch meest voordelige dissociatiekanaal. Daarentegen, voor clusters gedopeerd met Co en Mn (met uitzondering van $\mathrm{Co}_{13}\mathrm{Cr}^+$) is de verdamping van het doperingsatoom het meest waarschijnlijk. Deze experimenten tonen aan dat de stabiliteit van kobaltclusters verhoogd wordt bij dopering met Ti en V, maar verlaagd wordt bij dopering met Cr en Mn. Deze observaties zijn in overeenstemming met de verschillen tussen de bindingsenergieën van de overeenkomstige homogene en heterogene dimeren. Er kan ook opgemerkt worden dat de theoretisch veronderstelde uitzonderlijke stabiliteit van de icosahedrale $\mathrm{Pb}_{12}\mathrm{Al}^+$, $\mathrm{Co}_{12}\mathrm{V}^+$ en $\mathrm{Co}_{12}\mathrm{Cr}^+$ clusters in goede overeenstemming is met de massaspectroscopische waarnemingen. Voor de bimetaaloxideclusters vinden we dat substitutie van één enkel kobaltatoom door één enkel chromiumatoom het dissociatiegedrag van de kobaltoxideclusters beïnvloedt. Er werd eveneens ontdekt dat $\mathrm{Co}_2\mathrm{O}_2^+$, $\mathrm{Co}_4\mathrm{O}_3^+$, $\mathrm{Co}_4\mathrm{O}_4^+$, en CoCrO_2^+ clusters meer stabiel zijn dan andere samenstellingen.

Om de grootte- en samenstellingsafhankelijke magnetische momenten van bimetallische clusters te bestuderen is een daartoe speciaal ontwikkeld apparaat nodig. Het tweede doel van dit proefschrift was dan ook het ontwikkelen van een magnetische deflectie-opstelling waarin clusters in een moleculaire bundel kunnen interageren met een inhomogeen magnetische veld. De magnetische eigenschappen van de clusters worden bepaald uit hun afbuiging ten opzichte van de oorspronkelijke richting van de moleculaire bundel. Deze opstelling bestaat uit een vliegwiel, twee collimatoren, en magneet waarvan het magnetisch veld met sterke gradiënt heeft, een driftbuis en een positiegevoelige detector. Het vliegwiel wordt gebruikt om de snelheid van de clusters te bepalen. De collimatoren definiëren de vorm van de clusterbundel: $0.3 \times 3.0\ \mathrm{mm}^2$. De clusters die afgebogen worden in de magneet vliegen door een veldvrije vluchtbuis alvorens geëxtraheerd te worden in de vluchttijdmassaspectrometer. Informatie over verdeling van de clustergroottes en over de magnetische deflectie wordt simultaan op gemeten door een positiegevoelige detector die zich aan het einde van de hoge-resolutie vluchttijdmassaspectrometer bevindt. Analytische berekeningen en elektromagnetische simulaties werden uitgevoerd om de werking van de magneet te begrijpen en om de eigenschappen te optimaliseren. De magnetische veldgradiënt van de nieuwe magneet werd gecalibreerd door het opmeten van de afbuiging van een bundel chromiumatomen.

Abbreviations

BCC	body centered cubic
BNC	bayonet nut coupling
DE	dissociation energy
DFT	density functional theory
DLD	delay-line detector
FEMM	finite element method magnetics
FWHM	full width at half maximum
IP	ionization potential
HCP	hexagonal closed packed
HOMO	highest occupied molecular orbital
HRTOF	high resolution time-of-flight
HRTOF/MS	high resolution time-of-flight mass spectrometer
LOMO	lowest unoccupied molecular orbital
MCP	micro-channel plate
MES	minimum-energy structure
PIL	positioning ionization laser
PSTOF/MS	position-sensitive time-of-flight mass spectrometer
TM	transition metal
TOF	time-of-flight
TOF/MS	time-of-flight mass spectrometer
TTL	transistor-transistor logic
UHV	ultra high vacuum

Contents

List of Figures

List of Tables

Chapter 1

Stability and magnetism of metal clusters

1.1 Introduction

A metal cluster consists of a countable number of atoms that show metallic behavior in bulk. Due to the large fraction of surface atoms, and because of quantum size effects, the properties of metal clusters evolve non-monotonically with size [1]. Small metal clusters often have all atoms on the surface. The electronic and geometric structures of clusters strongly depend upon the number of atoms. For large metallic clusters, the HOMO-LUMO energy gap becomes smaller. The cluster tends to minimize the surface area, having close-packing geometry to increase the coordination. For intermediate sizes, the cluster size evolution of metal clusters behaves differently for different metals, e.g., simple (or noble) and transition metal clusters. When the clusters are embedded into a matrix, it is expected that interesting properties are introduced but additional complexities also appear. Hence, understanding the properties of isolated clusters in the gas phase, in absence of substrate or ambient interactions, is a crucial step towards the applicability of embedded or deposited clusters.

As a matter of fact, gas phase clusters composed of few atoms were produced for the first time by Robbins and co-workers in 1967, giving birth to the very rich field of cluster physics nowadays [2]. However, one had to wait for nearly twenty years, until 1984, to observe the first strikingly size-dependent properties of gas phase clusters, when Knight's group presented the mass spectrum of alkali

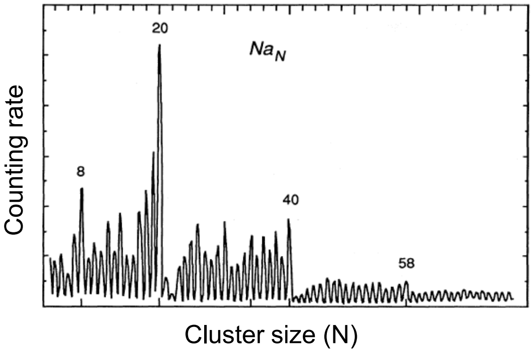

Figure 1.1: *Sodium cluster abundance spectrum* [3].

metal clusters with up to 100 atoms. As shown in Fig. 1.1, the cluster sizes with enhanced abundances (2, 8, 20, 40, 58 ...) reflect free electrons confined in a spherical potential well [3,4]. After those early discoveries, the electronic shell structure was detected in many simple metal cluster systems and experimentally verified by different electronic responses [5]. The electronic shell model was also studied intensively to develop a higher level of accuracy [6].

On the other hand, clusters composed of transition metal atoms deliver a different picture. Valence electrons are no longer free and confined in a potential well since the partially occupied *d* electrons are quite localized, prevailing the observation of a simple electronic shell structure. The stability of these clusters is governed by the geometric packing or the shells of atoms, resembling the magic numbers of rare gas clusters (13, 55, 147 ...) [7,8].

While the earlier work mainly concentrated on elemental clusters, later alloy species have been studied extensively in the search for novel nanostructured materials. Well controllable (e.g., size and composition) production techniques in combination with the knowledge of shell models allow to design and manipulate clusters with not only enhanced stabilities but also other interesting physical properties, e.g., enhanced magnetism, or optical, chemical properties of clusters. This can be fundamentally achieved by doping. The dopant atoms are introduced to stimulate structural transformation or to alter the number of valence electrons. In this regard, numerous investigations of different heterogeneous bonding mechanisms have been carried out. For example, doping electronegative elements

(O, C) or metal atoms (Al) into metal (Li, Al, Pb) clusters shows that the dopant occupies a central position and enhances stability of the clusters [9]. The impurity *d* electrons are proven to be important in the unusual stability of Au_5X^+ (X = V, Cr, Mn, Fe, Co, Zn) systems [10], which cannot be explained by spherical shell models. Transition metal doped gold and silicon clusters are studied with mass spectrometry and infrared spectroscopy, showing that the clusters have an endohedral cage structure [11]. Magnetic moments of MnCo, VCo, BiCo, TeDy, BiDy, and BiMn clusters have been measured using the Stern-Gerlach deflection method [12-15]. The average moments per atom of several species are found to surprisingly increase with dopant concentration, in contrast to their bulk values.

In the following section, we will provide the basic interpretations for experimental observations of size- and dopant-dependent cluster stability. Section 1.3 deals with the experimental aspect and historical overview of cluster magnetism. In section 1.4, recent achievements and, also, challenges in cluster research with the emergence of binary clusters are presented. In the last section, the objectives of this thesis are given.

1.2 Cluster stability

1.2.1 Electronic shell structure

As presented in Fig. 1.1, the mass-abundance spectrum of sodium Na_N clusters shows striking steps at $N = 8$, 20, 40, 58. It suggests that to the lowest order the single valence $3s$ electron of each Na atom in the sodium clusters is delocalized and confined in a potential well. The finite size of the clusters and that of the potential wells results in different electronic shells. Clusters with specific sizes containing a certain amount of itinerant electrons corresponding to filled electronic shells are more stable than others. These are named magic sizes. When adding or subtracting one atom, the stability of magic size clusters is reduced, which is reflected by the reduced abundance in the recorded mass spectra.

Shell structure in spherical clusters

The size dependent properties of simple metal clusters can be explained by a phenomenological shell model, where delocalized valence electrons are bound

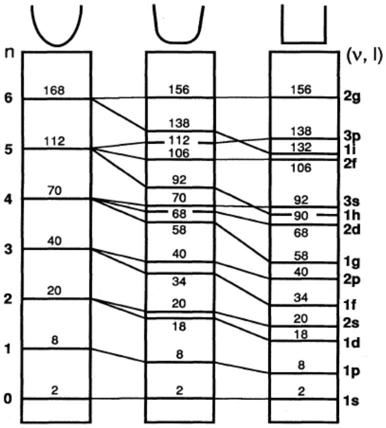

Figure 1.2: *Energy-level occupations for spherical three dimensional harmonic, intermediate, and square-well potentials* [16].

in a spherically symmetric potential well [3]. The effective single particle Hamiltonian for electrons with mass m moving in a three dimensional isotropic oscillator potential is:

$$H = \frac{p^2}{2m} + \frac{m\omega_0^2 r^2}{2} - U\hbar\omega_0[l^2 - n(n+3)/2] \tag{1.1}$$

where p and r are single-electron momentum and coordinate operators, ω_0 is the oscillator frequency, l is the angular momentum operator, and n is the shell number. The parameter U has to be adjusted to fit the experimental observations. The first term represents the kinetic energy of electrons, and the second term is a simple harmonic potential. The third term is an anharmonic correction constructed to modify the shape of the potential while keeping the average shell energy constant. The energy eigenvalue spectrum obtained by solving Eq. 1.1 is:

$$E_n = h\omega_0(n + 3/2) - U[l^2 - n(n+3)/6] \tag{1.2}$$

Figure 1.2 displays energy levels with different U in units of $h\omega_0$. $\nu = (n-l+2)/2$ is a quantum number of the modified spherical potentials. Varying U from 0 to 0.1 effectively flattens the bottom of the potential well, reproducing the level structures of various wells (i.e., from harmonic to square shape). For a square

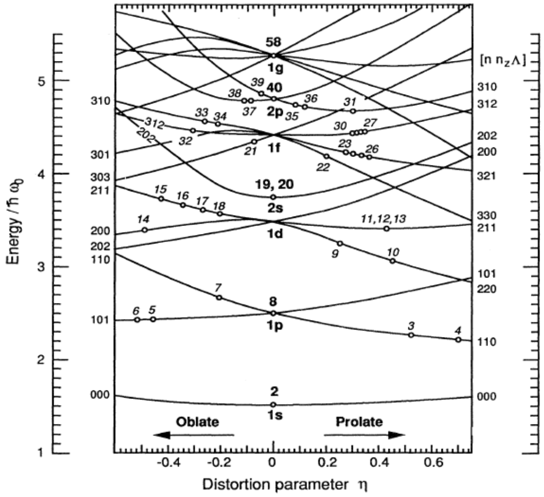

Figure 1.3: *Clemenger-Nilsson diagram* [4]. *Cluster numbers N are positioned at the highest occupied levels and at the equilibrium configuration* η (see text also).

potential well this leads to the following shell sequence:

$$1s^2 1p^6 1d^{10} 2s^2 1f^{14} 2p^6 1g^{18} 2d^{10} 1h^{22} 3s^2 2f^{14} 1i^{26} 3p^6 ... \tag{1.3}$$

The superscript indicates the degeneracy of each energy level. The shell sequence is in agreement with the main features of the abundance pattern of sodium clusters. As these shells are filled, clusters containing 2, 8, 20, 40, ... electrons become very stable. Practically, assuming $U = 0$ is a reasonable approximation for small clusters containing less than 20 atoms.

The ellipsoidal Clemenger-Nilsson shell model

While the spherical shell model can well describe the major abundance steps of closed shell structures, it is not valid for open-shell clusters. From the Jahn-Teller theorem [17], the open-shell clusters are unstable towards distortions. The spherical shell model is unable to explain the fine structure observed in the mass spectrum of sodium clusters (see Fig. 1.1). Clemenger introduced a deformable potential well [4], adapted from the Nilsson model [18], that is particularly well suited to describe this effect. The basic idea behind the Clemenger-Nilsson deformation shell model is that for a fixed volume, the cluster shape will be adjusted to minimize the total electronic energy. Possible deformations are changing the geometry from a sphere to an ellipsoid. Then the single particle Hamiltonian can be written as

$$H = \frac{p^2}{2m} + \frac{1}{2} m\omega_0^2 (\Omega_\perp^2 r^2 + \Omega_z^2 z^2) - U\hbar\omega_0 [l^2 - n(n+3)/2] \tag{1.4}$$

where z is the axis of the ellipsoidal symmetry while $r^2 = x^2 + y^2$. The scaling factors $\Omega_\perp$ and Ω_z can be expressed in terms of a deformation parameter η:

$$\Omega_\perp = \left(\frac{2+\eta}{2-\eta}\right)^{1/3} \qquad \Omega_z = \left(\frac{2+\eta}{2-\eta}\right)^{-2/3} \tag{1.5}$$

with the volume constraint $\Omega_\perp^2 \Omega_z = 1$. If $\Omega_\perp = \Omega_z$, Eq. 1.4 reduces to the spherical problem. For $\Omega_\perp \neq \Omega_z$, subshells are formed and features appear at N = 4, 6, 14, 18, 26, 30, 34, 50, 54, 68 ... Figure 1.3 is the Clemenger-Nilsson diagram, which shows the single particle energies as a function of η for $U = 0.04$. The total energy of the cluster can be represented in terms of the single particle energies. For a harmonic single particle potential, the total electronic energy of a N-atom cluster is a sum of the single particle energies

$$E_{total}(\eta, N) = \frac{3}{4} \sum_{i=1}^{N} E_i(\eta, n_x, n_y, n_z) \tag{1.6}$$

where n_x, n_y, and n_z are the harmonic-oscillator quantum numbers [i.e., for the 1s state, (n_x, n_y,n_z)=(0,0,0); for 1p state, they are (1,0,0), (0,1,0), and (0,0,1), etc]. The resulting total energy curve has a minimum at $\eta_0(N)$ and is indicated by a dot at the highest occupied level in the diagram. By this procedure, one obtains spherical geometries for closed-shell clusters ($\eta = 0$) and oblate or prolate spheroids for open-shell ones. The energy levels of a specific cluster can be obtained by drawing a vertical line through $\eta_0(N)$. The interceptions with the energy-level curves correspond to the energy levels of the cluster.

1.2.2 Geometric shell structure

So far, the Clemenger-Nilsson shell structure has been observed in many simple and noble metal cluster systems [5,6]. However, it only can describe the stability features of clusters, where the energy of the itinerant electrons dominates the size dependent properties. The detailed arrangement of the ionic cores is neglected. The alkali and noble metal clusters are quite well described by the

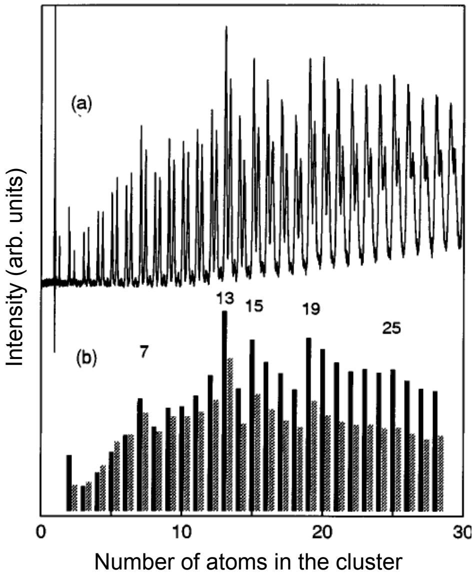

Figure 1.4: *(a) Mass spectrum of autoionized Ti clusters. (b) Intensities obtained from integrating the area under the peaks in the spectrum. Solid black and gray bars show the intensities of* Ti_N *and* Ti_NO *clusters, respectively* [21].

Clemenger-Nilsson shell model because the core orbitals (filled *d* shell or noble gas shell) and the valence orbitals (*sp*) are separated by a relative large energy gap.

For transition metals, the presence of a partially filled *d* orbital changes this picture completely. The rather localized valence *d* electrons hamper the observation of a simple electronic shell structure in transition metal clusters. In these situations, the cluster sizes with an enhanced stability often obey the hard-sphere packing model as observed in rare gas clusters [19,20]. Clusters with complete shells of atoms forming close-packed geometries will be especially stable. For transition metal clusters, a variety of experimental observations and theoretical calculations shows that a 13-atom icosahedral cluster has an enhanced stability in most cases [19-22].

Figure 1.4 shows a mass abundance spectrum of titanium clusters. One can see intensity anomalies, peaks with a higher intensity or sudden drops in abundance

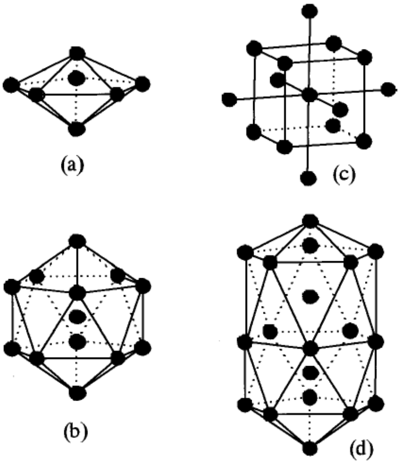

Figure 1.5: *Structural models for stable transition metal clusters: (a) pentagonal bipyramid (N=7), (b) icosahedron (N=13), (c) BCC (N=15), and (d) double icosahedron (N=19)* [21].

after certain sizes, for example, at $N = 7$, 13, 15, 19, 23, and 25. The major anomalies of titanium clusters relate to the icosahedral geometries, corresponding to cluster sizes with $N_i = 1 + \sum_{k=1}^{i}(10k^2 + 2)$ atoms. As illustrated in Fig. 1.5, the strongly enhanced abundance of the 13-atom clusters is attributed to the icosahedral structure, while the 15-atom clusters form a geometrically stable BCC structure. A pentagonal bipyramid, which is the elemental unit of the icosahedron, is determined for $N = 7$ clusters. The magic number of $N = 19$ is a partial combination of the pentagonal bipyramid and icosahedral stacking. The fine structure is attributed to subshell closures from completely covered facets of a cluster surface.

Not only transition metals and rare gases but also several other systems prefer a growth pattern of compact geometric shells. E.g., the stability of $(\mathrm{NaI})_N$ and In_N clusters is enhanced when respectively square and triangular faces of cuboid and octahedral structures are completed [19]. Systems like Ca_N, Mg_N, and $(\mathrm{C}_{60})_N$ also prefer an icosahedral growth pattern [19].

1.3 Magnetism in free clusters

The definition of the magnetic dipole moment of a particle is

$$\overrightarrow{\mu} = \frac{1}{2}\int \overrightarrow{r} \times \overrightarrow{J} dV \tag{1.7}$$

where $\overrightarrow{J}$ is the current density, $\overrightarrow{r}$ is the position within the particle, and V is the particle volume [23]. The resulting quantum-mechanical expression for the magnetic moment of an electron system is

$$\overrightarrow{\mu} = \frac{g_J \mu_B}{\hbar}(\overrightarrow{L} + \overrightarrow{S}) \tag{1.8}$$

where g_J is the Landé factor, $\mu_B = e\hbar/2m_e$ is the Bohr magneton constant, and $\overrightarrow{L}$ and $\overrightarrow{S}$ are quantum mechanical operators of the orbital and spin angular momentum [23]. The magnetic moments of the nuclei are small and can be ignored when considering the cluster magnetism.

Since clusters in a molecular beam are free from any interaction with a matrix, their intrinsic magnetic moments can be measured using an appropriate technique. With the fundamental experiments on space-quantization of atoms in magnetic fields, V. W. Stern and O. Gerlach demonstrated that atoms in different quantum states can be spatially separated by an inhomogeneous magnetic field [24]. From these measurements the Stern-Gerlach technique has become the standard in detecting and measuring the magnetic dipole moment of free clusters. In this section, we introduce the Stern-Gerlach method and recent achievements in studying the magnetism of clusters.

1.3.1 The magnetic deflection experiment

Figure 1.6 schematically shows a general arrangement of the Stern-Gerlach deflection setup. The main idea is that a collimated neutral particle beam is directed into a static magnetic induction $\overrightarrow{B}$. The force experienced by a particle with magnetic moment $\overrightarrow{\mu}$ is

$$\overrightarrow{F} = (\overrightarrow{\mu} \cdot \overrightarrow{\nabla})\overrightarrow{B} \tag{1.9}$$

A homogeneous field will not exert a net force on the magnetic dipole. The magnetic field used in Stern-Gerlach experiments should be inhomogeneous with a well-defined gradient. The inhomogeneous magnet provides the field and its gradient in the z direction, and their product is approximately constant over

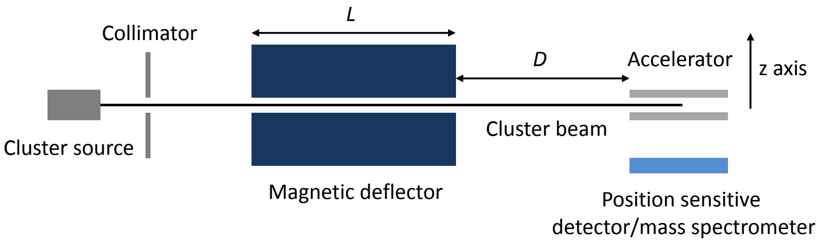

Figure 1.6: *Outline of the configuration of a Stern-Gerlach magnetic deflection experiment for free clusters.*

a relatively large region along the beam axis. It deflects any magnetic cluster by a distance [24]

$$d = \langle \mu_z \rangle \frac{\partial B}{\partial z} \frac{(L^2 + 2DL)}{2mv^2} \tag{1.10}$$

where L is the length of the magnet, and D is the distance from the magnet to the detection position. m and v are the mass and velocity of the cluster. $\langle \mu_z \rangle$ is the time-averaged projection of the cluster's magnetic moment along the direction of the field. The deflection can be measured using the position sensitive mode of a time-of-flight mass spectrometer. The neutral clusters have to be ionized before acceleration into the mass spectrometer. Since all other parameters in Eq. 1.10 are known, $\langle \mu_z \rangle$ can be determined from d.

1.3.2 Cluster ferromagnetism

Ferromagnetism is one of the most intensively studied properties of bulk matter. High magnetic moments of ferromagnetic materials result from a mutual alignment of electron spins. A better understanding of ferromagnetism, especially in small particles, is crucial not only for basic physical understanding but is also of great technological importance for both the existing industrial applications and the emerging nanotechnologies. In 1985, a pioneering experiment on free clusters of the ferromagnetic metal iron was performed by Cox *et al.* using the Stern-Gerlach deflection method [25]. Unfortunately, complete deflection beam profiles of these clusters were not measured, so that the most important difference between the deflection of a single iron atom and that of iron clusters was not observed.

The complete manifestation of iron cluster ferromagnetism was only revealed five years later by de Heer *et al.* [26]. A unique deflection of all iron clusters towards the direction of increasing field was strikingly shown. For an atom, one expects deflections to correspond to the different (quantized) projections of the magnetic moment along the direction of the magnetic field. In contrast, the observed single-sided deflection indicates that clusters behave like a spinning top and their magnetic moments appear to spontaneously align with the applied magnetic field. This deflection behavior of iron clusters was initially explained in terms of competition between the magnetic anisotropy energy and thermal energy using spin-relaxation theory [26]. At low temperature the magnetic anisotropy energy is much larger than the thermal energy, and the orientation of the magnetic moment is locked along the easy axis. When the thermal energy is high enough, the magnetic moment can fluctuate, resulting in the loss of hysteresis behavior. The spin-relaxation theory may be justified for large isolated clusters at relatively high energy. However, it is not clear how it applies to small isolated clusters with low thermal energy. Recently, the spin-relaxation behavior of cobalt clusters has been explained by an alternative theory based on the avoided crossing model [27], which does not require that individual clusters have defined temperatures. Discussions about the mechanism behind the spin relaxation behavior are still open.

In 1994, Billas and coworkers reported a comprehensive magnetic-deflection picture of iron, cobalt, and nickel clusters, showing how fascinating magnetism evolves in clusters from several tens to hundreds of atoms for temperatures between 80 and 1000 K [28]. Average magnetic moments per atom for Ni clusters at 78 K, Co clusters at 78 K, and Fe clusters at 120 K, as a function of the number of atoms in the clusters are shown in Fig. 1.7. Ferromagnetism was found even for the smallest sizes. For clusters with fewer than about 30 atoms the magnetic moments per atom are significantly larger than the expected moments extrapolated from the bulk. As the size is increased up to 700 atoms, the magnetic moments decrease approaching the bulk limit. However, the decrease of the magnetic moment per atom with size is not monotonic. It strongly oscillates as a function of cluster size. The oscillations are most likely caused by the geometric shell structure of the clusters. The trends are explained in terms of an enhancement of magnetic moments caused by the relatively large surface area in clusters, since it is known that the magnetic moments at ferromagnetic surfaces are enhanced [28]. So far, the magnetic moments of various metal cluster systems have been investigated, confirming the spin-relaxation behavior of ferromagnetic clusters [29-33]. Interestingly,

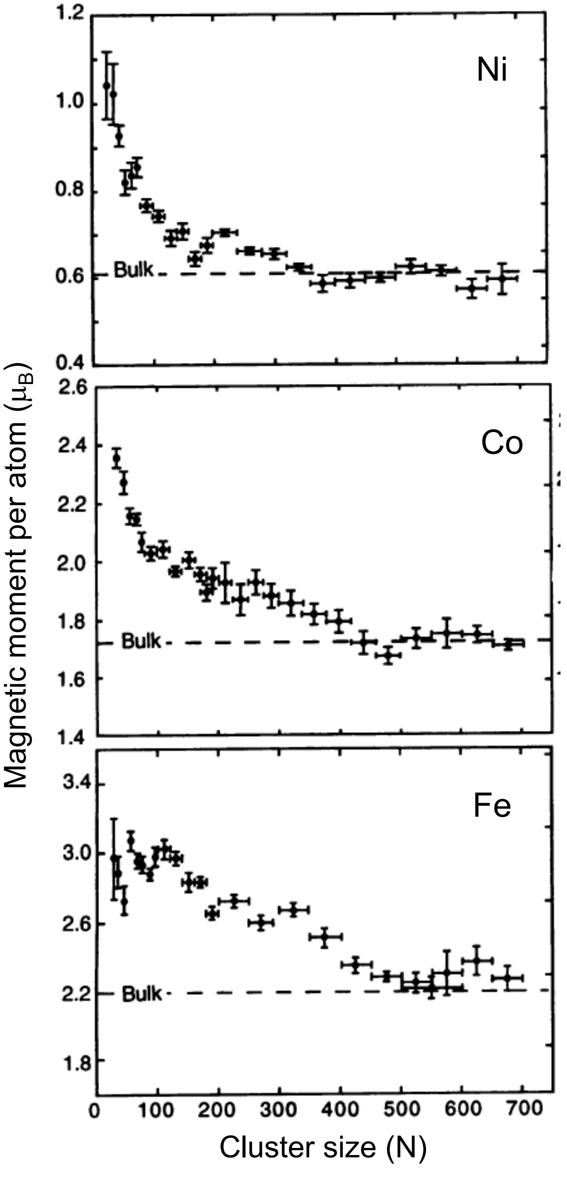

Figure 1.7: *Magnetic moments of nickel, cobalt, and iron clusters as a function of cluster sizes. For small clusters, the magnetic moment per atom is approximately 1, 2, and 3* μ_B*, respectively* [28].

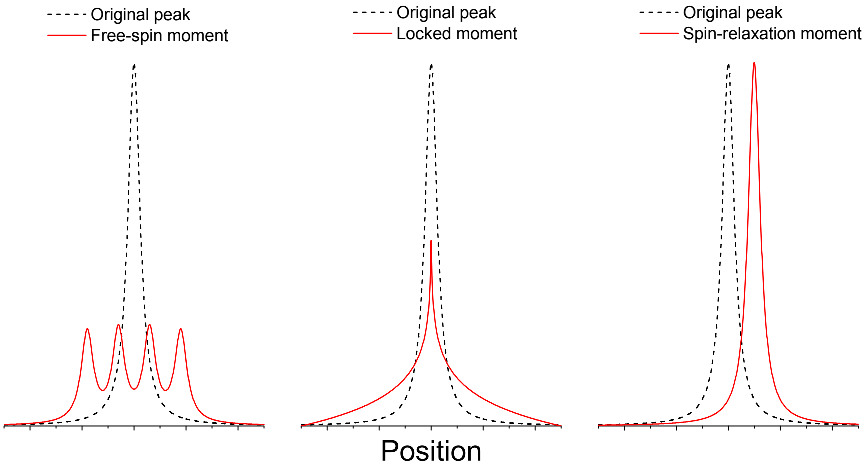

Figure 1.8: *Different magnetic deflection behavior in clusters. The black dashed and red solid lines indicate the position-sensitive spectra of clusters without and with the magnetic field, respectively.*

some metals are nonmagnetic in the bulk but their clusters are ferromagnetic, e.g. rhodium [31,32], or antiferromagnetic metals, e.g., manganese [29].

Although the influence of an external field on the magnetic moments of clusters can be directly measured, interpreting these data is not always straightforward and requires a careful consideration of the source conditions. If clusters were in thermal equilibrium at a certain temperature T, the answer could be well understood. However, this is usually not the case for clusters in a molecular beam due to the ambiguity of knowing the vibrational (T_{vib}) and rotational (T_{rot}) temperature of clusters. Experimental work has so far focused on three treatable cases as illustrated in Fig. 1.8:

- Free-spin moment: clusters behave as single atoms. The cluster beam splits in $2J + 1$ beamlets according to the angular momentum J.
- Locked (or rigid) moment: clusters and magnetic moment rigidly rotate as a whole and do not interact with vibrations. This results in a symmetric deflection pattern, strongly peaked at $d = 0$ and decaying asymptotically to zero at $\langle \mu_z \rangle = \pm\mu$. The relevant T will be T_{rot} of the clusters.

- Spin-relaxation (or floppy) moment: clusters deflect towards the direction of increasing field. This behavior is often explained using the superparamagnetic theory. At a certain temperature (blocking temperature) the thermal energy is higher than the magnetic anisotropy energy. The orientation of cluster magnetic moment can easily flip with respect to the particle axis. When the timescale of this flipping behavior is much faster than the measuring time, the cluster behaves like paramagnetic particles, resulting in single-sided deflection. The relevant T will be T_{vib} of the clusters.

1.4 Bimetallic clusters: challenges and benefits

Homogeneous clusters consisting of one type of metal atoms have been studied extensively during the eighties and nineties. It was shown that metal cluster properties dramatically change as a function of cluster size. Physics becomes even more fascinating when introducing a dopant atom in the host metal cluster, since this inherently offers the possibility of altering cluster stability, structure, and magnetism nearly at will.

Size- and constituent-dependent stability

Along with the improvement of cluster sources, the influence of a dopant on simple metal clusters was investigated. The standard electronic shell model becomes invalid due to the charge-background modification of impurities [34]. The observation of abundance maxima for 10-electron K_8Mg and K_8Zn systems by Kappes and coworkers can be regarded as the pioneering step in the onset of bimetallic cluster physics [35]. The interaction between localized bonds and free electrons in transition metal (from Sc to Ni) doped coinage metal (Ag and Au) clusters have been examined [36-39]. Photofragmentation studies demonstrated that the light dopants (Sc and Ti) contribute both their $4s$ and $3d$ electrons to the mutual cloud of itinerant electrons. For the heavier dopants (from Cr to Ni) only the $4s$ electrons are delocalized. While Au_9^+ is observed as a magic cluster containing eight delocalized electrons, the mass abundance spectra featured the enhanced stability of the 6-delocalized-electron planar ring Au_5X^+ (X = Cr, Mn, Fe, Co, Zn) systems. The stability patterns of transition metal doped Ag clusters reflected an electronic shell structure with dopant-dependent magic numbers. Enhanced stabilities were observed for $Ag_{11}Fe^+$, $Ag_{10}Co^+$, and Ag_9Ni^+ due to the contribution of 8, 9, and 10 valence electrons from Fe, Co, and Ni, respectively, forming a closed shell of 18 electrons. While by now the

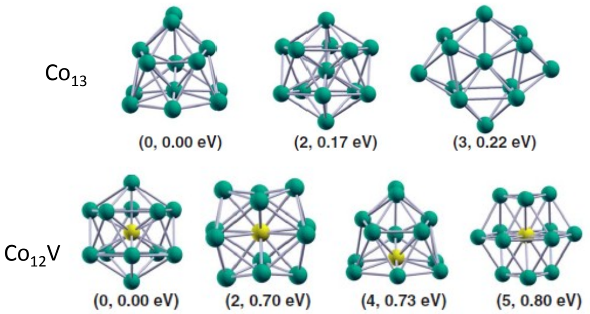

Figure 1.9: *(Top) Structures of optimal HCP, icosahedron, and cuboctahedron isomers of* Co_{13} *(from left to right). (Bottom) Structures of optimal icosahedron, optimal cuboctahedron, and two HCP geometries (from left to right) for* $Co_{12}V$*. Green dots represent Co atoms, while yellow dots represent V atoms. The first entry in the parenthesis gives the isomeric position and the second entry corresponds to relative energy with respect to the minimum-energy state* [60].

size- and constituent-dependent stability is intensively studied for (transition) metal doped simple metal clusters [40-44], very little is known about how the cluster stability develops in more complex systems, such as transition metal doped transition metal clusters. The presence of partially filled *d* shells of these metals results in many near isoenergetic isomers with different geometries and spin configurations. Already in dimers, these issues lead to a huge amount of possible electronic configurations with almost equal energies [7]. Despite the complexity, the binary transition metal clusters are still challenging for profound understanding and their potential use in applications deserves great attention.

Stable encapsulated structures

Another promising aspect of bimetallic clusters is that they allow to create exceptionally stable species via structural alternation by choosing an appropriate dopant atom. The smallest highest symmetric building block, the 13-atom icosahedron consisting of 12 atoms symmetrically surrounding a central dopant, attracted a lot of attention [45-48]. The close-packed structure of 13-atom icosahedra is well established and often observed as a magic number in mass spectrometry of pure transition metal clusters [7,21]. A structural transformation

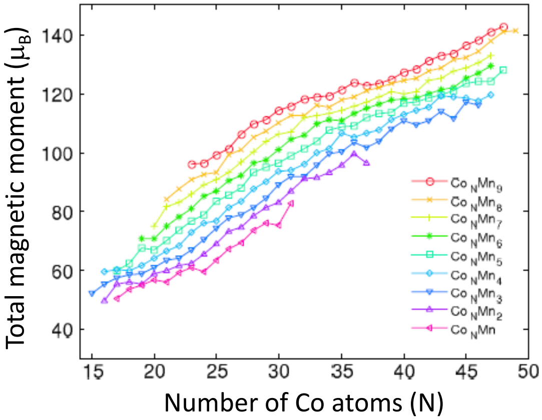

Figure 1.10: *Total magnetic moment of $Co_N Mn_M$ clusters as a function of N. Each series represents clusters with the same number of Mn atoms. The experimental uncertainty is about 1.5 μ_B* [12].

to the stable icosahedron can be stimulated by introducing a proper dopant atom in the center of the host clusters. This is due to the fact that the vertex-vertex bonds (a) in a perfect icosahedron is about 5 % longer than the center-vertex ones (R):

$$R = \frac{5^{1/4}}{2}\sqrt{\tau}a \tag{1.11}$$

where $\tau = (1+\sqrt{5})/2$ is the golden ratio or divine proportion [49]. An extensively discussed example is the family of $Al_{12}M$ with M from the third and fourth main group, containing a magic number of 40 valence electrons [50-52]. Striking magic behavior of $Pb_{12}Al$ in the mass abundance spectra of Al doped Si, Ge, Sn, and Pb clusters [9,53] has attracted intensive attention, but mainly in computational work [54-57]. Numerous theoretical studies suggest an enhanced stability of $Co_{12}TM$ (TM = Sc, Ti, V, Cr, Mn, Fe, and Ni) systems over the Co_{13} cluster via the icosahedral transformation [58-60]. Figure 1.9 illustrates the predicted structures of Co_{13} and $Co_{12}V$. The HCP geometry is found to be the ground state of Co_{13}, while the single V atom likes to occupy the central position in a 12-atom cage, and it is ferrimagnetically coupled with the surface Co atoms [61-64]. However, to our knowledge, still no direct observation of the stability of these clusters has been reported.

Tailoring magnetic moments

Bimetallic clusters also carry significant practical promises for tailoring magnetic moments as building blocks of nanostructured materials with novel magnetic properties. Some studies of alloy species in the search for novel nanomagnetic materials have been carried out. Stern-Gerlach experiments have been performed on BiCo [13], DyTe, and DyBi clusters [14]. Recently, a magnetic deflection study of BiMn clusters [15] has found either ferromagnetic or ferrimagnetic coupling behavior, depending on size and composition. More surprisingly, the per atom average moments of CoMn clusters are found to increase with the Mn concentration (see Fig. 1.10) in contrast to bulk CoMn [12]. Meanwhile, CoV clusters show a reduction of average moments with increasing V doping, consistent with what is expected in bulk CoV.

While the evolution of magnetic moments with cluster size and composition is well investigated for several transition metal clusters and also for some alloy systems, many interesting questions remain to be explored. For example, one of the standing questions in the physics of non-magnetic metals incorporating a low concentration of magnetic atoms is the size of the so-called Kondo cloud [65-68]. The interaction of magnetic impurities with the metallic host will allow observing the occurrence (or not) of the Kondo-like effect in a range of clusters from a few up to several tens of atoms, and, in particular, to detect the smallest size from where the Kondo effect shows up.

It also is interesting to study the transformation of the ferrimagnetic-ferromagnetic coupling in transition metal clusters, which can result in a giant magnetic moment. One way to accomplish this is by doping [69,70]. If doping also increases the stability of the cluster compared to the pure clusters, this will be an additional achievement on top of spin engineering.

Another interesting effect is the dramatic change of magnetic properties of small transition metal clusters, such as chromium and manganese clusters, under chemical control, e.g., by doping with oxygen or nitrogen [71-73]. Interaction with electronegative dopants elongates the cluster bonds and leads to ferromagnetic coupling, through so-called superexchange interaction, where the exchange coupling between the transition metal atoms oscillates with the number of oxygen atoms. Such clusters will be promising building blocks for making new cluster-assembled materials.

1.5 Objectives of this work

So far, it is clear that bimetallic cluster systems are ideal objects in which one can tune the electronic and geometric properties, and thus, the stability, structure, and magnetism of the clusters. Highly stable clusters with unique magnetic, optical, and thermal properties are very promising as building blocks of future cluster assembled materials. For that purpose, studying the fundamental properties of bimetallic clusters is an essential step toward the construction of cluster assembled materials.

The first goal of this thesis is to study the bonding, stability, and possible structure of binary cluster systems composed of (transition) metals, such as, $\mathrm{Pb}_n\mathrm{Al}^+$, $\mathrm{Co}_n\mathrm{TM}^+$ (TM = Ti, V, Co, Cr, Mn), and $\mathrm{Co}_{n-1}\mathrm{CrO}_m^+$. We will discuss several fundamental questions to go deeper into the physics of these quantum finite size systems. How are clusters excited and fragmented by the photon absorption? How does the dopant change the cluster fragmentation behavior in binary transition metal systems? How do the cluster size and constituents influence the bonding, stability, and likely structure? Can the dopant-encapsulated icosahedra be stimulated, and their stabilities be enhanced by proper doping?

Further studying magnetic properties of bimetallic cluster systems requires an adequate experimental tool. The second goal of this thesis is therefore dedicated to the design, implementation, and realization of a new magnetic deflection setup. The setup is compatible with the Leuven binary cluster source, which is an advantage over the existing setups for studying magnetic properties of binary species. To maintain the high mass resolution during position-sensitive measurements, the magnetic deflection system is coupled to a HRTOF mass spectrometer, where the time (mass) and position (magnetism) information is measured simultaneously by a position-sensitive detector. First results of magnetic deflection experiments are presented.

References

1. M. L. Cohen and W. D. Knight, Phys. Today **43**, 42 (1990).
2. E. J. Robbins, R. E. Leckenby, P. Willis, Adv. Phys. **16**, 739 (1967).

3. W. D. Knight, K. Clemenger, W. A. de Heer, W. A. Saunders, M. Y. Chou, and M. L. Cohen, Phys. Rev. Lett. **52**, 2141 (1984).
4. K. Clemenger, Phys. Rev. B **32**, 1359 (1985).
5. W. A. de Heer, Rev. Mod. Phys. **65**, 611 (1993).
6. M. Brack, Rev. Mod. Phys. **65**, 677 (1993).
7. M. D. Morse, Chem. Rev. **86**, 1049 (1986).
8. J. A. Alonso, Chem. Rev. **100**, 637 (2000).
9. S. Neukermans, *Physical properties of stable dopant encapsulated binary clusters*, PhD thesis (KU Leuven, Leuven, 2004).
10. E. Janssens, *Electronic and geometric structure of transition metal doped silver and gold clusters*, PhD thesis (KU Leuven, Leuven, 2004).
11. P. Claes, *Physical properties of transition metal doped gold and silicon clusters studied with mass spectrometry and action spectroscopy*, PhD thesis (KU Leuven, Leuven, 2011).
12. S. Yin, R. Moro, X. Xu, and W. A. de Heer, Phys. Rev. Lett. **98**, 113401 (2007).
13. T. Hihara, S. Pokrant, and J. A. Becker, Chem. Phys. Lett. **294**, 357 (1998).
14. S. Pokrant, C. Herwig, T. Hihara, and J. A. Becker, Eur. Phys. J. D **9**, 509 (1999).
15. S. Yin, X. Xu, R. Moro, and W. A. de Heer, Phys. Rev. B **72**, 174410 (2005).
16. M. G. Mayer and J. H. D. Jensen, *Elementary theory of nuclear shell structure* (Wiley, New York, 1955).
17. H. A. Jahn and E. Teller, Proc. R. Soc. London Ser. A **161**, 220 (1937).
18. S. G. Nilsson, K. Dan. Vidensk. Selsk. Mat. Fys. Medd. **29**, 16 (1955).
19. T. P. Martin, Phys. Rep. **273**, 199 (1996).
20. W. Miehle, O. Kandler, T. Leisner, and O. Echt, J. Chem. Phys. **91**, 5940 (1989).
21. M. Sakurai, K. Watanabe, K. Sumiyama, and K. Suzuki, J. Chem. Phys. **111**, 235 (1999).

22. T. P. Martin, T. Bergmann, H. Gohlich, and T. Lange, Chem. Phys. Lett. **176**, 343 (1991).

23. R. P. Feynman, R. B. Leighton, and M. Sands, *The Feynman Lectures on Physics* (Addison Wesley, 2006).

24. V. W. Gerlach and O. Stern, Zeit. Phys. **9**, 349 (1922).

25. D. M. Cox, D. J. Trevor, R. L. Whetten, E. A. Rohlfing, and A. Kaldor, Phys. Rev. B **32**, 7290 (1985).

26. W. A. de Heer, P. Milani, and A. Chatelain, Phys. Rev. Lett. **65**, 488 (1990).

27. X. Xu, S. Yin, R. Moro, and W. A. de Heer, Phys. Rev. B **78**, 054430 (2008).

28. I. M. L. Billas, A. Chatelain, and W. A. de Heer, Science **265**, 1682 (1994).

29. M. B. Knickelbein, Phys. Rev. Lett. **86**, 5255 (2001).

30. F. W. Payne, Wei Jiang, and L. A. Bloomfield, Phys. Rev. Lett. **97**, 193401 (2006).

31. A. J. Cox, J. G. Louderback, S. E. Apsel, and L. A. Bloomfield, Phys. Rev. B **49**, 12295 (1994).

32. A. J. Cox, J. G. Louderback, and L. A. Bloomfield, Phys. Rev. Lett. **71**, 923 (1993).

33. D. C. Douglass, J. P. Bucher, and L. A. Bloomfield, Phys. Rev. Lett. **68**, 1774 (1992).

34. C. Baladron and J. A. Alonso, Physica B **154**, 73 (1988).

35. M. M. Kappes, P. Radi, M. Schar, and E. Schumacher, Chem. Phys. Lett. **119**, 11 (1985).

36. S. Neukermans, E. Janssens, H. Tanaka, R. E. Silverans, and P. Lievens, Phys. Rev. Lett. **90**, 033401 (2003).

37. H. Tanaka, S. Neukermans, E. Janssens, R. E. Silverans, and P. Lievens, J. Am. Chem. Soc. **125**, 2862 (2003).

38. E. Janssens, S. Neukermans, H. M. T. Nguyen, M. T. Nguyen, P. Lievens, Phys. Rev. Lett. **94**, 113401 (2005).

39. E. Janssens, H. Tanaka, S. Neukermans, R. E. Silverans, P. Lievens, Phys. Rev. B **69**, 085402 (2004).

40. H. Kudo, Nature **355**, 432 (1992).

41. M. Heinebrodt, N. Malinowski, F. Tast, W. Branz, I. M. L. Billas, and T. P. Martin, J. Chem. Phys. **110**, 9915 (1999).

42. W. Bouwen, F. Vanhoutte, F. Despa, S. Bouckaert, S. Neukermans, L. T. Kuhn, H. Weidele, P. Lievens, and R. E. Silverans, Chem. Phys. Lett. **314**, 227 (1999).

43. U. Heiz, A. Vayloyan, E. Schumacher, C. Yeretzian, M. Stener, P. Gisdakis, N. Rosch, J. Chem. Phys. **105**, 5574 (1996).

44. P. Lievens, P. Thoen, S. Bouckaert, W. Bouwen, F. Vanhoutte,H. Weidele, and R. E. Silverans, Chem. Phys. Lett. **302**, 751 (1999).

45. S. N. Khanna and P. Jena, Phys. Rev. Lett, **69**, 1664 (1992).

46. V. Kumar and Y. Kawazoe, Appl. Phys. Lett. **80**, 859 (2002).

47. P. Pyykko and N. Runeberg, Ang. Chem. Int. Ed. **41**, 2174 (2002).

48. X. Li, B. Kiran, J. Li, H. J. Zhai, and L. S. Wang, Angew. Chem. **114**, 4980 (2002).

49. http://mathworld.wolfram.com/icosahedron.html.

50. X. G. Gong and V. Kumar, Phys. Rev. Lett. **70**, 2078 (1993).

51. X. Li and L. S. Wang, Phys. Rev. B **65**, 153404 (2003).

52. B. K. Rao and P. Jena, J. Chem. Phys. **115**, 778 (2001).

53. S. Neukermans, E. Janssens, Z. F. Chen, R. E. Silverans, P. v. Schleyer, and P. Lievens, Phys. Rev. Lett. **92**, 163401 (2004).

54. D. L. Chen, W. Q. Tian, and C. C. Sun, Phys. Rev. A **75**, 013201 (2007)

55. D. L. Chen, W. Q. Tian, W. C. Lu, and C. C. Sun, J. Chem. Phys. **124**, 154313 (2006).

56. C. Rajesh and C. Majumder, J. Chem. Phys. **128**, 024308 (2008).

57. G. Chen and Y. Kawazoe, J. Chem. Phys. **126**, 014703 (2007).

58. Y. Jinlong, X. Chuanyun, X. Shangda, and W. Kelin, Phys. Rev. B **48**, 12155 (1993).

59. J. Lv, F. Q. Zhang, J. F. Jia, X. H. Xu, and H. S. Wu, J. Mol. Struct.: THEOCHEM **955**, 14 (2010).

60. S. Datta, M. Kabir, T. Saha-Dasgupta, and A. Mookerjee, Phys. Rev. B **80**, 085418 (2009).

61. S. Nonose, Y. Sone, K. Onodera, S. Sudo, and K. Kaya, J. Phys. Chem. **94**, 2744 (1990).

62. A. Nakajima, T. Kishi, T. Sugioka, Y. Sone, and K. Kaya, J. Phys. Chem. **95**, 6833 (1991).

63. K. Hoshino, T. Naganuma, K. Watanabe, Y. Konishi, A. Nakajima, and K. Kaya, Chem. Phys. Lett. **239**, 369 (1995).

64. A. Pramann, K. Koyasu, and A. Nakajima, J. Phys. Chem. A **106**, 2483 (2002).

65. J. Kondo, Prog. Theor. Phys. **32**, 37 (1964).

66. H. C. Manoharan, C.P. Lutz, and D.M. Eigler, Nature **403**, 512 (2000).

67. V. Madhavan, W. Chen, T. Jamneala, M.F. Crommie, and N.S. Wingreen, Science **280**, 567 (1998).

68. L. Kouwenhoven and L. Glazman, Phys. World **14**, 33 (2001).

69. R. C. Longo, M. M. G. Alemany, A. Vega, J. Ferrer, and L. J. Gallego, Nanotechnology **19**, 245701 (2008).

70. S. Datta, M. Kabir, A. Mookerjee, and T. Saha-Dasgupta, Phys. Rev. B **83**, 075425 (2011).

71. B. V. Reddy, S.N. Khanna, Phys. Rev. Lett. **83**, 3170 (1999).

72. B. K. Rao and P. Jena, Phys. Rev. Lett. **89**, 185504 (2002).

73. K. Tono, A. Terasaki, T. Ohta, T. Kondow, Phys. Rev. Lett. **90**, 133402 (2003).

Chapter 2

Experimental methods

The experiments presented in this thesis are carried out on the Leuven HRTOF mass spectrometer, which has been used for photofragmentation experiments on bimetallic clusters. In section 2.1 we will introduce the general principles of the HRTOF, mainly focusing on the photofragmentation technique. A detailed technical description of the apparatus can be found in J. De Haeck's Ph.D. thesis [1]. The setup is currently extended to be able to perform magnetic deflection experiments, as described in Chapter 7. In section 2.2, the interpretation of photofragmentation processes is discussed.

2.1 Experimental setup

2.1.1 Overview of the apparatus

A schematic drawing of the Leuven HRTOF is shown in Fig. 2.1. The setup consists of three parts: the source chamber, the extraction chamber and the TOF chamber. The source chamber and the extraction chamber are connected by a 1 mm diameter conical orifice, the skimmer. The skimmer is used to select the central part of the cluster beam and to reduce the gas load in the extraction chamber. The setup is differentially vacated by four turbo molecular pumps to obtain ultra high vacuum conditions, providing a base pressure of $5{\cdot}10^{-8}$ mbar. Typical operating pressures are 10^{-4}, 10^{-6}, and 10^{-7} mbar in three subsequent chambers, respectively.

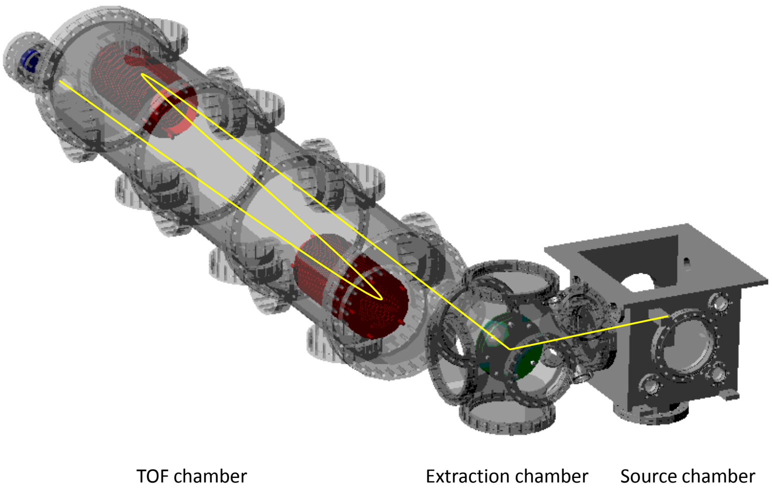

Figure 2.1: *Schematic overview of the Leuven high resolution free cluster setup before modification as described in chapter 7. The apparatus consists of three differentially pumped chambers, the source chamber, the extraction chamber, and the TOF chamber* [1]. *The yellow line indicates the cluster beam path.*

The whole setup is operated at a frequency of 10 Hz. Precise timing is important for optimal cluster production and photofragmentation. For this purpose, two delay generators (Stanford Research Systems, DG535) are employed. The master clock sends trigger pulses to the gas valve, ablation lasers, extraction optics, and oscilloscope. The second one, which is synchronized with the master clock, controls the mass selector and the fragmentation laser.

2.1.2 Binary cluster source

The clusters are produced using a dual-laser dual-target vaporization cluster source [2,3] installed in the source chamber. The source is a critical part of the apparatus, which is uniquely designed for producing binary clusters. Cluster formation in a laser vaporization source has been studied extensively and is well documented [4-6]. The source has several strengths. It allows the use of high-power pulsed lasers. Also a pulsed carrier gas inlet requires less gas load, low overall pressure in the chamber, and high instantaneous pressure inside the

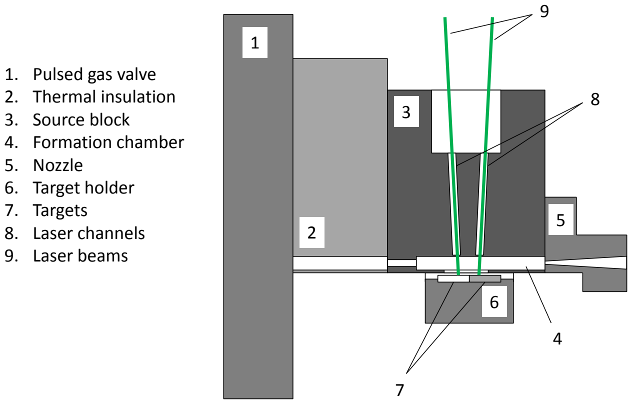

Figure 2.2: *Schematic drawing (not to scale) of the dual-target dual-laser vaporization source.*

source, providing a high cluster flux compared to continuous cluster sources.

A schematic drawing of the source is shown in Fig. 2.2. The source body is made of a stainless steel block, containing a formation chamber (17 mm long and 3 mm wide), which starts by the gas inlet and ends with the detachable conical nozzle (40 mm long). The two target materials are ablated by two independent 532 nm Nd:YAG lasers (Spectra Physics, INDI-HG and Continuum, Minilite II). The lasers are focused onto two target plates (7.5 x 25 mm^2) through two closely placed laser channels (1 mm diameter). A small glass is inserted into the front side of the laser channels to stabilize the pressure inside the formation chamber. The targets are moved in a closed-loop pattern using UHV compatible stepper motors (Arun Microelectronics Ltd., C17.2) under computer control. This allows the target plates to be uniformly ablated.

The process of laser vaporization is presented in Fig. 2.3. The laser energy absorbed by the solid surface can be expressed as [5]

$$I(x) = (1 - R)I_0e^{-\alpha x} \tag{2.1}$$

where I_0 is the laser fluence, $I(x)$ is the fluence at a distance x beneath the

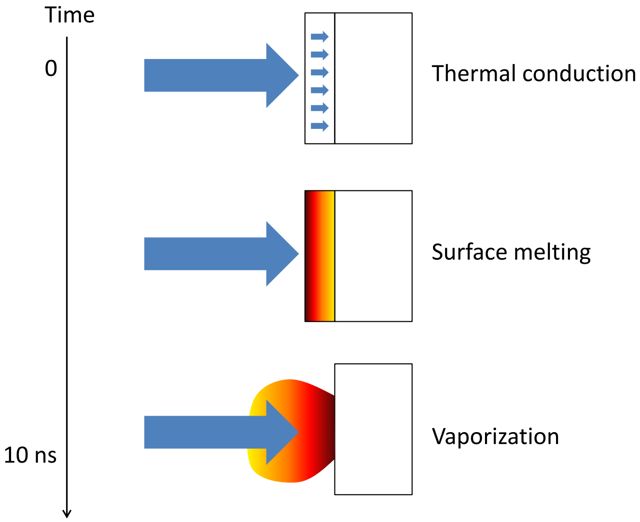

Figure 2.3: *Schematic representation of the laser vaporization process.*

surface, α is the absorption coefficient, and R is the reflectivity. The target material is also characterized by a specific heat C_v, a density ρ, and a thermal conductivity K. The thermal diffusivity $D = K/C_v\rho$ determines the thermal diffusion length after a time t of laser irradiation $L_{th} = (2Dt)^{1/2}$. For a laser power density Q_0, the heated layer has gained an average thermal energy $Q_0 t/(Dt)^{1/2}$. When this energy exceeds the sublimation energy of the solid in a time shorter than the duration τ of the laser pulse, evaporation takes place. The laser firing time, focusing spot size, and energy all affect the vaporization [3].

Synchronous with the laser ablation, highly purified helium gas is introduced into the source by a pulsed supersonic valve (R.M. Jordan, C-211), with a pressure up to 8 bar. The formation of clusters is initiated by collision of the helium carrier gas with the material vapor. Metal dimers are mainly formed by three-body collisions during which the energy and momentum conservation have to be fulfilled simultaneously [7]. The helium carrier gas will take away the formation energy of each created dimer. The bond is stabilized against re-evaporation if the remaining thermal energy of the metal dimer is lower than its binding energy. Once dimers are formed, they act as condensation centra for further growth. While clusters increase in size, the helium atoms keep them in thermal equilibrium with the source block walls. The cluster source is thermally

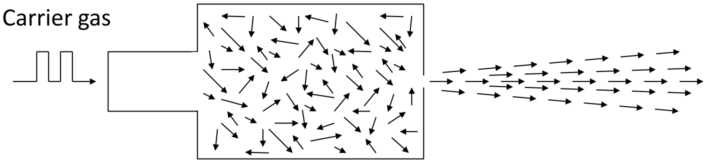

Figure 2.4: *Schematic representation of the expansion from a high-pressure formation chamber through a small nozzle, which results in a supersonic beam. The arrows represent the cluster velocities.*

and electrically isolated from the surroundings by Teflon parts.

The mixture of clusters and helium gas then expands out of the high-pressure formation room into the vacuum chamber through the nozzle, resulting in a supersonic beam with narrow distribution of relatively high velocities as shown in Fig. 2.4 [8-10]. The cluster beam velocity does strongly depend on the relative timing between firing the laser and introducing the helium gas [7]. The particle velocities inside the source are randomized, but after expanding through the nozzle the beam gets directed. Further clustering in the expansion is not likely due to the low particle density and the straight beam direction. For each target material, the shape, diameter, and opening angle of the nozzle can be adjusted in order to have the desired cluster size distribution. After leaving the nozzle, the central part of the cluster beam is selected by the skimmer before entering the extraction chamber.

2.1.3 Curved field extraction optics

The curved field extraction optics (the green part in Fig. 2.1), which has recently been developed by Jorg De Haeck for high mass resolution purposes [1], originally consists of three parallel metallic plates (Kore Technology). The back plate can be pulsed from zero up to 10 kV by utilizing an ultrafast high voltage push-pull switch (Behlke, HTS 151-GSM-03). The middle plate, placed 14 mm away from the two other plates, is used for double stage extraction. It has a rectangular hole of 32 x 110 mm^2 and is pulsed to the same voltage as the back plate. The front grounded plate has a grid of bonded nickel mesh. The extraction optics can operate without the middle plate for a compromise of

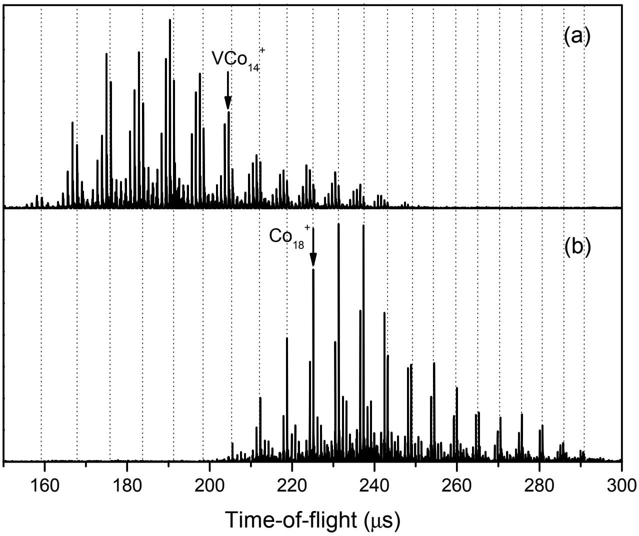

Figure 2.5: *Typical mass spectra of* $V_m Co_{n-m}^{+}$ *clusters produced in the HRTOF setup for different horizontal extraction angles: (a)* 0^o *and (b)* 0.5^o*. The dotted lines indicate the pure* Co_n^+ *clusters.*

resolution and signal intensity.

The extraction assembly can be moved as a whole and tilted by an elaborate motion system. The linear movement of the extraction optics in the x and y direction (of the plane perpendicular to the TOF chamber) is controlled by two translation feedthroughs to optimize the alignment between the exiting cluster beam with the axis of the TOF. A X-Y precision tilting device is installed to tilt the extraction plates in the range of $\pm$ 1.5^o using UHV stepper motors. This motion is driven by two separate motors for the vertical and horizontal tilt, respectively.

In the extraction chamber, cationic clusters are orthogonally accelerated into the TOF mass spectrometer. For neutral clusters, additional laser postionization is employed. In this case, the initially charged clusters are removed from the beam by electrostatic deflection. If the extraction direction is the same as that of the initial cluster velocity vector, the mass range of the TOF mass spectrometer could be unlimited. However, this is not applicable for the orthogonal extraction. Because of the original velocity component, the velocity acquired after acceleration will have a nonzero angle compared to the acceleration field. This angle depends on the kinetic energy and not solely on the initial velocity. If all ions in the original ion beam travel with equal energy, the angle after acceleration will be fixed. If all ions in the original ion beam travel with equal velocity, the angle after acceleration is larger for larger masses. Since the velocity of particles in a molecular beam is nearly independent of their mass, the mass range is restricted of about 500 amu. To achieve different mass ranges of clusters, the extraction optics has to be moved and tilted.

Figure 2.5 presents typical mass spectra of $V_mCo_{n-m}^+$ clusters produced with the orthogonal extraction at two different lateral angles: (a) 0^o and (b) 0.5^o. The pure cobalt clusters are marked by dotted lines. The peaks before Co_n^+ correspond to VCo_{n-1}^+, $V_2Co_{n-2}^+$, $V_3Co_{n-3}^+$ ... The corresponding cluster distributions are (a) from Co_{10}^+ to Co_{20}^+ and (b) from Co_{16}^+ to Co_{28}^+.

2.1.4 High-resolution TOF mass spectrometer

In the large cylindrical TOF chamber, the clusters are reflected twice by the dual stage reflectron system to enhance the mass resolution ($m/\Delta m$) up to 10000. The mass resolution achieved in this study is around 4000 due to the use of simple single stage extraction to increase the signal intensity.

The reflectrons (the red part in Fig. 2.1) are uniform electric mirrors mounted at two ends of the TOF chamber. Consider two clusters with the same mass but slightly different drift velocities heading towards the reflectron. The cluster with a lower velocity needs less time to reverse its direction in the reflectron. The faster cluster spends more time since it penetrates deeper. By carefully tuning the electric field of the reflectrons with regard to the cluster kinetic energies, the difference of traveling time is corrected. Consequently, the mass resolution of the instrument is improved. The clusters are then reflected by the second reflectron before hitting the detector.

At the end of the flight path, cluster signals are recorded by a 40 mm-diameter chevron type MCP detector (the blue part in Fig. 2.1, Kore Technology). The impact of charged particles with sufficient kinetic energy creates a small current, which is further amplified 20 times by a fast amplifier (Fast ComTec, TA2000B).

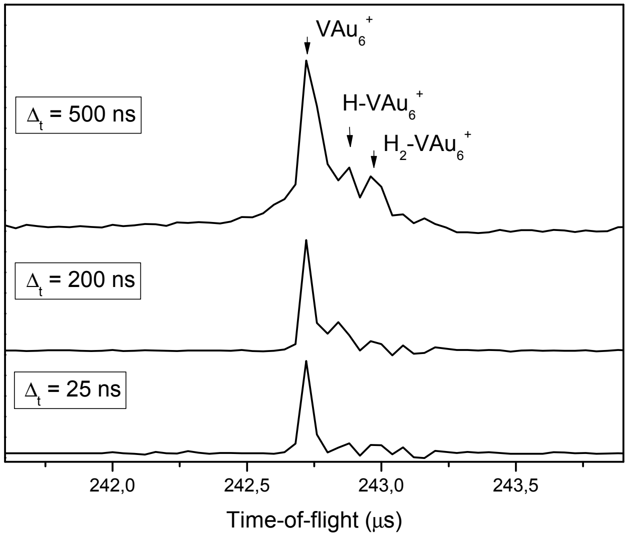

Figure 2.6: *Mass selective transmission of* VAu_6^+ *cluster according to opening times* Δ_t.

The amplified signals are finally collected by a digital oscilloscope (Tektronix, TDS3000B).

2.1.5 Mass selection

The setup is equipped with an ion deflection-type mass gate [11] installed at the first intermediate focal point for mass-selective fragmentation experiments. The mass gate consists of a periodic array of parallel wire segments formed by two electrically isolated sets of wires (± 250 V). The deflection area consists of a 15 mm diameter circular aperture placed perpendicular to the cluster beam direction. If no voltage is applied on the two wire sets, the ions travel freely through the gate. Applying opposite voltages of equal magnitude on the set of wires results in an electrical field that deflects the charged particles. By opening the gate only during a short time interval when the time-focused ion packet of interest passes through the selector, mass selective ion transmission is obtained. For this purpose, a pulsed voltage switch (Behlke, HS 21-03) with a minimum pulse width Δ_t of 15 ns is used. The mass selection resolution is determined by the strength of the electrostatic field of the parallel wire system, the duration of the pulse width Δ_t and the accurate positioning of the mass gate. In practice, if Δ_t is shorter than 30 ns, signal loss becomes significant, especially for large cluster sizes.

Figure 2.6 shows the evolution of mass selective transmission for the VAu_6^+ cluster. The VAu_6^+ peak is observed along with the hydrogen contaminated ones (H-VAu_6^+ and H_2-VAu_6^+). Voltages of ± 100 V are applied to the wire segments. By decreasing Δ_t, the hydrogen contaminated peaks are gradually eliminated. At $\Delta_t = 25$ ns, only the non-contaminated VAu_6^+ is selected but the intensity is considerably reduced.

2.2 Photofragmentation technique

In this section, we focus on the photofragmentation technique and how the cluster stability information can be obtained from fragmentation spectra. First, the photofragmentation technique will be introduced and the interpretation of mass-selected photofragmentation spectra is discussed. The relation between the photofragmentation behavior and the relative stability of clusters is explained. Finally, in the third part, statistical models in combination with photofragmentation spectra are discussed to extract the dissociation energies that are associated with the cluster stability.

2.2.1 Mass-selective photofragmentation

Figure 2.7 illustrates the working principles of the photofragmentation experiments in the present work. After formation, the cluster beam is perpendicularly accelerated into the TOF chamber by the extraction. The clusters follow a Z-shaped beam path in the TOF chamber. The first reflectron is used for temporally focusing the cluster beam in the mass gate. The mass-selected clusters are then photofragmented by a high power Nd:YAG laser (Quanta Ray, GCR-150) with a third harmonic generation option. The laser is slightly defocused to have a beam diameter of 15 mm at the interaction region. The laser fluence is varied in the range of 0-100 mJ/cm^2 for fluence dependence measurements. The second reflectron focuses the fragmented cluster beam onto

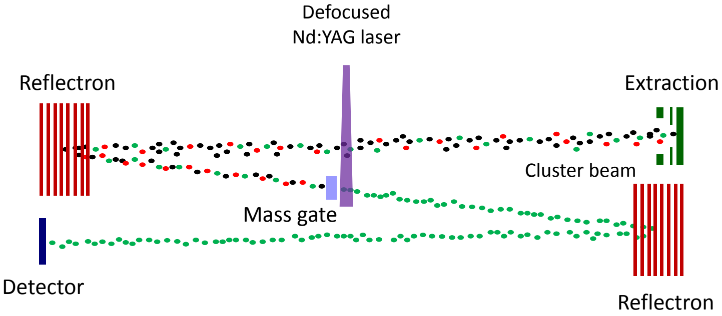

Figure 2.7: *Illustration of the mass-selected photofragmentation setup.*

the detector.

Figure 2.8 shows a typical example of the relative timing sequence for the mass-selected photofragmentation experiments. Following the trigger from the master clock, opening of the pulsed valve is the first event in the sequence. The two Nd:YAG lasers ablate the dopant and host targets at about 170 and 480 μs after the first trigger, respectively. The extraction pulse to accelerate cationic clusters into the TOF chamber is the next event with a minimal pulse length of 50 μs. The extraction time is typically varied between 670 and 1170 μs. The exact value depends on the cluster size range of interest. The oscilloscope is externally triggered at the same time as the extraction. Following extraction, the potential of the mass gate is pulsed to zero when the desired ion passes while a constant voltage deflects the others. The photofragmentation laser is triggered 1 μs after opening the mass gate to fragment the mass-selected clusters. Finally, the relative arrival times of the fragment and remaining parent ions are detected and observed on the oscilloscope.

A typical example of a mass-selectively photofragmented spectrum is shown in Fig. 2.9 for $V_2Co_{16}^+$. The fragment and the remaining parent ions are detected. After fragmentation, the fragment cluster flies at the same velocity as that of the parent cluster. However, their flight times in the second reflectron are not the same because of the mass difference. The flight time for the fragment ion (daughter, D) in the second reflectron becomes [1]:

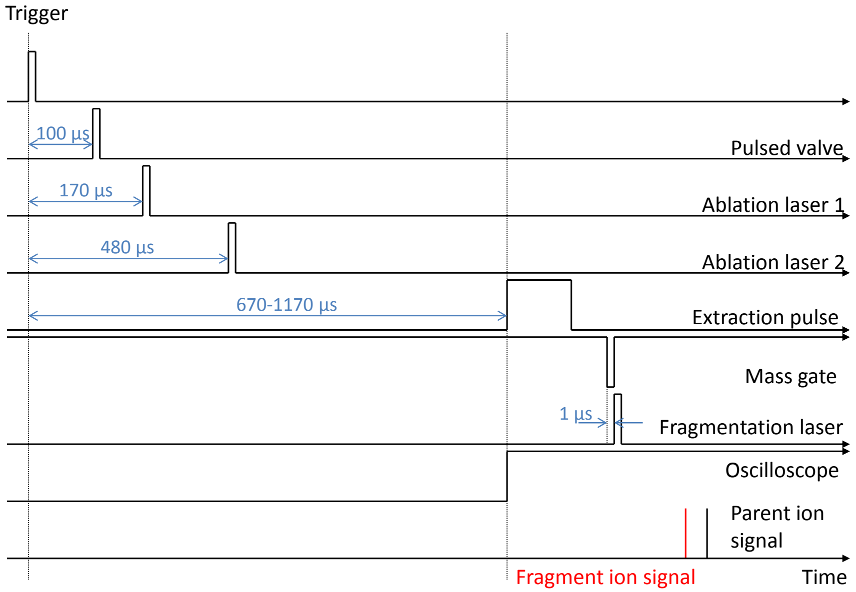

Figure 2.8: *Typical schematic diagram describing the relative timing of the mass spectrometer and laser systems utilized for photofragmentation experiments.*

$$t_{ref,D} = \sqrt{2m_D}\frac{l_{R1}}{q\Delta V_{R1}}\left(\sqrt{\frac{m_D}{m_P}E_k} - \sqrt{\frac{m_D}{m_P}E_k - q\Delta V_{R1}}\right) + \sqrt{2m_D}\frac{l_{R2}}{q\Delta V_{R2}}(\sqrt{\frac{m_D}{m_P}E_k - q\Delta V_{R1}}) \tag{2.2}$$

and for the remaining parent (P) ion

$$t_{ref,P} = \sqrt{2m_P}\frac{l_{R1}}{q\Delta V_{R1}}\left(\sqrt{E_k} - \sqrt{E_k - q\Delta V_{R1}}\right) + \sqrt{2m_P}\frac{l_{R2}}{q\Delta V_{R2}}\left(\sqrt{E_k - q\Delta V_{R1}}\right) \tag{2.3}$$

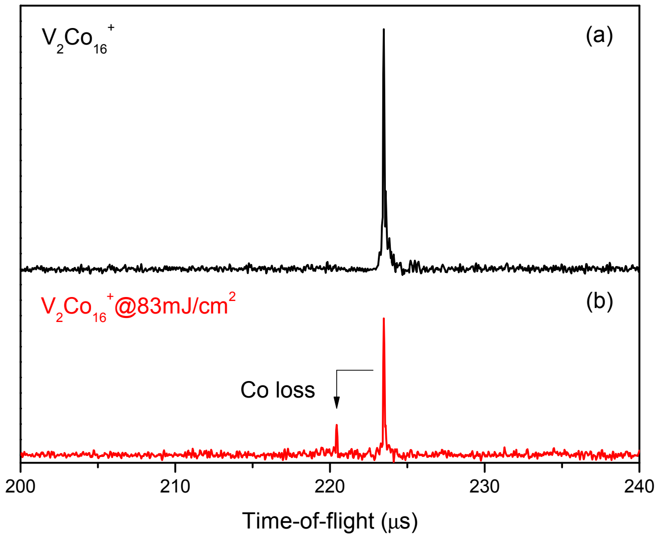

Figure 2.9: *An example of a mass-selectively photofragmented spectrum. The cluster is* $V_2Co_{16}^+$*, (a) mass-selected with* Δ_t *= 100 ns and (b) fragmented using 532 nm laser light at 83 mJ/cm*^{2}*. The lower intensity peak corresponds to the recorded ion fragment with a single Co atom loss.*

where m_P and m_D are the masses of the parent and fragment ions, respectively [1]. l and ΔV are the field stage length and the potential difference. The first and second field stage in the reflectron are denoted by the subscripts $R1$ and $R2$. E_k is the kinetic energy of the ions. Because the potentials and the dimensions of the reflectron as well as the kinetic energy of the clusters are known, the mass of the fragment can be determined. For example, in Fig. 2.9 $E_k = 6700$ eV, $l_{R1} = 0.1065$ m, $l_{R1} = 0.2051$ m, $\Delta V_{R1} = 4470$ eV, $\Delta V_{R2} = 3320$ eV. Based on the time difference between $\mathrm{V_2Co_{16}^+}$ and its fragment peak of 3.04 μs, the fragment ion is identified as $\mathrm{V_2Co_{15}^+}$.

The geometric overlap between the photofragmentation laser spot and cluster beam is important for calibrating the fragment/parent intensity ratio. The laser beam diameter is 15 mm at the interaction zone. The overlap factor can be determined once the cluster beam length is known. We first estimate the

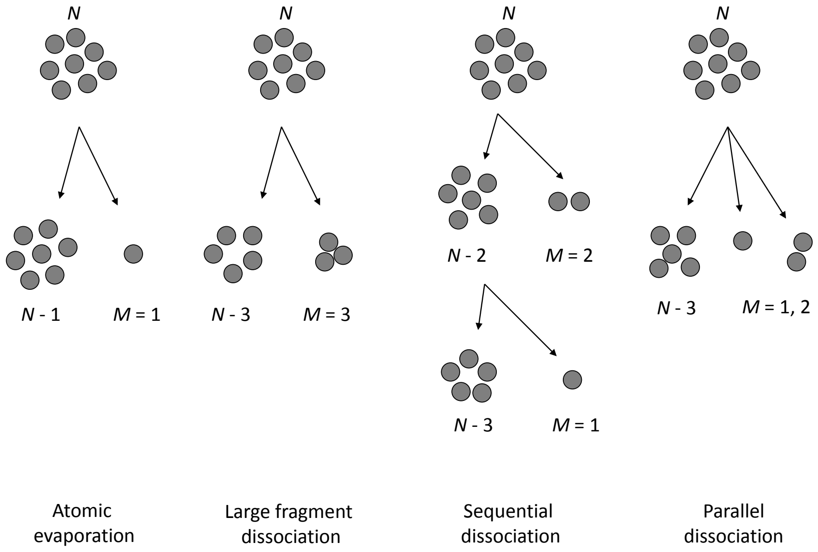

Figure 2.10: *Dissociation possibilities from an initially hot cluster X_N, resulting in the fragments $X_{N-\Sigma M_i}$ and X_{M_i}.*

velocity of the clusters of interest. For example, Co_n^+ (n = 10-30) clusters with E_k = 6700 eV have a velocity range of 27×10^3-47×10^3 m/s. Alternatively, the cluster velocity can also be estimated from the arrival time (160-280 μs) and the length of the field free zone (5.183 m), which turns out to be a velocity range of 19×10^3-32×10^3 m/s. If the opening time of the mass gate is less than 300 ns, the length of the mass-selected cluster pulses is always smaller than the laser beam spot. In our experiments, the overlap factor is between 0.8-1.0, typically depending on the signal intensity, cluster size, and target material.

2.2.2 Dissociation pathways and relative stability

Photofragmentation is an effective method to reveal the relative cluster stability [12,13]. By irradiating the clusters with laser light, they are excited. The excitation energy E^* gained by photon absorption is statistically distributed among all vibrational modes of the cluster system. The relation between E^* and the cluster temperature is defined by the equipartition theorem for harmonic oscillators

$$E^* = (3N - 6)k_BT \tag{2.4}$$

with N the number of atoms and ($3N$-6) the vibrational degrees of freedom. If the absorbed energy exceeds a certain threshold, implying a significant probability of localizing enough internal energy in a single mode to overcome the binding energy of a fragment, the cluster can spontaneously dissociate as a means to lower E^*

$$X_N \rightarrow \Sigma X_{M_i} + X_{N-\Sigma M_i} \tag{2.5}$$

Fragments can be single atoms, $M_i = 1$, and/or small clusters, $M_i > 1$. If the excitation energy is much larger than the dissociation threshold, e.g., by multiphoton absorption, multiple dissociation events can take place, where the fragments can be produced sequentially and/or in parallel. This is shown schematically in Fig. 2.10.

More stable clusters, characterized by larger bond dissociation energies, remain more intense after fragmentation. The dissociation process has the tendency to terminate at sizes and stoichiometries with enhanced stability because these are more robust than others having the same excess energy. In addition, they are also produced as preferred fragments from larger ones. It should be mentioned that if the photoexcitation energy is sufficiently high, a structural permutation can take place before fragmentation. The clusters will explore all possibilities of getting the energetically most favorable dissociation channel. The structural information of the precursors is thus erased during the permutation. This interpretation of photofragmentation spectra related to the relative stability of clusters has been widely applied in a number of papers, confirming that the dissociation behavior is governed by the relative stabilities of the clusters [14-20].

2.2.3 The theory of unimolecular decay

The stability of clusters can be determined once their dissociation energies D are known. Several approaches to describe the relation between binding energies and abundances of clusters have been discussed elsewhere [21-25]. However, none of them has provided a definite treatment. Although the dissociation energies of clusters are not measured directly in photofragmentation experiments, they can be extracted, under certain conditions, from the experimentally measured decay rate constant k_{decay}. Hereafter, we show that an explicit relation between D and k_{decay} can be derived using the theory of unimolecular decay [26], which leads to a conclusive determination of cluster stabilities.

Consider a stationary distribution of particles, where all particles can evaporate and recombine, forming two states that are in equilibrium, 'reactant' and 'product'. According to the stationary condition, the average number of particles does not change with time. The formation rate should be the same as the decay rate. Therefore their relation can be expressed as follows:

$$\frac{\rho_p(E)}{\rho_p(E)+\rho_r(E)} k_{formation} = \frac{\rho_r(E)}{\rho_p(E)+\rho_r(E)} k_{decay} \tag{2.6}$$

where the subscripts p and r refer to the product and reactant states, respectively. ρ is the energy level density, k is the rate constant, and E is the particle energy. For simplicity, we assume that only a single atom evaporates from a particle. Then the decay rate constant is

$$k_{decay}(E) = k_{formation} \frac{\rho_p(E)}{\rho_r(E)} = \frac{1}{V} \sigma \upsilon \frac{\rho_p(E)}{\rho_r(E)} \tag{2.7}$$

where $1/V$ is the concentration of the particle and υ is the relative speed of the product and reactant. The cross section σ for an atom captured by the product particle can be geometrically assumed as

$$\sigma = \pi r^2 [1 + (N-1)^{1/3}]^2 \tag{2.8}$$

where $r = \sqrt[3]{\frac{3}{4\pi\rho_b}}$ and ρ_b is the bulk density (particle/volume) .

The product now is comprised of the free atom and fragments. The level density of the free atom can be specified as

$$\rho = g \frac{V 4\pi \varepsilon^{1/2} \sqrt{2} m^{3/2}}{h^3} \tag{2.9}$$

and the level density of the product is

$$\frac{d}{d\varepsilon} \rho_p(E; \varepsilon) = g \frac{V 4\pi \varepsilon^{1/2} \sqrt{2} m^{3/2}}{h^3} \rho_d(E - D - \varepsilon) \tag{2.10}$$

where ε is kinetic energy of the free atom, m is the reduced mass of the atom and fragment, ρ_d is the level density of the fragment, and g is the atom degeneracy factor due to an intrinsic angular momentum. Combining Eqs. 2.7 and 2.10 gives us the decay rate constant

$$k_{decay}(E; \varepsilon) d\varepsilon = g \frac{m}{\pi^2 \hbar^3} \sigma(\varepsilon) \varepsilon \frac{\rho_d(E - D - \varepsilon)}{\rho_r(E)} d\varepsilon \tag{2.11}$$

By integrating k_{decay} over the kinetic energy ε with the use of the microcanonical temperature of the fragment, T_d, one finally gets:

$$k_{decay}(E) = g \frac{m}{\pi^2 \hbar^3} \langle \sigma \rangle T_d^2 \frac{\rho_d(E - D)}{\rho_r(E)} \tag{2.12}$$

with

$$\rho_d(E - D - \varepsilon) \simeq e^{-\varepsilon/T_d}\rho_d(E - D) \tag{2.13}$$

and

$$\langle\sigma\rangle \equiv \frac{\int_0^E \sigma(\varepsilon)\varepsilon exp(-\varepsilon/T_d)d\varepsilon}{\int_0^E \varepsilon exp(-\varepsilon/T_d)d\varepsilon}. \tag{2.14}$$

In Eq. 2.12, the factor in front of the level density ratio can be understood as a frequency factor, ω, and the decay rate constant can be written as [22,26-30]

$$k_{decay}(E) = \omega\frac{\rho_d(E - D)}{\rho_r(E)} \tag{2.15}$$

with $\omega = g\frac{m}{\pi^2\hbar^3}\langle\sigma\rangle T_d^2$. For an energy independent and geometrically assumed $\sigma = \pi r^2 N^{2/3}$, the frequency factor is [22,26]

$$\omega \approx g\frac{m}{\pi^2\hbar^3}\pi r^2 N^{2/3} T_d^2. \tag{2.16}$$

The level densities of the fragment and reactant particles can be approximated by using the high energy limit of harmonic oscillators [22,26]

$$\rho_N(E) = \frac{[E + (3N - 6)\hbar\omega_D/2]^{3N-7}}{(3N - 7)!\,(\hbar\omega_D)^{3N-6}} \tag{2.17}$$

where ω_D is the Debye frequency of N-atom particles. Following Eqs. 2.15 and 2.17, we get the dissociation energy

$$D = E + (3N - 9)\hbar\omega_D/2 - [E + (3N - 6)\hbar\omega_D/2]\left(\frac{k_{decay}(E)}{\omega(\hbar\omega_D/k_B T_d)^3}\right)^{1/(3N-7)}. \tag{2.18}$$

Formula 2.18 shows that the monomer dissociation energy can be calculated explicitly if the decay rate constant k_{decay} is known. There are only two approximations made: i) the high energy limit of the level densities and ii) the geometric approximation of the capture cross section. It should also be mentioned that Eq. 2.15 is used with the assumption of complete statistical mixing, where the fragmentation occurs after the time needed for the excitation energy to dissipate over all accessible degrees of freedom. The decay rate constant can be experimentally determined by fluence-dependent measurements under single photon absorption conditions. In chapter 3, we apply this approach to retrieve the dissociation energies of AlPb$_n^+$ clusters by photofragmentation experiments. For a detailed explanation of the unimolecular decay theory, the reader can consult Ref. [26].

References

1. J. De Haeck, *Mass spectrometric developments and a study of lithium doped silicon and germanium clusters*, PhD thesis (KU Leuven, Leuven, 2011).
2. P. Thoen, *Lithium oxide and lithium monocarbide clusters: production by a laser vaporization source and measurement of the ionization potentials*, PhD thesis (KU Leuven, Leuven, 1998).
3. W. Bouwen, P. Thoen, F. Vanhoutte, S. Bouckaert, F. Despa, H. Weidele, R. E. Silverans, and P. Lievens, Rev. Sci. Instrum. **71**, 54 (2000).
4. O. F. Hagena and W. Obert, J. Chem. Phys. **56**, 1793 (1971).
5. P. Milani and S. Iannotta, *Cluster beam synthesis of nano structured materials* (Springer, Berlin Heidelberg New York, 1999).
6. H. Pauly, *Atom, molecule and cluster beam II* (Springer, Berlin Heidelberg New York, 2000).
7. J. M. Soler, N. Garcia, O. Echt, K. Sattler, and E. Recknagel, Phys. Rev. Lett. **49**, 1857 (1982).
8. O. F. Hagena, Surf. Sci. **106**, 101 (1981).
9. O. F. Hagena, Rev. Sci. Instrum. **63**, 2374 (1992).
10. G. Scoles (ed.), *Atomic and molecular beam methods* (Oxford University Press, Oxford, 1988).
11. P. R. Vlasak, D. J. Beussman, M. R. Davenport, and C. G. Enke, Rev. Sci. Instrum. **67**, 68 (1996).
12. W. A. de Heer, Rev. Mod. Phys. **65**, 611 (1993).
13. E. Janssens, *Electronic and geometric structure of transition metal doped silver and gold clusters*, PhD thesis (KU Leuven, Leuven, 2004).
14. J. B. Jaeger, T. D. Jaeger, and M. A. Duncan, J. Phys. Chem. A **110**, 9310 (2006).
15. C. J. Dibble, S. T. Akin, S. Ard, C. P. Fowler, and M. A. Duncan, J. Phys. Chem. A **116**, 5398 (2012).
16. K. S. Molek, Z. D. Reed, A. M. Ricks, and M. A. Duncan, J. Phys. Chem. A **111**, 8080 (2007).
17. K. S. Molek, T. D. Jaeger, and M. A. Duncan, J. Chem. Phys. **123**, 144313 (2005).

18. K. S. Molek, C. Anfuso-Cleary, and M. A. Duncan, J. Phys. Chem. A **112**, 9238 (2008).

19. E. Janssens, S. Neukermans, H.M.T. Nguyen, M.T. Nguyen, P. Lievens, Phys. Rev. Lett. **94**, 113401 (2005).

20. S. Neukermans, E. Janssens, H. Tanaka, R. E. Silverans, and P. Lievens, Phys. Rev. Lett. **90**, 033401 (2003).

21. W. A. de Heer, W. D. Knight, M. Y. Chou, and M. L. Cohen, Solid State Phys. **40**, 93 (1987).

22. K. Hansen and U. Naher, Phys. Rev. A **60**, 1240 (1999).

23. K. Hansen and M. Manninen, J. Chem. Phys. **101**, 10481 (1994).

24. S. Bjørnholm, J. Borggreen, O. Echt, K. Hansen, J. Pedersen, and H. D. Rasmusen, Z. Phys. D. **19**, 47 (1991).

25. S. Bjørnholm and J. Borggreen, Philos. Mag. B **79**, 1321 (1999).

26. K. Hansen, *Statistical physics of nanoparticles in the gas phase* (Springer, Dordrecht Heidelberg New York London, 2013).

27. G. F. Bertsch, N. Oberhofer, and S. Stringari, Z. Phys. D **20**, 123 (1991).

28. S. Frauendorf, Z. Phys. D **35**, 191 (1995).

29. P. Fröbrich, Phys. Lett. A **202**, 99 (1995).

30. D. H. E. Gross and P. A. Hervieux, Z. Phys. D **35**, 27 (1995).

Chapter 3

Exceptional stability of $Pb_{10}Al^{+}$ and $Pb_{12}Al^{+}$ clusters

The results presented in this chapter are based on:

Mass-selected photodissociation studies of Pb_nAl^{+} clusters ($n = 7 - 16$): evidence for the extraordinary stability of $Pb_{10}Al^{+}$ and $Pb_{12}Al^{+}$
S. Bhattacharyya, N. T. Tung, J. De Haeck, K. Hansen, P. Lievens, and E. Janssens
Physical Review B **87**, 054103 (2013).

Abstract

We report fragmentation pathways and dissociation energies of Pb_nAl^{+} ($n = 7 - 16$) clusters. The clusters are produced with pulsed laser vaporization and studied in a supersonic molecular beam setup. They are mass-selected and photodissociated with 532 and 355 nm laser light. Photofragments are thereafter mass-separated in a tandem reflectron time-of-flight mass spectrometer. Bare Pb_n^{+} ($n = 8 - 16$) clusters preferentially evaporate Pb atoms, with the exception of Pb_{15}^{+} that fragments by loss of a Pb_2 dimer to form the stable Pb_{13}^{+} cluster. The smallest Pb_nAl^{+} ($n = 7 - 11$) clusters also show mainly atomic Pb evaporation, whereas the favored fragmentation pathway of the larger clusters ($n = 12 - 16$) involves Pb_2 and Pb_3 fragments. $Pb_{10}Al^{+}$ and $Pb_{12}Al^{+}$ are the most intense fragments of several larger cluster sizes, demonstrating the high stability of these two sizes. Dissociation energies corresponding to the most facile fragmentation

channel of Pb_nAl^+ ($n = 11 - 15$) are bracketed from the measured laser fluence dependencies of the fragment intensities using constraints imposed by unimolecular reaction rates.

3.1 Introduction

A long-term goal of cluster science research is to synthesize chemically inert, particularly stable cluster species with specific properties that can be used as advanced materials in nanotechnology applications [1]. Bimetallic clusters could be the building blocks of these advanced materials, since their physical and chemical properties can be engineered by manipulating size, shape, and composition [2]. However, apart from a few fullerenes [3] and endohedral fullerenes, only the Zintl ions have been isolated in macroscopic amounts and have been crystallized in well-ordered lattices [4]. Among the variety of atomic clusters studied, group 14 clusters, especially pure and doped silicon clusters, have been investigated extensively, in part due to their importance in electronic devices. Computational studies have predicted a large number of highly symmetric icosahedral structures for heavier group 14 congeners [5]. The stability of several of these systems has been demonstrated by their high abundance in mass spectrometric studies on MS_n (M=Cr, Mn, Cu, Zn, and S = Si, Ge, Sn, Pb) [6]. A few years ago, the mass spectrometric discovery of the extremely stable $Pb_{10}Al^+$ and $Pb_{12}Al^+$ clusters was reported [7]. Their high stability was attributed to their closed-packed structure and optimally filled electron shells. Following this, Chen *et al.* [8,9] calculated, using density functional theory, the electronic structures and stabilities of $Pb_{12}M^+$ clusters, where M represents group 13 elements such as B, Al, Ga, In, and Tl. They suggested that the high stabilities arise from the closed-shell nature of the subsystems, which are subject to the $2(N_\pi + 1)^2$ rule with $N_\pi = 1$. These suggestions are in line with the general principles for designing stable symmetrical clusters taking into account both electron shell closure rules and geometric arguments to form close packed endohedral structures [10]. Rajesh *et al.* later investigated Pb_nM (M = C, Al, In, Mg, Sr, Ba, and Pb; n = 8, 10, 12, and 14) theoretically [11,12], and Bai *et al.* found that $Pb_{12}Fe$ has a stable icosahedral structure [13]. Schäfer *et al.* probed the position of a Mg atom in lead clusters by electric deflection studies and reported the formation of endohedral Mg doped lead cage structures [14]. Also the composition dependence of the electrical dipole moments of Sn_mPb_n ($7 \leq n + m \leq 15$) nanoalloys has been discussed [15]. Recently the onset of cluster assembling was studied via the formation of cluster dimers, $[Pb_{10}M]_2$ (M = Fe, Co, Ni), built up of $Pb_{10}M$ endohedral square antiprisms [16]. Theoretical as well as photoelectron spectroscopic investigations have shown that the anionic clusters Pb_{10}^{2-}, Pb_{12}^{2-} and also Sn_{12}^{2-} are highly aromatic and have caged structures [8,17-20]. Also the role of cage aromaticity for larger doped group 14 clusters has been studied [21,22]. It is also worth noting that the ligand-free bimetallic clusters, $M@Pb_{12}^{2-}$ and $M@Pb_{10}^{2-}$ with M = Ni, Pd, Pt, could be synthesized in solution [4].

In this chapter, we present a mass-selective photodissociation study of pure Pb_n^+ ($n = 8 - 16$) and aluminum doped Pb_nAl^+ ($n = 7 - 16$) clusters using 532 nm and 355 nm laser light. Conclusive evidence for the extraordinary high stability of $Pb_{10}Al^+$ and $Pb_{12}Al^+$ is given. Fragmentation pathways combined with mass spectrometric results allow commenting on structural characteristics of these species. In addition, laser fluence dependent photofragmentation studies on Pb_nAl^+ ($n = 11 - 15$) enabled us to set limits on the dissociation energies corresponding to their most facile fragmentation channels.

3.2 Experimental setup

Details of the experiments are discussed in chapter 2. In brief, bimetallic Pb_nAl^+ cluster cations are produced in a pulsed dual-target dual-laser vaporization source and studied in the HRTOF. In the cluster source rectangular aluminum and lead targets are ablated by two independent pulsed Nd-YAG lasers at 532 nm having a typical energy density ~8 mJ/cm^2. We assume that the temperature of the clusters equals the temperature of the cluster source (i.e., 300 K). Heat exchange with the walls of the source occurs via the He carrier gas. The validity of this assumption was confirmed in earlier work where argon absorption was studied as a function of the source temperature [23,24].

Doped lead clusters are skimmed into the extraction chamber. The cationic Pb_n^+ or Pb_nAl^+ clusters of interest are accelerated perpendicularly into the RTOF through extraction optics, and then mass selected by the wire type mass gate. These mass selected clusters are then exposed to the second (532 nm) or third (355 nm) harmonics of a Q-switched Nd-YAG laser close to the mass gate, and the resulting photofragments are mass separated by the second reflectron before hitting the MCP detector.

Table 3.1: *Dissociation channels for Pb_nAl^+ (n = 7-16). The primary fragment is the parent cluster in the sequential dissociation process.*

Parent cluster	Primary dissociation channel	Sequential†/Parallel‡ dissociation
Pb_7Al^+	$Pb_6Al^+ + Pb$	
Pb_8Al^+	$Pb_7Al^+ + Pb$	
Pb_9Al^+	$Pb_8Al^+ + Pb$	
$Pb_{10}Al^+$	$Pb_9Al^+ + Pb$	$Pb_8Al^+ + Pb$†
$Pb_{11}Al^+$	$Pb_{10}Al^+ + Pb$	$Pb_9Al^+ + Pb$†
$Pb_{12}Al^+$	$Pb_{10}Al^+ + Pb_2$	$Pb_{11}Al^+ + Pb$‡
$Pb_{13}Al^+$	$Pb_{12}Al^+ + Pb$	$Pb_{10}Al^+ + Pb_2$†
$Pb_{14}Al^+$	$Pb_{12}Al^+ + Pb_2$	
$Pb_{15}Al^+$	$Pb_{12}Al^+ + Pb_3$	
$Pb_{16}Al^+$	$Pb_{14}Al^+ + Pb_2$	$Pb_{12}Al^+ + Pb_2$†

3.3 Results and discussions

3.3.1 Photofragmentation channels

The photodissociation of Pb_nAl^+ ($n = 7 - 16$) was studied with 355 nm light as a function of laser fluence in the $5 - 80$ mJ/cm^2 range with a slightly defocused laser beam of diameter 13 mm. However, for $n = 7 - 10$ and $n = 16$, photofragments were only observed for fluences above 60 mJ/cm^2. For these sizes the low intensity of the photofragments did not allow us to perform a fluence dependence study. The dissociation channels of Pb_nAl^+ ($n = 7 - 16$) with 355 nm light are given in Table 3.1. For the smallest Pb_nAl^+ ($n = 7 - 9$) clusters only one dissociation channel is observed, which consists of monomer Pb atom evaporation. The larger Pb_nAl^+ clusters ($n = 10, 11, 13, 16$) also decay through one dissociation channel only, as evidenced by the lower laser fluence spectra. However, at higher fluence (around 30 mJ/cm^2) a second fragment appears with the fragment seen at lower fluence remaining more intense. This second fragment results from the absorption of two (or more) photons, which is concluded from the increase of the ratio of the intensities of second to primary fragments with laser fluence as well as its appearance at higher fluence only. $Pb_{12}Al^+$ appears to be an exception, here we find two parallel dissociation channels, i.e., monomer and dimer decay, with the dimer evaporation channel being the most intense. Both fragments originate directly from the parent cluster, because the ratio of the fragment peak intensities does not (for low laser fluence) depend on the laser fluence. The sequential and parallel fragmentation paths observed for Pb_nAl^+ ($n \geq 10$) are included in Table 3.1.

Pb_nAl^+ (n = 10, 11 and 13) clusters are found to dissociate via monomer evaporation, whereas Pb_nAl^+ (n = 12, 14 and 16) fragments via dimer Pb_2 loss to form $Pb_{n-2}Al^+$ fragment ions and $Pb_{15}Al^+$ dissociates by Pb_3 emission to form the stable $Pb_{12}Al^+$ fragment ion. Figure 3.1 shows mass spectra recorded after photodissociation of mass selected Pb_nAl^+ ($n = 7 - 15$) clusters with 355 nm laser light at a fluence of 70 mJ/cm^2. For all sizes, 532 nm laser light yielded the same primary dissociation channels as the 355 nm laser light, but no sequential dissociation channels are observed (not shown on figure). Only $Pb_{12}Al^+$ could not be fragmented with the 532 nm laser light, most likely because of energy reasons. An alternative explanation could be that the photoabsorption cross section is effectively zero.

The fragmentation channels recorded for Pb_nAl^+ ($n = 12 - 16$) show larger fragments, contrasting with the observations for bare Pb_n^+ clusters that all, except Pb_{15}^+, fragment by monomer evaporation. Mass spectra recorded after photodissociation of size selected pure Pb_n^+ ($n = 8 - 16$) with 100 mJ/cm^2 of 355 nm laser light are given in Fig. 3.2. The pure lead cluster cations all decay by monomer evaporation, except Pb_{15}^+ which decays by dimer evaporation to form the stable Pb_{13}^+ fragment cluster. The most facile fragmentation channels of cationic lead clusters have been computed by Rajesh and Majumder from total energies of the lowest energy isomers found in a DFT study at the GGA level including spin-orbit coupling effects [25]. Their predictions are in excellent agreement with the current results: monomer decay is the preferred channel for all Pb_n^+ clusters ($n = 2 - 14$) with the exception of Pb_{15}^+. Pb_{15}^+ decays by Pb_2 loss, confirming the higher stability of Pb_{13}^+, which is predicted to have a slightly distorted icosahedral symmetry. In addition the predicted fragmentation energies are all below 2.7 eV, which implies that a single 355 nm photon can induce photodissociation provided that the kinetic shift is not excessively large [25].

The observation of Pb_2 fragments from Pb_nAl^+ (n = 12 and 14) to form more stable $Pb_{n-2}Al^+$ and the Pb_3 fragment from $Pb_{15}Al^+$ leading to $Pb_{12}Al^+$ is of particular interest as most metallic clusters show atom evaporation only. Dimer evaporation has previously been observed in alkali metal and coinage metal clusters: lithium, sodium, copper, silver, gold, and doped gold clusters [26-31]. In these cases, the enhanced dimer evaporation channel is correlated strongly with an enhanced stability of the fragment cluster, reflecting either a closed electronic shell structure or a strong odd-even amplitude.

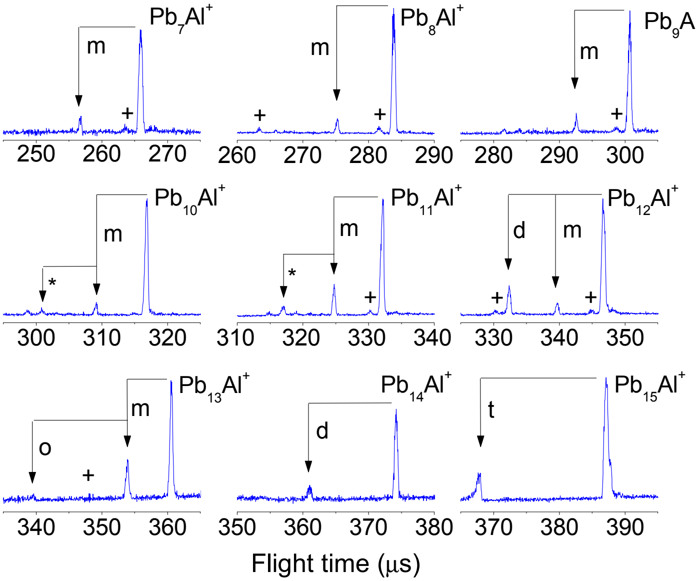

Figure 3.1: *Fragmentation of Pb_nAl^+ (n = 7-15) with 70 mJ/cm^2 laser light (355 nm). The dissociation channels (from parent to fragment) are indicated by arrows. Arrows labeled with m, d and t correspond to neutral Pb, Pb_2, and Pb_3 loss respectively. The arrows for $Pb_{12}Al^+$ indicate parallel monomer and dimer evaporation channels. '*' and 'o' correspond to sequential neutral Pb and Pb_2 evaporation from the first generation fragments. Additional peaks marked with '+' correspond to Pb_n^+ and $Pb_{n-1}Al^+$ clusters that are transmitted due to the limited resolution of the mass selector.*

As seen from Table 3.1, $Pb_{10}Al^+$ and $Pb_{12}Al^+$ appear as product in the photon induced decay chain of most studied Pb_nAl^+ ($n > 10$) clusters. $Pb_{10}Al^+$ is formed as primary fragment from $Pb_{11}Al^+$ and $Pb_{12}Al^+$ and as a secondary fragment from the photodissociation of the $Pb_{13}Al^+$ parent. Likewise, $Pb_{12}Al^+$ is formed as a primary photodissociation fragment from Pb_nAl^+ ($n = 13 - 15$) and in the sequential decay process from $Pb_{16}Al^+$.

The photon induced unimolecular dissociation tends to terminate at fragment ions with enhanced stabilities [32], and if certain clusters are formed as main fragment for several initial cluster sizes, they can be identified as relatively stable units. Our earlier mass spectrometric observations already indicated an extraordinary stability of $Pb_{10}Al^+$ and $Pb_{12}Al^+$ [7]. However, a high abundance of a specific size in a mass spectrum does not always reflect a higher stability, because cluster formation in a laser ablation source is sensitive to production parameters, and it is not obvious that the conditions for application of the evaporative ensemble theory are fulfilled [32]. Furthermore, the presence of the dimer channel seriously complicates the analysis. In the present investigation, wherein clusters are first mass selected, stability information is extracted from the intensity ratio of fragment to parent signals after laser irradiation and not from the intensity of the clusters as produced in the source. The results prove that the $Pb_{10}Al^+$ and $Pb_{12}Al^+$ clusters are significantly more stable than their precursors in the decay chain.

3.3.2 Dissociation energies

In order to extract dissociation energies, $D_{n,\Delta n}$, of a n-atom cluster dissociating into $n-\Delta n$ and Δn atom fragments from the experimentally relevant evaporative rate constant $k_n(E)$, an expression connecting these two via the excitation energy (E) is needed. Following Eq. 2.18, the dissociation energy for monomer evaporation, $D_{n,1}$, is:

$$\begin{aligned} D_{n,1} &= E + (3n-9)\hbar\omega_D/2 \\ &\quad - [E + (3n-6)\hbar\omega_D/2]\left(\frac{k_{n,1}(E)}{\omega'_{n,1}}\right)^{1/3n-7} \end{aligned} \tag{3.1}$$

with $\omega'_{n,1} = \omega_{n,1}(\hbar\omega_D/k_BT_d)^3$, which is of the order $10^{15} - 10^{16}$ s^{-1} (e.g., $\omega'_{n,1} = 8.1\times10^{15}$ s^{-1} for $Pb_{11}Al^+$). The excitation energy of the cluster is $E = E_{th} + h\nu$, where $E_{th} = (k_BT - \hbar\omega_D/2)(3n-6)$ is the thermal energy and $h\nu$ is the excitation energy resulting from the absorption of a photon.

The mass spectrometric observations are used to derive the evaporative rate constant $k_n(E)$. The width of the energy distribution prior to laser excitation is given by $2\sqrt{C/k_B}\ k_BT = 2\sqrt{3n-6}\ k_BT$. The largest value, for $Pb_{16}Al^+$, corresponds to 0.23 eV or only 0.054 times the total energy after absorption of a 355 nm photon. This worst case corresponds to a range of rate constants of about a factor of exp(1), which is the limit of validity of approximating the thermal distribution of rate constants with a single value. For smaller clusters, the approximation is better and we proceed with using a single value to describe the decay.

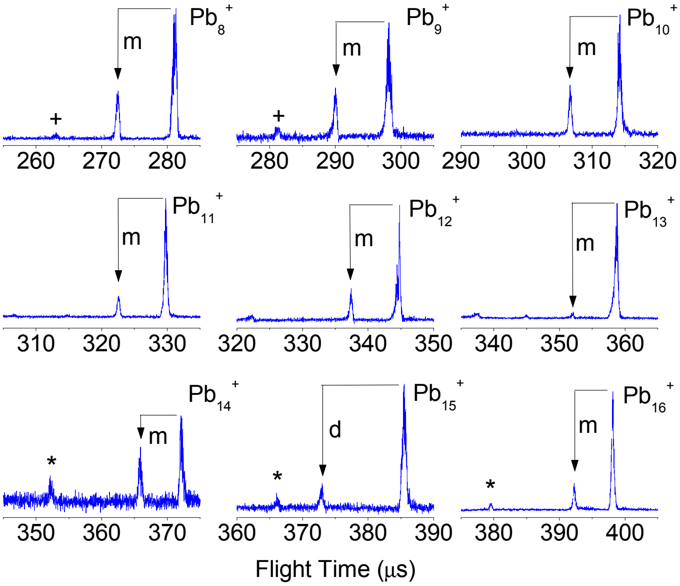

Figure 3.2: *Fragmentation of* Pb_n^+ *(n = 8-16) with 100* mJ/cm^2 *laser light (355 nm). The dissociation channels (from parent to fragment) are indicated by arrows labeled with m and d for neutral Pb and* Pb_2 *loss, respectively. Peak labeled with '*' correspond to* Pb_{n-3}^+ *fragments. These could be direct fragments from the corresponding* Pb_n^+ *parents or sequential fragments from* Pb_{n-1}^+*. Additional peaks marked with '+' correspond to* Pb_{n-1}^+ *clusters that are transmitted due to the limited resolution of the mass selector.*

When the laser fluence is in the single photon absorption regime, immediately after the laser fires ($t = 0$), there are basically two types of clusters: those that did absorb one single photon and those that did not absorb any photon: $I(0)$=$I^*(0)$+$I^0(0)$ with I^* and I^0 the intensity of the clusters that absorbed one and zero photons, respectively. The two fractions are given by

$$I^*(0) = \left(\frac{\sigma F_L}{h\nu}\right) I(0) \ and \ I^0(0) = \left(1 - \frac{\sigma F_L}{h\nu}\right) I(0), \tag{3.2}$$

where σ is the photon absorption cross section, F_L is the laser fluence and $h\nu$ the photon energy. In addition, one has to account for the fraction of clusters that is exposed to the laser beam. This imperfect overlap factor between the

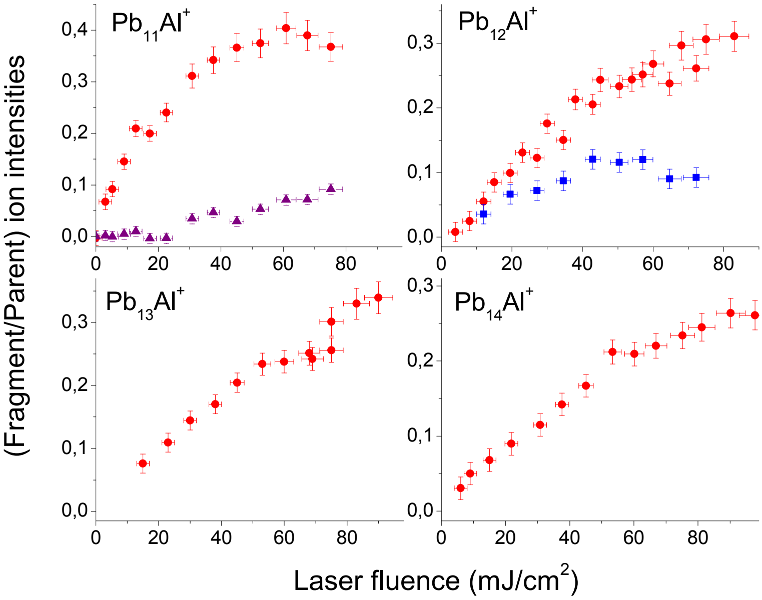

Figure 3.3: *Laser fluence dependence for i) $Pb_{11}Al^+ \rightarrow Pb_{10}Al^+ \rightarrow Pb_9Al^+$ and ii) $Pb_{12}Al^+ \rightarrow Pb_{10}Al^+$ and $Pb_{12}Al^+ \rightarrow Pb_{11}Al^+$ dissociation channels observed using 355 nm laser light, and iii) $Pb_{13}Al^+ \rightarrow Pb_{12}Al^+$ and iv) $Pb_{14}Al^+ \rightarrow Pb_{12}Al^+$ dissociation channels as seen with 532 nm laser light. Circles and triangles represent primary and secondary fragment ion intensities, respectively. The squares for $Pb_{12}Al^+$ correspond to the parallel monomer dissociation channel. The error bars represent uncertainties related to laser power fluctuations and the determination of the ion intensities (baseline dependence, fluctuations of the cluster source condition, etc.).*

ion packet and laser beam is estimated to be 75% based on geometry arguments (dimensions of the mass gate and the laser beam, quality of temporal focus point for the mass selective fragmentation). The intensities of the cluster signal are corrected for this overlap. The dissociation energies derived at the end of the analysis are not very sensitive to the overlap factor. A change by 10% results in a change of $D_{n,\Delta n}$ by a few percent only. Clusters that absorbed a photon (with an energy larger than the dissociation energy) will be subject to unimolecular dissociation at a rate $k_n(E)$, while the intensity of the non-excited clusters is constant. The ratio between the numbers of non-decayed and initial clusters is then:

$$\frac{I(t)}{I(0)} = 1 - \frac{\sigma F_L}{h\nu}(1 - e^{-k_n(E)t}) \tag{3.3}$$

with $I(t)$ the number of parent clusters at the time t given that the dissociation laser fires at $t = 0$ and the clusters reach the second reflectron at time t.

From the geometry of the instrument and the kinetic energies of the clusters, t can be estimated (e.g., ∼39 μs for $Pb_{12}Al^+$). The parent intensity at $t = 0$, $I(0)$, can be approximated by the sum of the parent and the fragment ion intensities at t. If σ were known, $k_n(E)$ can be obtained from the intensities of the peaks in the mass spectra vs. F_L using Eq. 3.3. Unfortunately σ cannot be determined directly. However, the fluence dependence data provide a range for σ. From Eq. 3.2 it is clear that in the single photon regime, $1 - \sigma F_L/h\nu$ and $\sigma F_L/h\nu$ are equal to the probabilities that none and one photon are absorbed by the cluster, respectively. The maximal laser fluence in the single photon regime must be such that $\sigma F_L/h\nu$ is smaller than unity, providing an upper boundary for σ. The depletion of the parent peak at the maximal fluence (in the linear regime) provides a lower boundary for σ: $1 - I(t)/I(0) < \sigma F_L/h\nu$ since at least one photon is to be absorbed to trigger dissociation. Following this reasoning we obtain, depending on the cluster size, typical cross-section ranges of 0.01 Å^2 – 0.08 Å^2 for the absorption of a 2.33 eV photon and of 0.03 Å^2 – 0.15 Å^2 for the absorption of a 3.55 eV photon.

Fig. 3.3 shows the variation of the intensity ratio of primary and secondary fragments to the parent signal as a function of the dissociation laser fluence. The fluence curves measured for Pb_nAl^+ ($n = 11-15$) at either 355 nm and 532 nm laser wavelengths all show a linear dependence below a certain threshold fluence, which indicates a single photon process, with the possible exception of $n = 11$.

Given the boundaries for σ, an upper and lower value for $k_n(E)$ and thus for $D_{n,\Delta n}$ can be derived. However, if $k_n(E)t \gg 1$ most excited clusters are dissociated on the time scale of the experiment. Since high rate constants correspond to low $D_{n,\Delta n}$ values, for most sizes only an upper boundary for $D_{n,\Delta}$ could be derived. The dissociation energies for clusters that decay by monomer evaporation, $Pb_{11}Al^+$ and $Pb_{13}Al^+$, are determined to be in the ranges $D_{11,1} \leq 2.04$ eV and $D_{13,1} = 1.80-1.92$ eV, respectively.

Eq. 3.1 cannot be used if the fragmentation occurs by dimer or trimer evaporation. The frequency factor for dimer ($\Delta n = 2$) and trimer ($\Delta n = 3$)

evaporation differs from that of a monomer because the rotational and vibrational degrees of freedom of the light fragment must be included in the level density. Applying a similar procedure as in Eq. 2.18 provides for the dimer decay:

$$\begin{aligned} D_{n,2} &= E + (3n-12)\hbar\omega_D/2 \\ &\quad - [E + (3n-6)\hbar\omega_D/2] \left(\frac{k_{n,2}(E)}{\omega_{n,2}}\right)^{1/3n-7} \end{aligned} \tag{3.4}$$

with [26]

$$\begin{aligned} \omega_{n,2} &= \omega'_{n,1} 0.809 \left(\frac{k_B T_d}{B_{dimer}}\right)\left(\frac{k_B T_d}{\hbar\omega_v}\right)\left(\frac{\hbar\omega_D}{0.05\text{ eV}}\right)^3 \\ &= 223\ \omega'_{n,1} \end{aligned} \tag{3.5}$$

The factor 0.809 is the symmetry number for the Pb_2 dimer considering the natural abundances of its four isotopes. In addition, there is a factor 2 from the reduced mass of the channel and a factor of 1/2 from the absence of electronic degeneracy of the atom. The rotational constant B_{dimer} is 0.0188534 cm^{-1} and $\hbar\omega_v = 109.6\ \text{cm}^{-1}$ [33]. The dissociation energy ranges determined using Eq. 3.4 for dimer evaporation from $Pb_{12}Al^+$ and $Pb_{14}Al^+$ gives $D_{12,2} = 2.33{-}2.98$ eV and $D_{14,2} \leq 2.07$ eV, respectively.

The frequency factor for trimer evaporation can be written as:

$$\begin{aligned} \omega_{n,3} &= \omega'_{n,1}\ 1.91 \left(\frac{k_B T_d}{B_{dimer}}\right)^{3/2}\left(\frac{k_B T_d}{\hbar\omega_v}\right)^3\left(\frac{\hbar\omega_D}{0.05\text{ eV}}\right)^6 \\ &= 3.0\times 10^3\ \omega'_{n,1} \end{aligned} \tag{3.6}$$

where it is assumed that the bond lengths in the trimer are equal to the dimer bond length (which explains the appearance of the dimer rotational constant in the equation) and with $\hbar\omega_v = 117\ \text{cm}^{-1}$ [34]. Following a similar procedure for the trimer emission from $Pb_{15}Al^+$, it is found that $D_{15,3} \leq 2.09$ eV.

The derived ranges for the dissociation energies are summarized in Table 3.2. These data show that i) the dissociation energies of Pb_nAl^+ ($n = 11-15$) vary strongly with cluster size. $Pb_{12}Al^+$ is by far the most stable cluster of the investigated size range. ii) A single 355 nm photon (3.49 eV) leads to photodissociation of all investigated clusters, while a single 532 nm photon (2.33 eV) cannot induce photofragmentation of $Pb_{12}Al^+$, in line with the

Table 3.2: *Dissociation energies ($D_{n,\Delta}$) of the Pb_nAl^+ (n = 11-15) clusters associated with the dissociation channels $Pb_nAl^+ \rightarrow Pb_{n-\Delta n}Al^+ + Pb_{\Delta n}$*

n,Δn	$D_{n,\Delta n}$(eV)
11,1	$D_{11,1} \leq 2.04$
12,2	$2.33 \leq D_{12,2} \leq 2.98$
13,1	$1.80 \leq D_{13,1} \leq 1.92$
14,2	$D_{14,2} \leq 2.07$
15,3	$D_{15,3} \leq 2.09$

observations discussed in section 3.3.1. iii) The experimental dissociation energies for $Pb_{11}Al^+$ ($D_{11,1} \leq 2.04$ eV) and $Pb_{12}Al^+$ (2.33 eV $\leq D_{12,2} \leq$ 2.98 eV) can be compared with calculated values of 2.98 eV and 3.75 eV, respectively (see supporting information of Ref. [10]). Although the calculated values are significantly higher than the experimental ones, the change from $Pb_{11}Al^+$ to $Pb_{12}Al^+$ and the preferred fragmentation channel are consistent. Moreover, it was shown for pure lead clusters that calculated binding energies can be significantly overestimated (of up to 1 eV) if spin-orbit coupling is ignored in the total energy calculations [25]. The experimental dissociation energies are within an energy range that is comparable to the dissociation energy range predicted computationally, including the spin-orbit coupling effect, for bare Pb_n^+ ($n = 10-15$) clusters (i.e., 1.8–2.7 eV with the exception of Pb_{14}^+ for which the monomer dissociation energy is predicted to be as low as 1.1 eV) [25].

3.4 Conclusions

The fragmentation pathways of mass selected Pb_nAl^+ ($n = 7-16$) clusters are investigated in photodissociation experiments using 532 nm and 355 nm laser light. $Pb_{10}Al^+$ and $Pb_{12}Al^+$ appear as the fragment of all larger clusters, which conclusively proves the high stability of these two clusters. Analysis of the laser fluence dependence of the fragment intensities established that the primary fragments are produced from one photon absorption processes. The dissociation energies of the most facile fragmentation channel of Pb_nAl^+ ($n = 11-15$) are bracketed based on the laser fluence dependence of the photon induced unimolecular decay. The dissociation energy of $Pb_{12}Al^+$ is shown to be significantly higher than that of the neighboring cluster sizes.

References

1. J. A. Alonso, *Structure and properties of atomic nanoclusters* (Imperial College Press, London, 2005).
2. R. Ferrando, J. Jellinek, and R. L. Johnston, Chem. Rev. **108**, 845 (2008).
3. H. W. Kroto, J. R. Heath, S. C. Obrien, R. F. Curl, and R. E. Smalley, Nature (London) **318**, 162 (1985).
4. E. N. Esenturk, J. Fettinger, and B. Eichhorn, J. Am. Chem. Soc. **128**, 9178 (2006).
5. V. Kumar and Y. Kawazoe, Appl. Phys. Lett. **80**, 859 (2002).
6. S. Neukermans, X. Wang, N. Veldemans, R.E. Silverans, and P. Lievens, Int. J. Mass. Spectrom. **252**, 145 (2006).
7. S. Neukermans, E. Janssens, Z. F. Chen, R. E. Silverans, P. v. R. Schleyer, and P. Lievens, Phys. Rev. Lett. **92**, 163401 (2004).
8. D. L. Chen, W. Q. Tian, W. C. Lu, and C. C. Sun, J. Chem. Phys. **124**, 154313 (2006).
9. D. L. Chen, W. Q. Tian, and C. C. Sun, Phys. Rev. A **75**, 013201 (2007).
10. Z. Chen, S. Neukermans, X. Wang, E. Janssens, Z. Zhou, R. E. Silverans, R. B. King, P. v. R. Schleyer, and P. Lievens, J. Am. Chem. Soc. **128**, 12829 (2006).
11. C. Rajesh and C. Majumder, Chem. Phys. Lett. **430**, 101 (2006).
12. C. Rajesh and C. Majumder, J. Chem. Phys. **128**, 024308 (2008).
13. Y. J. Bai, H. Y. Cheng, H. Q. Sun, N. Xu, and K. M. Deng, Physica B **406**, 3781 (2011).
14. S. Schafer and R. Schafer, ChemPhysChem **9**, 1925 (2008).
15. S. Heiles, S. Schafer, and R. Schafer, Phys. Chem. Chem. Phys. **12**, 247 (2010).
16. X. Chen, K. Deng, C. Xiao, J. Chen, and D. E. Ellis, Comput. Theor. Chem. **971**, 73 (2011).
17. P. v. R. Schleyer and H. Jiao, Pure Appl. Chem. **68**, 209 (1996).

18. D. Chen, W. Q. Tian, J. Feng, and C. Sun, J. Phys. Chem. A **111**, 8277 (2007).

19. L. Cui and L. Wang, J. Phys. Chem. A **110**, 10169 (2006).

20. L. Cui and L. Wang, Int. Rev. Phys. Chem. **27**, 139 (2008).

21. Y. Negishi, H. Kawamata, A. Nakajima, and K. Kaya, J. Electron Spectrosc. **106**, 117 (2000).

22. S. Furuse, K. Koyasu, J. Atobe, and A. Nakajima, J. Chem. Phys. **129**, 064311 (2008).

23. E. Janssens, P. Gruene, G. Meijer, L. Wöste, P. Lievens, and A. Fielicke, Phys. Rev. Lett. **99**, 063401 (2007).

24. S. M. Lang, P. Claes, N. T. Cuong, M. T. Nguyen, P. Lievens, and E. Janssens, J. Chem. Phys. **135**, 224305 (2011).

25. C. Rajesh and C. Majumder, J. Chem. Phys. **126**, 244704 (2007).

26. N. Veldeman, E. Janssens, K. Hansen, J. De Haeck, R. E. Silverans, and P. Lievens, Faraday Discuss. **138**, 147 (2008).

27. C. Brechignac, H. Busch, Ph. Cahuzac, and J. Leygnier, J. Chem. Phys. **101**, 6992 (1994).

28. S. Kruckeberg, L. Schweikhard, J. Ziegler, G. Dietrich, K. Lutzenkirchen, and C. Walther, J. Chem. Phys. **114**, 2955 (2001).

29. K. Hansen, Philos. Mag. B **79**, 1413 (1999).

30. S. Kruckeberg, G. Dietrich, K. Lutzenkirchen, L. Schweikhard, C. Walther, and J. Ziegler, Int. J. Mass. Spectrom. **155**, 141 (1996).

31. C. Brechignac, Ph. Cahuzac, J. Leygnier, and J Weiner, J. Chem. Phys. **90**, 1492 (1989).

32. K. Hansen and U. Näher, Phys. Rev. A **60**, 1240 (1999).

33. H. Sontag and R. Weber, J. Mol. Spectrosc. **100**, 75 (1983).

34. D. D. Stranz and R. K. Khanna, J. Chem. Phys. **74**, 2116 (1981).

Chapter 4

Size and dopant dependent stability of Co_nTM^+ (TM = Ti, V, Cr, and Mn) clusters

The results presented in this chapter are based on:

Dopant dependent stability of transition metal doped cobalt cluster cations
N. T. Tung, E. Janssens, and P. Lievens
Applied Physics B **114**, 497 (2014).

Abstract

In the preceding chapter, we have examined the stability of $AlPb_n^+$ clusters and learned how to extract the dissociation energies from fluence measurements. In this chapter, we present a photofragmentation study of mass-selected transition metal doped cobalt cluster cations Co_nTM^+ ($n = 8 - 18$, TM = Ti, V, Cr, and Mn). Time-of-flight spectra recorded after laser excitation of mass selected clusters in the gas phase show that the evaporation of a cobalt atom is the most facile dissociation channel for clusters with TM = Ti and V, suggesting an enhanced stability of the doped clusters compared to the bare ones. In contrast, for Co_nTM^+ with TM = Cr and Mn the loss of the dopant atom is found to be the preferred dissociation channel. $Co_{13}Cr^+$ is a notable exception and favors dissociation by loss of a neutral Co atom. It is implied that substituting Mn and Cr generally destabilizes the cobalt clusters with the exception of $Co_{12}Cr^+$,

which is relatively more stable than Co_{13}^{+}. Additional measurements of V_nCo^+ ($n = 9 - 16$) show that the loss of a Co atom is still the most facile dissociation channel, which is in agreement with the predicted stronger V−V bond compared to the V−Co one.

4.1 Introduction

Bimetallic clusters have become a subject of significant interest because of their potential use in new cluster-assembled materials with promising physical and chemical properties, which can be artificially manipulated by controlling the size and composition of the building blocks [1,2]. Among them, cobalt-based bimetallic clusters have been considered as one of the most interesting systems. For example, it is expected that the position of the dopant atom determines the reactivity, stability, and magnetic properties of doped cobalt clusters.

Early experimental investigations showed that an increase of reactivity can be achieved by doping cobalt clusters with vanadium atoms [3-5]. Later, a reactivity study of manganese doped cobalt clusters showed that clusters composed of manganese and cobalt tend to follow an icosahedral growth sequence, in contrast to pure cobalt clusters, which adopt close-packed structures [6]. Several theoretical studies dealt with the structural and magnetic properties of cobalt-based bimetallic clusters [7-16]. With the ultimate goal to create stable cluster-based materials having desired properties, the effect on the structural, electronic, magnetic, and chemical properties of replacing the central atom in icosahedral Co_{13} was theoretically studied in $Co_{12}TM$ (TM = Ti, V, Cr, Mn, Fe, Co, and Ni) [17]. It was found that the substituted species are more stable than Co_{13}, except for $Co_{12}Ni$, while the magnetic moment of pure cobalt clusters is reduced by the central TM atom substitutions. Recently, these *ab initio* density functional theory calculations have been extended to investigate the structural and magnetic properties of $Co_{12}TM$ with TM = Rh, Pd, and Pt [18].

In contrast to the extensive amount of computational data, there is limited experimental confirmation for the predictions made. Photoionization and photoelectron spectroscopy studies were performed to study the electronic properties of vanadium and manganese doped cobalt clusters [6,19-21]. The magnetism of manganese and vanadium doped cobalt clusters has been studied using deflection experiments [22,23]. It was revealed that the per atom average moments of Co_nMn_m increase with increasing Mn concentration, in contrast to bulk CoMn. Meanwhile, for vanadium doped cobalt clusters, a reduction of the average magnetic moments with increasing V concentration was observed, consistent with what is expected in bulk CoV.

Very few experiments have been done so far that provide direct evidence on the relative stability of TM doped cobalt clusters. In an effort to bridge this gap, we performed a systematic photofragmentation study on mass-selected $\mathrm{Co}_n\mathrm{TM}^+$ ($n = 8 - 18$, TM = Ti, V, Cr, and Mn) clusters to explore their fragmentation behavior. Additionally, the dissociation channels of $\mathrm{V}_n\mathrm{Co}^+$ ($n = 9 - 16$) clusters are investigated. The effect of doping on the relative stability and the dissociation pathways are discussed in relation with experimental and theoretical data available in literature.

4.2 Experimental setup

Details about the experimental setup are discussed in chapter 2. In brief, the cobalt and vanadium based bimetallic clusters, $\mathrm{Co}_n\mathrm{TM}^+$ and $\mathrm{V}_n\mathrm{Co}^+$, are produced in the pulsed dual-target dual-laser vaporization source, and studied in the HRTOF mass spectrometer. The clusters of interest are mass-selected by the mass gate, and then exposed to the second harmonic of a Q-switched Nd:YAG laser (Spectra Physics GCR 150). The laser is slightly defocused to have a beam diameter of 15 mm and fluences in the range of $10-80$ mJ/cm^2 are used for the photodissociation. The delayed fragments and the remaining parent clusters are recorded by the detector.

4.3 Results and discussions

Table 4.1 gives an overview of the investigated parent clusters $\mathrm{Co}_n\mathrm{TM}^+$ (TM = Ti, V, Cr, Mn and $n = 8-18$) and the recorded fragments. It is obvious that the evaporation of a cobalt atom is the preferred dissociation channel for clusters with TM = Ti and V. In contrast, the loss of the dopant atom is found to be the favored one for $\mathrm{Co}_n\mathrm{TM}^+$ with TM = Cr and Mn, except for $\mathrm{Co}_{13}\mathrm{Cr}^+$. It should be mentioned that no fragments could be measured at laser fluences lower than 10 mJ/cm^2. Similar behavior has been observed for TM oxide and silicon carbide clusters where also a high laser fluence was required to achieve significant amounts of dissociation [24,25]. Additional channels, corresponding to the loss of two or three Co atoms, are detected for the large cluster sizes except $\mathrm{Co}_{12}\mathrm{V}^+$. Some insight into the underlying mechanisms of the dissociation processes can

Table 4.1: *Fragment ions observed from photofragmentation of TM doped cobalt clusters, $Co_n TM_m^+$. The sizes of the parent and fragment clusters are labeled as n.m. The most intense fragment is listed in bold font. Parallel channels are marked with an asterisk.*

Parent clusters	Fragment ions (TM = Ti)	Fragment ions (TM = V)	Fragment ions (TM = Cr)	Fragment ions (TM = Mn)
8.1	7.1		**8.0**, 7.0	8.0
9.1	**8.1**, 7.1		**9.0**, 8.0	**9.0**, 8.0
10.1	**9.1**, 8.1	**9.1**, 8.1	**10.0**, 9.0	**10.0**, 9.0
11.1	**10.1**, 9.1	**10.1**, 9.1	**11.0**, 10.0	**11.0**, 10.0
12.1	**11.1**, 10.1	11.1	**12.0**, 11.0	**12.0**, 11.0
13.1	**12.1**, 11.1	**12.1**, 11.1	**12.1***, 13.0*	**13.0**, 12.0
14.1	**13.1**, 12.1	**13.1**, 12.1	**14.0***, 13.1*	**14.0**, 13.0
15.1	**14.1**, 13.1	**14.1**, 13.1	**15.0***, 14.1*	**15.0**, 14.0, 13.0
16.1		**15.1**, 14.1	**16.0***, 15.1*	**16.0**, 15.0, 14.0
17.1		**16.1**, 15.1	**17.0***, 16.1*	**17.0**, 16.0, 15.0
18.1		**17.1**, 16.1, 15.1		**18.0**, 17.0, 16.0

be obtained from the laser fluence dependence of the fragment ion intensities. These additional fragmentation channels are produced more efficiently at higher laser fluence, which implies that they likely result from sequential dissociation processes. Detailed investigation of the fluence dependence of the fragmentation of Co_nV^+ clusters, which will be discussed in chapter 5, also confirmed the presence of sequential processes. Parallel channels are found for Co_nCr^+ with $n \geq 12$. Fragmentation energies of pure Co_n clusters have been found to be in the 2.93−3.94 eV range [26]. Supposing that this range is a good proxy for the dissociation energies of the Co_nTM^+ ($n = 10 - 20$) clusters, the energy of a single 532 nm photon (2.34 eV) is insufficient to induce the dissociation [27,28]. There are thus good arguments to believe that under the current experimental conditions at least two photons are required to trigger fragmentation.

It is known that a high abundance of a specific cluster in a mass spectrum does not always reflect a higher stability [24,25,27,29,30]. In the present study, wherein Co_nTM^+ clusters are first mass selected, stability information is extracted from the relative intensities of the fragment to parent signals after laser irradiation and not from the intensity of the clusters as produced in the source. The photon induced dissociation tends to terminate at fragment ions

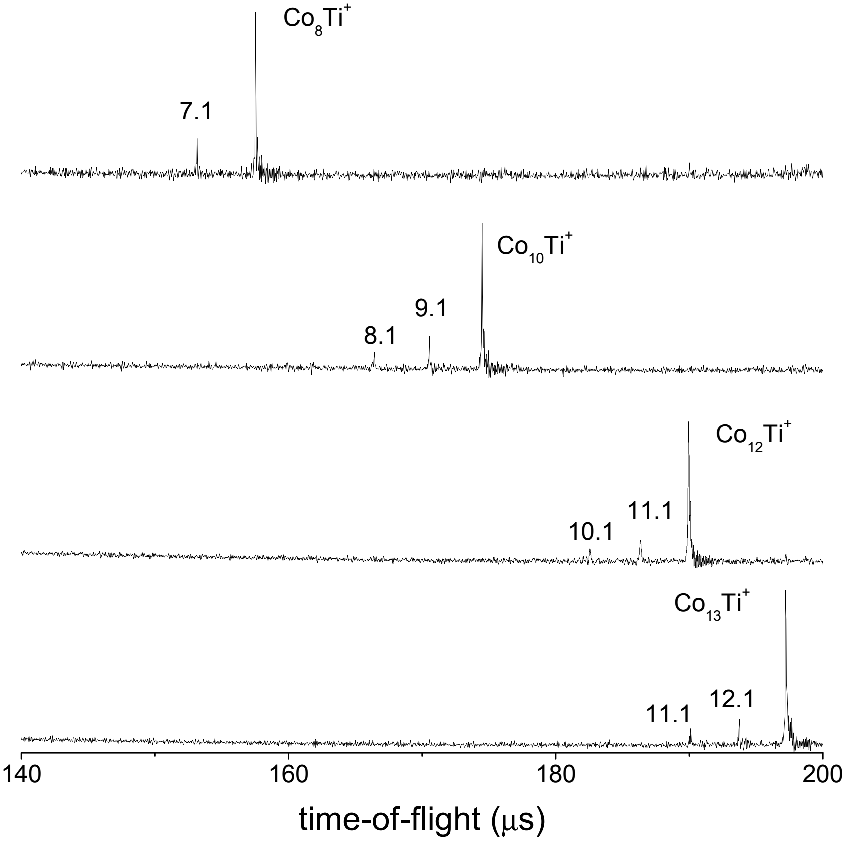

Figure 4.1: *Time-of-flight spectra of photofragmented* Co_8Ti^+, $Co_{10}Ti^+$, $Co_{12}Ti^+$, *and* $Co_{13}Ti^+$ *clusters using a laser fluence of 75 mJ/cm*^{2}. *The highest intensity peaks correspond to the remaining parent clusters. The fragment* $Co_nTi_m^+$ *clusters are labeled as n.m.*

with enhanced stabilities [31]. The dissociation is assumed to take place on the ground-state potential energy surface. The charge of the parent cation cluster favorably resides on the larger fragment species, which usually have lower ionization potentials. It is in line with our experimental observations, where two likely fragmentation channels for $\mathrm{Co}_n\mathrm{TM}^+$ are

$$\mathrm{Co}_n\mathrm{TM}^+ \rightarrow \mathrm{Co}_{n-1}\mathrm{TM}^+ + \mathrm{Co}$$

Table 4.2: *Comparison of calculated and measured binding energies for Co−TM dimers.*

Co−TM	Calculated binding energies energies (eV/atom)	Measured binding energies (eV/atom)
Co_2	1.45 [9,12], 1.12 [10], 1.43 [16]	1.72 [32], 1.32 [26]
Co−Ti	1.7 [10]	2.4 [33]
Co−V	1.53 [9], 1.19 [10], 1.51 [12]	−
Co−Cr	0.67 [10], 0.82 [13]	−
Co−Mn	0.96 [10], 1.09 [11,12]	−

$$\mathrm{Co}_n\mathrm{TM}^+ \rightarrow \mathrm{Co}_n^+ + \mathrm{TM}$$

Although the dissociation energies are not directly measured, the relative stability of $\mathrm{Co}_{n-1}\mathrm{TM}^+$ clusters compared to Co_n^+ can be quantitatively understood. The binding energies, E_b, of Co_n^+ and $\mathrm{Co}_{n-1}\mathrm{TM}^+$ can be approximated as

$$\begin{aligned} E_b(\mathrm{Co}_n^+) &= (n-1)E(\mathrm{Co}) + E(\mathrm{Co}^+) - E(\mathrm{Co}_n^+) \\ E_b(\mathrm{Co}_{n-1}\mathrm{TM}^+) &= (n-2)E(\mathrm{Co}) + E(\mathrm{Co}^+) + E(\mathrm{TM}) - E(\mathrm{Co}_{n-1}\mathrm{TM}^+) \end{aligned}$$

with E the total energy. If the first channel is energetically preferred over the second, $E(\mathrm{Co}_{n-1}\mathrm{TM}^+) - E(\mathrm{TM}) < E(\mathrm{Co}_n^+) - E(\mathrm{Co})$ and consequently, $\mathrm{Co}_{n-1}\mathrm{TM}^+$ is relatively more stable than Co_n^+.

Figures 4.1 and 4.2 present the selected photofragmentation spectra recorded for $\mathrm{Co}_n\mathrm{Ti}^+$ and $\mathrm{Co}_n\mathrm{V}^+$ clusters, respectively. The only dissociation channel found is the evaporation of a single Co atom (see also Table 4.1), which is also the preferred fragmentation channel of pure Co_n^+ clusters [26]. Sequential channels, via the loss of a second and a third Co atom, are observed as aforementioned. No evidence for the evaporation of the dopant atom is found. This indicates that the Ti−Co and V−Co bonds in the clusters are stronger than the Co−Co ones, which consequently results in the relatively more stable Ti- and V-substituted clusters than their pure Co counterparts. This argument is supported by the measured and calculated binding energies of Co−TM dimers, which are listed in Table 4.2. The measured binding energy of Co_2 (1.72 eV [32]) is much smaller than that of TiCo (2.4 eV [33]). Various calculations have also confirmed that the binding energies of Ti−Co and V−Co bonds are higher than those of Co−Co [8,10,16]. In addition *ab initio* studies of small $\mathrm{Co}_n\mathrm{V}$ clusters demonstrated that the binding energies of $\mathrm{Co}_n\mathrm{V}$ tend to be slightly larger than those of pure

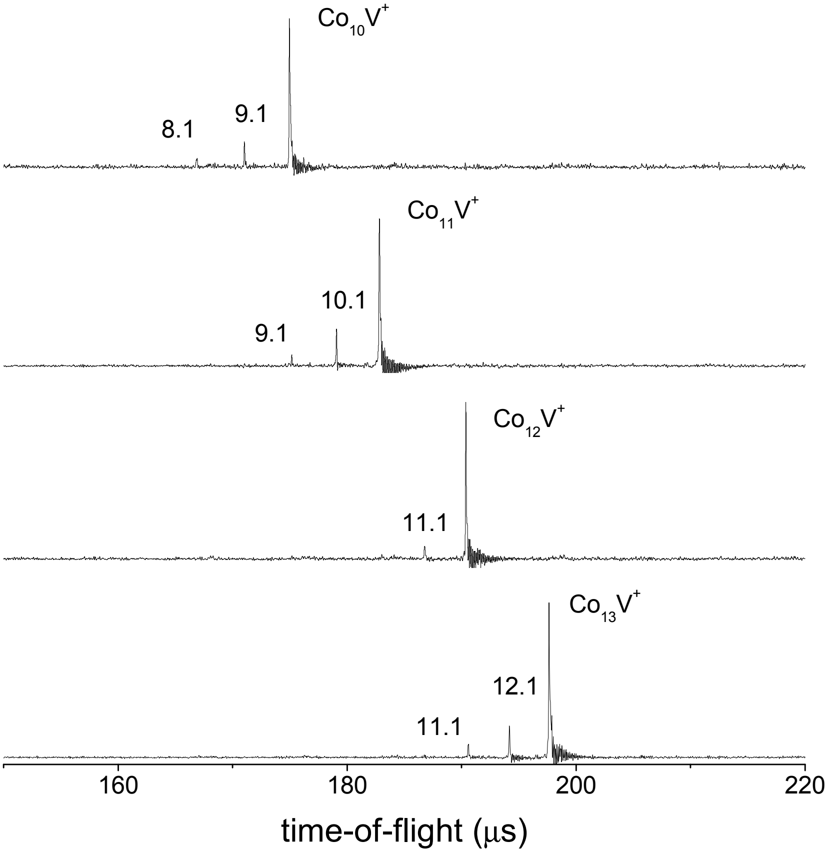

Figure 4.2: *Time-of-flight spectra of photofragmented $Co_{10}V^+$, $Co_{11}V^+$, $Co_{12}V^+$, and $Co_{13}V^+$ clusters using a laser fluence of 75 mJ/cm^2. The highest intensity peaks correspond to the remaining parent ions, while the labels denote fragment sizes. The fragment $Co_nV_m^+$ clusters are labeled as n.m.*

Co_{n+1} with $n < 9$ [12]. An earlier theoretical investigation on Co_{12}TM showed an enhanced stability for substitutional doping of a Ti atom into the center of an icosahedral Co_{13} cluster [17].

An interesting feature is the particular dissociation behavior of $Co_{12}V^+$. While other clusters can be fragmented at the fluence threshold $\sim$ 20 mJ/cm^2, the dissociation of $Co_{12}V^+$ is only possible using fluences above 55 mJ/cm^2.

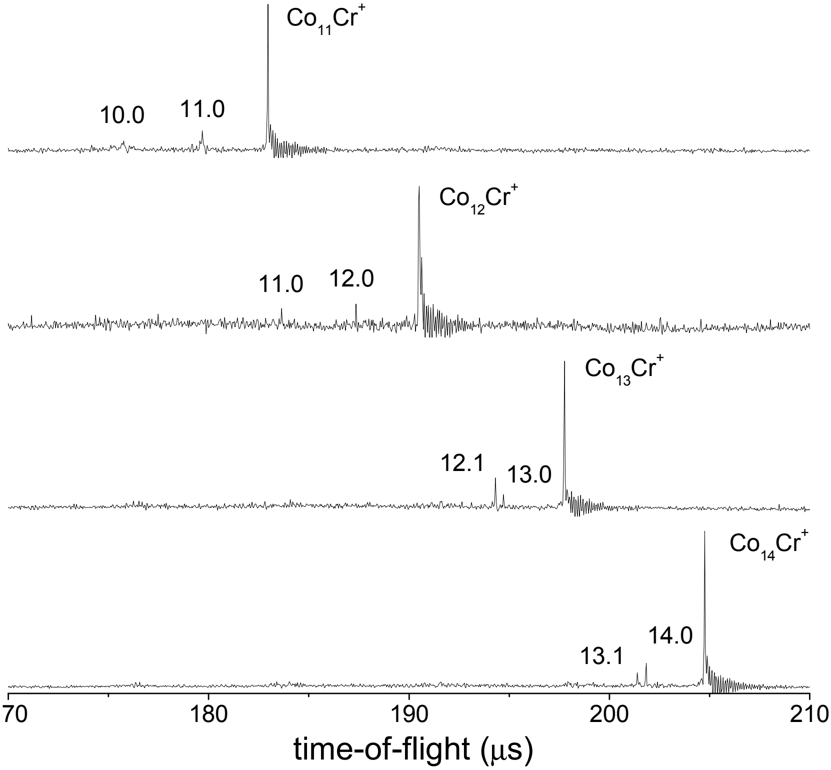

Figure 4.3: *Time-of-flight spectra of photofragmented* $Co_{11}Cr^+$*,* $Co_{12}Cr^+$*,* $Co_{13}Cr^+$*, and* $Co_{14}Cr^+$ *clusters using a laser fluence of 75 mJ/cm*^{2}*. The highest intensity peaks correspond to the remaining parent ions, while the labels denote fragment sizes. The fragment* $Co_nCr_m^+$ *clusters are labeled as n.m.*

Moreover, even for a fluence up to 90 mJ/cm^2, no sequential dissociation channels are recorded, indicating that $\mathrm{Co}_{12}\mathrm{V}^+$ has the highest stability among the studied V doped clusters. Details about the particular stability of $\mathrm{Co}_{12}\mathrm{V}^+$ will be discussed in chapter 5.

Figures 4.3 and 4.4 show time-of-flight spectra of selected Cr- and Mn-doped Co cluster cations after photofragmentation. It appears that the fragmentation behavior of $\mathrm{Co}_n\mathrm{Cr}^+$ and $\mathrm{Co}_n\mathrm{Mn}^+$ is very different from that of Ti and V doped Co clusters: the major fragmentation channels favor the loss of the dopant atom to form Co_n^+. The only exception is $\mathrm{Co}_{13}\mathrm{Cr}^+$, which prefers dissociation

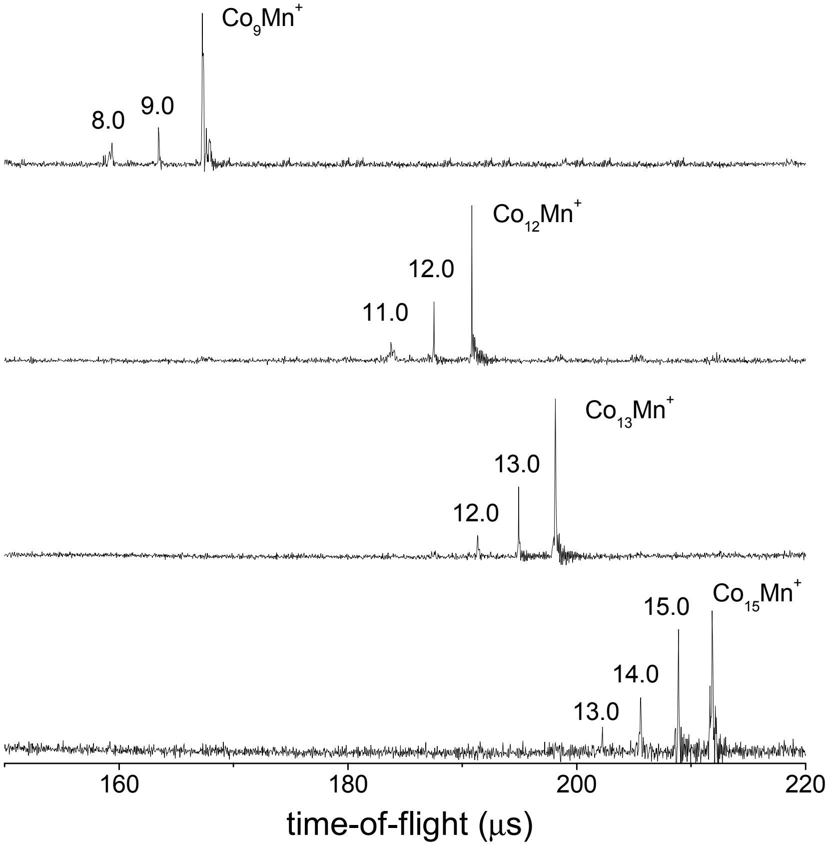

Figure 4.4: *Time-of-flight spectra of photofragmented* Co_9Mn^+, $Co_{12}Mn^+$, $Co_{13}Mn^+$, *and* $Co_{15}Mn^+$ *clusters using a laser fluence of 75* mJ/cm^2. *The highest intensity peaks correspond to the remaining parent ions, while the labels denote fragment sizes. The fragment* $Co_nMn_m^+$ *clusters are labeled as n.m.*

into $Co_{12}Cr^+$, and fragmentation into Co_{13}^+ appears as a minor parallel channel. Sequential channels, via the consecutive losses of Co atoms, are recorded for Co_nCr^+ with $n = 8-12$ and Co_nMn^+ with $n = 9-18$ (see also Table 4.1). It is manifested that in general the Co_nCr^+ and Co_nMn^+ clusters are relatively less stable than the Co_{n+1}^+ clusters, which could be interpreted by the larger binding energy of Co−Co over those of Cr−Co and Mn−Co [11-13] as shown in Table 4.2. These observations are in agreement with the calculated binding energies of Co_nCr and Co_nMn clusters compared to those of Co_{n+1} with $n = 1 - 8$ [12,13]. Moreover, it is remarkable that the fragment peaks for Co_nMn^+ are much more intense than that for the other dopants, which could be due to a relatively higher photon absorption probability.

The dissociation behavior of $Co_{13}Cr^+$ is exceptional. As aforementioned, while the other Co_nCr^+ clusters fragment into Co_n^+ and a neutral Cr atom, $Co_{13}Cr^+$ favors dissociation via the loss of a Co atom, implying that $Co_{12}Cr^+$ is more stable than Co_{13}^+. Parallel channels, corresponding to the loss of neutral Cr and Co atoms, are detected for larger Co_nCr^+ with $n > 12$, which may be related to a minor energy difference for dissociation channels involving the loss of either a Co or a Cr atom. The exceptional behavior of $Co_{12}Cr^+$ among all $Co_{12}TM^+$ clusters could be related to the enhanced stability of the corresponding neutral $Co_{12}Cr$, which is computationally predicted to have an icosahedral structure with the Cr atom at the central position [17]. Noting that the ground state structure of Co_{13} has a HCP geometry [8,9,20], one might expect that the enhanced stability of $Co_{12}Cr^+$ is related to a structural transformation with regard to Co_{13}^+. The Cr release as preferred fragmentation channel of $Co_{12}Cr^+$ does not necessarily imply that Cr is located in a low-coordinated position. The (multiple) photon absorption involves a lot of energy compared to the initial vibrational energy in the cluster. After photon absorption, the clusters are highly excited and atomic permutations can take place before fragmentation via the preferred dissociation channels [29]. Consequently, the preferred dissociation channel provides relative stability information about the fragments, but no structural information about the mother clusters [24-25,27].

For Co_nCr^+ with $n \geq 13$, the observed parallel dissociation channels indicate that the additional Co atoms might be attached onto the surface of $Co_{12}Cr^+$. Nevertheless, not only Cr, but also single V and Mn substitution to produce $Co_{12}V$ and $Co_{12}Mn$ have been believed to initiate a HCP-to-icosahedron structural transformation [8,11,16,34]. It is obvious from reactivity measurements and theoretical calculations that V prefers the center site of the Co cage, whereas Mn was shown to substitute a Co atom at the surface position [13]. In contrast to the enhanced stability of $Co_{12}Cr^+$, the destabilization of Co_{13}^+ by Mn substitution is confirmed in our photofragmentation experiments, where Co_nMn^+ favors dissociating into Co_n^+ and a neutral Mn atom.

In order to obtain a comprehensive understanding of Co−TM bonds, the dissociation behavior of cobalt doped TM clusters is further investigated. For this purpose, V_nCo^+ clusters with $n = 9-16$ are produced and photofragmented at 532 nm laser light. Table 4.3 lists the V_nCo^+ clusters and their recorded

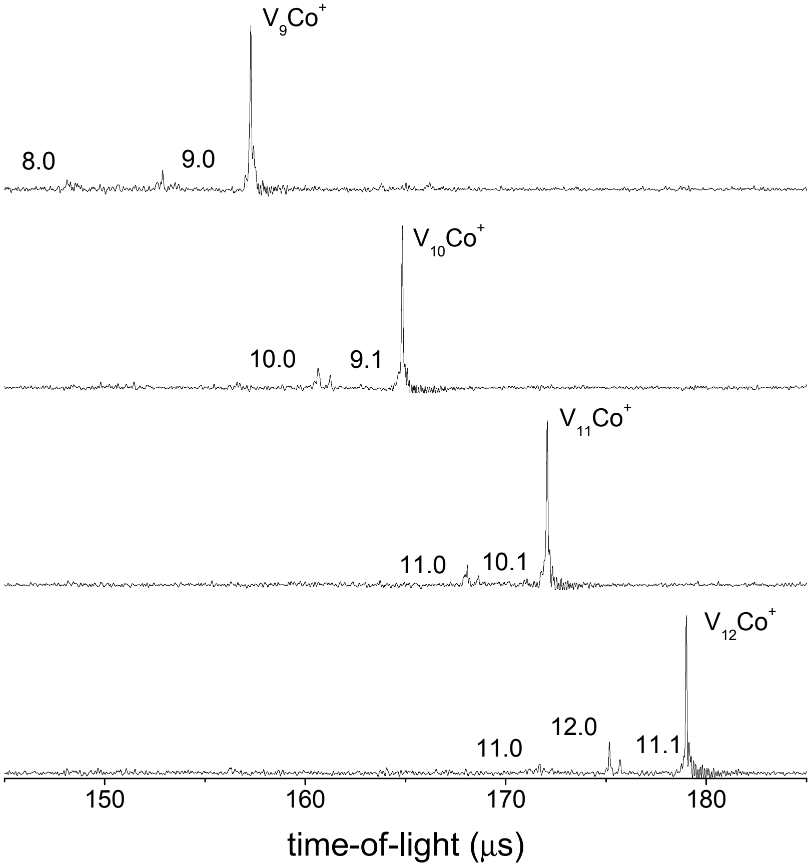

Figure 4.5: *Time-of-flight spectra of photofragmented* V_9Co^+, $V_{10}Co^+$, $V_{11}Co^+$, *and* $V_{12}Co^+$ *clusters using a laser fluence of 75 mJ/cm*^{2}. *The highest intensity peaks correspond to the remaining parent ions, while the labels denote fragment sizes. The fragment* $V_nCo_m^+$ *clusters are labeled as n.m.*

fragment ions. Selected photofragmentation spectra of $\mathrm{V}_n\mathrm{Co}^+$ are presented in Fig. 4.5. Obviously, for all studied $\mathrm{V}_n\mathrm{Co}^+$ the loss of Co is found to be the major dissociation channel, which is identical to the dissociation behavior of $\mathrm{Co}_n\mathrm{V}^+$. This observation can be understood by using a similar interpretation for V doped Co_n^+ clusters, where the V−Co bond is predicted to be weaker compared to the V−V one [9,35].

Table 4.3: *Fragment ions observed from photofragmentation of Co doped V clusters, $V_nCo_m^+$. The sizes of the parent and fragment clusters are labeled as n.m. The most intense channel is in listed bold font.*

Parent clusters	Fragment ions
9.1	**9.0**, 8.0
10.1	**10.0**, 9.1
11.1	**11.0**, 10.1
12.1	**12.0**, 11.1, 11.0
13.1	**13.0**, 12.1, 12.0
14.1	**14.0**, 13.1, 13.0, 12.1
15.1	**15.0**, 14.1, 14.0, 13.0
16.1	**16.0**, 15.0

4.4 Conclusions

The stability of mass-selected TM doped cobalt cluster cations with TM = Ti, V, Cr, and Mn are systematically studied in photofragmentation experiments using 532 nm laser light. All Co_nTi^+ and Co_nV^+ clusters dissociate into $Co_{n-1}TM^+$ and a neutral Co atom, while most of Co_nCr^+ and Co_nMn^+ clusters prefer dissociating into Co_n^+ and the neutral dopant atom. Sequential dissociation processes via the consecutive loss of Co atoms are recorded at high laser fluence. It is suggested that Ti and V substitutions enhance the stability of Co clusters whereas Co_nCr^+ and Co_nMn^+ clusters are less stable than the Co_{n+1}^+ counterparts. Exceptional fragmentation behavior among Co_nCr^+ is observed for $Co_{13}Cr^+$, which prefers dissociating via loss of a Co atom rather than via loss of a Cr atom. This supports the theoretical prediction of the enhanced stabilities of the neutral counterparts $Co_{12}Cr$, which is believed to be icosahedral with the dopant atom at the central site. Finally, the photofragmentation behavior of TM-rich Co clusters, V_nCo^+, is examined. It is shown that the loss of a Co atom is still the lowest energy dissociation channel, which confirms the binding rule of Co−TM bonds throughout the dissociation behaviors of TM doped Co clusters.

References

1. J. Bansmann, S. H. Baker, C. Binns, J. A. Blackman, J. P. Bucher, J. Dorantes-Davila, V. Dupuis, L. Favre, D. Kechrakos, A. Kleibert, K. H.

Meiwes-Broer, G. M. Pastor, A. Perez, O. Toulemonde, K. N. Trohidou, J. Tuaillon, and Y. Xie, Surf. Sci. Rep. **56,** 189 (2005).

2. R. Ferrando, J. Jellinek, and R. L. Johnston, Chem. Rev. **108,** 845 (2008).
3. S. Nonose, Y. Sone, K. Onodera, S. Sudo, and K. Kaya, J. Phys. Chem. **94,** 2746 (1990).
4. A. Nakajima, T. Kishi, T. Sugioka, Y. Sone, and K. Kaya, J. Phys. Chem. **95,** 6833 (1991).
5. N. Fujima and T. Yamaguchi, J. Phys. Soc. Jpn. **61,** 1724 (1992).
6. G. M. Koretsky, K. P. Kerns, G. C. Nieman, M. B. Knickelbein, and S. J. Riley, J. Phys. Chem. A **103,** 1997 (1999).
7. M. Pereiro, D. Baldomir, J. E. Arias, Phys. Rev. B **80,** 075412 (2009).
8. S. Datta, M. Kabir, S. Ganguly, B. Sanyal, T. Saha-Dasgupta, and A. Mookerjee, Phys. Rev. B **76,** 014429 (2007).
9. S. Datta, M. Kabir, T. Saha-Dasgupta, and A. Mookerjee, Phys. Rev. B **80,** 085418 (2009).
10. G. L. Gutsev, M. D. Mochena, P. Jena, C. W. Bauschlicher, and H. Partridge III, J. Chem. Phys. **121,** 6785 (2004).
11. S. Ganguly, M. Kabir, S. Datta, B. Sanyal, and A. Mookerjee, Phys. Rev. B **78,** 014402 (2008).
12. N. Shen, J. Wang, and L. Zhu, Chem. Phys. Lett. **467,** 114 (2008).
13. N. Shen, Y. Wang, S. Chen, and J. Wang, Front. Phys. China **4,** 408 (2009).
14. P. Wu, L. F. Yuan, and J. L. Yang, J. Phys. Chem. A **112,** 12320 (2008).
15. Q. L. Lu, L. Z. Zhu, L. Ma, and G. H. Wang, Phys. Lett. A **350,** 258 (2001).
16. J. Lv, F.-Q. Zhang, J.-F. Jia, X.-H. Xu, and H.-S. Wu, J. Mol. Struct. THEOCHEM **955,** 14 (2010).
17. Y. Jinlong, X. Chuanyun, X. Shangda and W. Kelin, Phys. Rev. B **48,** 12155 (1993).
18. F. Aguilera-Granja, R. C. Longo, L. J. Gallego, and A. Vega, J. Chem. Phys. **132,** 184507 (2010).

19. K. Hoshino, T. Naganuma, K. Watanabe, Y. Konishi, A. Nakajima, and K. Kaya, Chem. Phys. Lett. **239,** 369 (1995).

20. S. R. Liu, H. J. Zhai, and L. S. Wang, Phys. Rev. B **64,** 153402 (2001).

21. A. Pramann, K. Koyasu, and A. Nakajima, J. Phys. Chem. A **106,** 2483 (2002).

22. S. Yin, R. Moro, X. Xu, and W. A. de Heer, Phys. Rev. Lett. **98,** 113401 (2007).

23. M. B. Knickelbein, Phys. Rev. B **75,** 014401 (2007).

24. J. B. Jaeger, T. D. Jaeger, and M. A. Duncan, J. Phys. Chem. A **110,** 9310 (2006).

25. K. S. Molek, Z. D. Reed, A. M. Ricks, and M. A. Duncan, J. Phys. Chem. A **111,** 8080 (2007).

26. D. A. Hales, C. X. Su, L. Lian, and P. B. Armentrout, J. Chem. Phys. **100,** 1049 (1994).

27. S. Bhattacharyya, T. T. Nguyen, J. De Haeck, K. Hansen, P. Lievens, and E. Janssens, Phys. Rev. B **87**, 054103 (2013).

28. K. Hansen, A. Herlert, L. Schweikhard, and M. Vogel, Phys. Rev. A **73,** 063202 (2006).

29. C. J. Bibble, S. T. Akin, S. Ard, C. P. Fowler, and M. A. Duncan, J. Phys. Chem. A **116,** 5398 (2012).

30. A. M. Knight, B. Bandyopadhyay, C. L. Anfuso, K. S. Molek, M. A. Duncan, Int. J. Mass Spectrom. **304,** 29 (2011).

31. K. Hansen and U. Näher, Phys. Rev. A **60,** 1240 (1999).

32. A. Kant and B. Strauss, J. Chem. Phys. **41,** (1964) 3806.

33. E. M. Spain and M. D. Morse, J. Phys. Chem **96,** 2476 (1992).

34. S. Datta, M. Kabir, A. Mookerjee, and T. Saha-Dasgupta, Phys. Rev. B **83,** 075425 (2011).

35. A. Kant and S. S. Lin, J. Chem. Phys. **51,** 1644 (1969).

Chapter 5

Exceptional stability of $Co_{12}V^+$ clusters

The results presented in this chapter are based on:

Photofragmentation of mass-selected vanadium doped cobalt cluster cations
N. T. Tung, E. Janssens, S. Bhattacharyya, and P. Lievens
European Physical Journal D **67**, 41 (2013).

Abstract

Earlier photodissociation spectra showed an exceptional stability of the $Co_{12}V^+$ cluster. In this chapter, the stability of $Co_{12}V^+$ is examined in detail. Particularly, the size and composition dependent dissociation behavior of mass-selected vanadium doped cobalt cluster cations ($Co_{n-1}V^+$, $n = 11 - 21$ and $Co_{13-m}V_m^+$, $m = 0 - 3$) is studied as a function of laser fluence. The recorded fragmentation spectra show that all studied clusters prefer dissociation by loss of a cobalt atom. Sequential cobalt atom evaporation is found at higher laser fluences. No dissociation channel involving vanadium loss is observed, consistent with the V$-$Co bonds being stronger than the Co$-$Co bonds. $Co_{12}V^+$, which was predicted to have an icosahedral symmetry, is found to be the most stable cluster among the singly vanadium doped species. Consecutive increment of the vanadium concentration along the $Co_{13-m}V_m^+$ ($m = 0-3$) series further confirms the enhanced stability of $Co_{12}V^+$, in excellent agreement with theoretical predictions [Datta *et al.*, Phys. Rev. B **80** (2009) 085418].

5.1 Introduction

One of the earliest studies on the reactivity of bimetallic clusters dealt with the H_2 adsorption on vanadium doped cobalt clusters [1,2]. Since vanadium shows, in contrast to cobalt, a high reactivity toward H_2 [3], one expected to be able to tailor the reactivity by controlling the composition of the bimetallic clusters. In particular, an increase of the reactivity can be achieved by doping the cobalt clusters with vanadium atoms [4]. However, the reactivity of $\mathrm{Co}_{n-m}\mathrm{V}_m$ ($n = 6 - 13$, $m = 0 - 4$) toward H_2 does not change monotonously with m, but shows a strong size and composition dependence. While substituting one Co atom by one V atom increases the reactivity of $\mathrm{Co}_{n-1}\mathrm{V}$ for $n \leq 12$, $\mathrm{Co}_{12}\mathrm{V}$ appears to be extraordinary stable against H_2 adsorption [1]. When more than one atom is substituted by vanadium in the Co_{13} cluster, the reactivity was found to increase again. The adsorption of H_2 on cationic $\mathrm{Co}_{n-m}\mathrm{V}_m^+$ ($n = 2 - 19$, $m = 0 - 2$) clusters shows a similar behavior as the corresponding neutral clusters [2]. Also for $\mathrm{Co}_{n-m}\mathrm{V}_m^+$ with $n > 13$, the first exchange leads to a strong decrease in reactivity compared to Co_n^+ while the second substitution results in a strong increase. The comparable size dependent H_2 adsorption for neutral and cationic vanadium doped cobalt clusters suggests that the low reactivity for $\mathrm{Co}_{12}\mathrm{V}^{0,+}$ clusters is governed not only by the electronic structure of the clusters but also by their geometry [5-8].

Recently, a detailed density-functional-theory study has been performed to explain the extraordinary stability of $\mathrm{Co}_{12}\mathrm{V}$ against H_2 [9]. It was found that $\mathrm{Co}_{12}\mathrm{V}$ is exceptionally stable and its minimum-energy structure prefers to be icosahedral with the vanadium dopant atom at the center, while the pure Co_{13} cluster has a distorted hexagonal symmetry. Further charge-transfer analysis of vanadium doped clusters indicated that the low reactivity of icosahedral $\mathrm{Co}_{12}\mathrm{V}$ is due to the weaker interaction between the hydrogen 1s electron and the 3d orbital of the surface Co atoms to which the H_2 molecule is bonded as compared to the bare Co_{13} cluster [9].

Also, the magnetic properties of cobalt and transition metal doped cobalt clusters have been studied intensively using Stern-Gerlach deflection experiments. It was shown that cobalt clusters have magnetic moments per atom that are larger than the value for bulk cobalt (1.7 μ_B/atom) due to the reduced dimensionality and increased surface-to-volume ratio of clusters [10-13]. For manganese doped cobalt clusters, the per atom average moments of $\mathrm{Co}_n\mathrm{Mn}_m$ are found to increase with Mn concentration, in contrast to bulk CoMn [14,15]. Meanwhile, $\mathrm{Co}_n\mathrm{V}_m$ clusters show a reduction of the average magnetic moments with increasing V doping, consistent with what is expected in bulk CoV [14]. Comparison of the magnetic deflection data with *ab initio* studies allowed to assign the corresponding geometric structures of the clusters [16-18].

No experiments have been performed so far that directly confirm the relative stability of the neutral and cationic $Co_{12}V^{0,+}$ clusters. In this chapter, we present a systematical photofragmentation study on mass-selected vanadium doped cobalt cluster cations. For that purpose, two series of clusters are investigated: i) singly-doped $Co_{n-1}V^+$ ($n = 11-21$) and ii) the 13-atom systems $Co_{13-m}V_m^+$ ($m = 0-3$) with consecutively increased vanadium concentration. Their relative stabilities and dissociation pathways are discussed in relation with experimental and theoretical studies available in literature.

5.2 Results

Details about the experimental setup are described in chapter 2 and section 4.2. Figure 5.1 shows a typical TOF spectrum of the $Co_{n-m}V_m^+$ ($n = 11-21, m = 0-6$) clusters that are produced in the laser vaporization source. The highest peaks correspond to pure Co_n^+ and singly doped $Co_{n-1}V^+$ clusters. $Co_{n-2}V_2^+$ clusters are also clearly present. Intensities of the doped clusters decrease from $m = 1$ to $m = 3$ but increase again for $m = 5$ and $m = 6$. These characteristics of the $Co_{n-m}V_m^+$ TOF spectrum are similar to the findings reported by Nakajima and co-workers [2]. Some of the clusters with high V concentration ($m = 4-6$) are hydrogen contaminated. The hydrogen atoms might come from the target surface and the impurities in the helium gas line.

A selection of photofragmentation spectra recorded for $Co_{n-1}V^+$ is shown in Fig. 5.2. For all $Co_{n-1}V^+$ clusters ($n = 11-21$), the main dissociation channel found corresponds to the evaporation of a single Co atom. Additional channels are observed for higher laser fluences (> 40 mJ/cm^2), producing smaller fragment ions by sequential Co atom evaporation (see 83 mJ/cm^2 spectra in Fig. 5.2). No molecular fragment or neutral vanadium atom loss is detected. All fragmentation channels observed for $Co_{n-1}V^+$ ($n = 11-21$) are included in Table 5.1.

Figure 5.3 shows the variation of the fragment to parent intensity ratio for the primary and sequential dissociation channels as function of the laser fluence. The fluence dependence of $Co_{n-1}V^+$ ($n = 11-21$) shows that no fragments could be measured at low laser fluence. A certain fluence value is required to achieve the dissociation channels. For example, for $Co_{11}V^+$ it takes $\sim$23

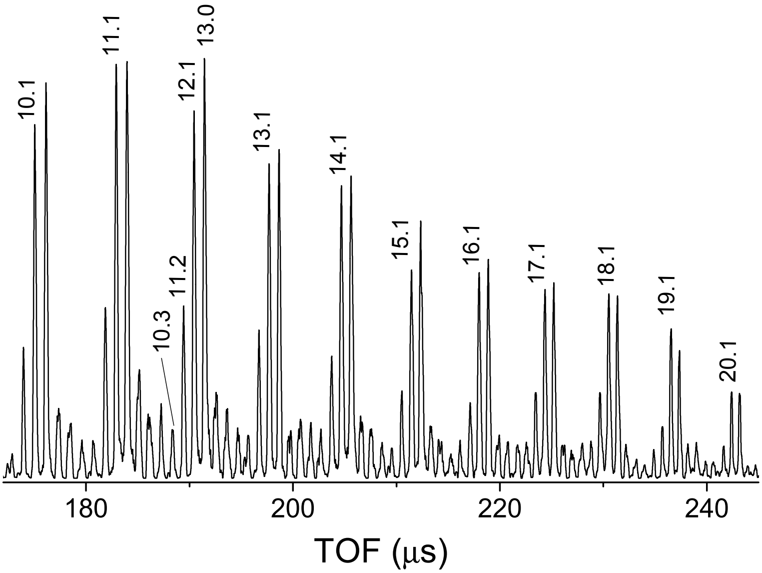

Figure 5.1: *Typical TOF spectrum of the* $Co_{n-m}V_m$ *clusters produced by laser vaporization. The peaks are labeled by* $(n-m, m)$. *The highest intensities correspond to pure* Co_n^+ *and singly doped* $Co_{n-1}V^+$ *clusters.*

mJ/cm^2 to stimulate the primary channel and a fluence of at least 45 mJ/cm^2 is required to see the secondary one. Similarly, minimal fluences required for photodissociation are ~32 mJ/cm^2 and ~48 mJ/cm^2 for $Co_{13}V^+$, and ~22 mJ/cm^2 and ~35 mJ/cm^2 for $Co_{16}V^+$, respectively. For $Co_{19}V^+$, it takes ~32 mJ/cm^2, 47 mJ/cm^2, and 59 mJ/cm^2 to observe the primary, secondary, and tertiary channel, respectively. Similar behavior has been discussed in previous work where high laser fluences are necessary to observe significant amounts of dissociation [19-25]. The secondary and tertiary fragments are also produced more efficiently at higher laser fluence, implying that they are sequential dissociation processes. If they would result from the same primary parents, their intensity ratios would be independent of the laser fluence.

As for most of the studied clusters, the fluence dependence of $Co_{13}V^+$, $Co_{16}V^+$, and $Co_{19}V^+$, is not linear, reflecting that the fragmentation processes are governed by multi-photon absorption. However, even if the fluence dependence seems to be linear, as for example for $Co_{11}V^+$ and $Co_{15}V^+$, the fragmentation may be the result of a multi-photon absorption process [26]. Our observation

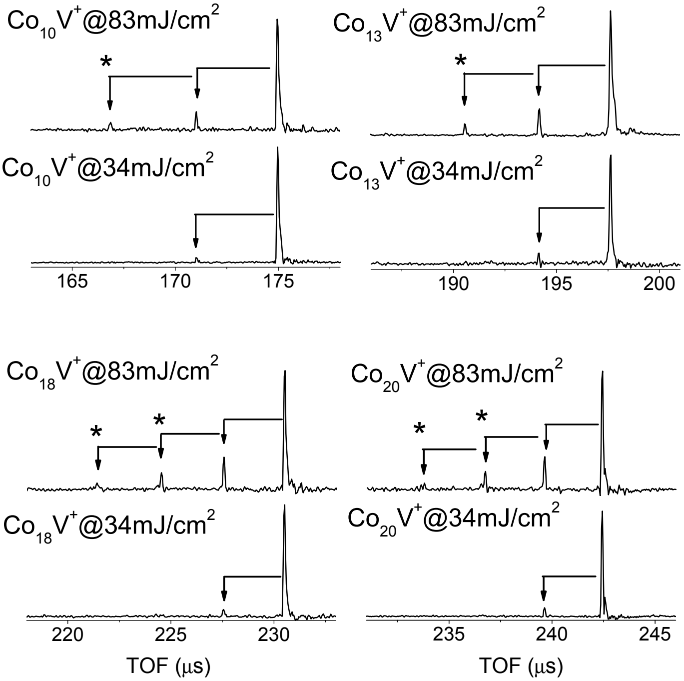

Figure 5.2: *Photofragmentation of* $Co_{10}V^+$, $Co_{13}V^+$, $Co_{16}V^+$, *and* $Co_{20}V^+$ *at laser fluences of 34 and 83 mJ/cm*^{2}. *Dissociation channels (from parent to daughter) are indicated by arrows. Arrows correspond to neutral Co monomer loss. The '*' corresponds to the sequential neutral Co evaporation from the primary and the secondary daughters.*

on the fragmentation pathways of pure cobalt cation clusters (Co_n^+, $n = 7-34$) also indicate that there is only cobalt atom evaporation. These observations agree with earlier experiments using collision induced dissociation [27], where it was shown that Co_n^+ ($n = 2$–18) clusters dissociate exclusively by the loss of single atoms. Fragmentation energies, for cluster sizes relevant to this work ($n =$ 11–18), were found in the range of 3.14–3.94 eV [27]. Note that the excitation energy of the clusters is $E = E_{th} + E_{photon}$, where $E_{th} = n_{eff}\times$ 0.063 eV $=$ $(n-2)\times$ 0.063 eV is the thermal energy and E_{photon} is the excitation energy resulting from the absorption of photons. If we suppose that this range is a good approximation for the dissociation energies of the $\mathrm{Co}_{n-1}\mathrm{V}^+$ ($n = 11-21$) clusters, the energy of a single 532 nm photon (2.34 eV) is insufficient to stimulate the primary and, obviously, also the sequential dissociation processes [28,29]. Hence, we have good arguments to believe that at least two photons

Table 5.1: *Dissociation channels for* $Co_{n-1}V^+$ *(*$n = 11 - 21$*). The primary fragment is the parent cluster of the first sequential dissociation channel while the fragment of the first sequential channel is the parent cluster of the second sequential dissociation channel.*

Parent cluster	Primary channel	1^{st} seq. channel	2^{nd} seq. channel
$Co_{10}V^+$	$Co_9V^+ + Co$	$Co_8V^+ + Co$	-
$Co_{11}V^+$	$Co_{10}V^+ + Co$	$Co_9V^+ + Co$	-
$Co_{12}V^+$	$Co_{11}V^+ + Co$	-	-
$Co_{13}V^+$	$Co_{12}V^+ + Co$	$Co_{11}V^+ + Co$	-
$Co_{14}V^+$	$Co_{13}V^+ + Co$	$Co_{12}V^+ + Co$	-
$Co_{15}V^+$	$Co_{14}V^+ + Co$	$Co_{13}V^+ + Co$	-
$Co_{16}V^+$	$Co_{15}V^+ + Co$	$Co_{14}V^+ + Co$	-
$Co_{17}V^+$	$Co_{16}V^+ + Co$	$Co_{15}V^+ + Co$	-
$Co_{18}V^+$	$Co_{17}V^+ + Co$	$Co_{16}V^+ + Co$	$Co_{15}V^+ + Co$
$Co_{19}V^+$	$Co_{18}V^+ + Co$	$Co_{17}V^+ + Co$	$Co_{16}V^+ + Co$
$Co_{20}V^+$	$Co_{19}V^+ + Co$	$Co_{18}V^+ + Co$	$Co_{17}V^+ + Co$

must be absorbed by the clusters in order to trigger fragmentation.

Figure 5.4 presents the photofragmentation spectra of mass-selected $Co_{13-m}V_m^+$ clusters with increasing vanadium concentration ($m = 0-3$). Again, dissociation occurs via single Co atom loss. Sequential cobalt atom evaporation is observed at higher laser fluences for all compositions but $Co_{12}V^+$. The fragmentation behavior of $Co_{12}V^+$ is exceptional. While other clusters can be fragmented at the fluence threshold $\sim$ 20 mJ/cm^2, the dissociation of $Co_{12}V^+$ is only possible using fluences above 55 mJ/cm^2. Moreover, even for the maximal fluence of 90 mJ/cm^2, it is found that no sequential dissociation channels are recorded for $Co_{12}V^+$. The special character of $Co_{12}V^+$ is further illustrated in Fig. 5.5, where the intensities I_n of the remaining parent normalized to their original intensities are plotted. I_n allows to uncover stability information if the photoabsorption cross section does not show strong size-to-size variations. In that case the intensity of more stable parent clusters remains larger after laser irradiation. The original parent intensity before laser firing is not directly measured in our experiments. However, it can be approximated by summing the intensities of the remaining parent and the fragment ions under the assumption that the positive charge remains with the fragment. As shown in Fig. 5.5, I_n decreases almost monotonically with increasing number of Co atoms in clusters, which might be due to a smoothly increasing photon absorption probability with cluster size. Alternatively, the dissociation energy might gradually decrease

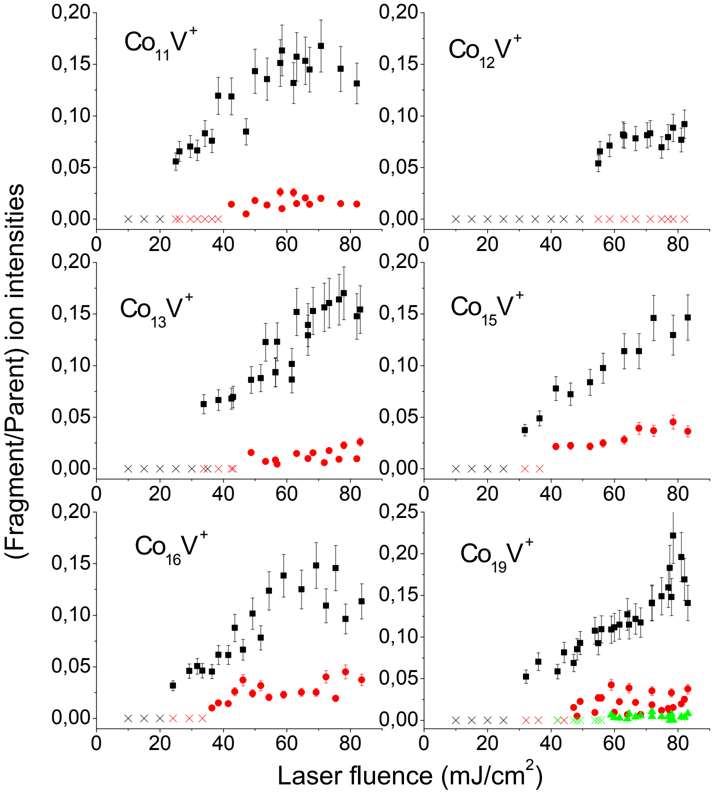

Figure 5.3: *Laser fluence dependence of* $Co_{11}V^+$, $Co_{12}V^+$, $Co_{13}V^+$, $Co_{15}V^+$, $Co_{16}V^+$, *and* $Co_{19}V^+$ *with 532 nm laser light. The black squares represent the primary daughter ion intensities while the red circles and green triangles represent the secondary and tertiary daughter ion intensities, respectively. The crosses indicate that no daughter peak could be observed at these fluences.*

with increasing cluster size. Though, this last option is unlikely, since earlier experiments on pure cobalt cluster cations showed a slight increase of the dissociation energy with size in this size regime [27]. The most striking feature in Fig. 5.5 is the pronounced maximum at $Co_{12}V^+$ followed by a minimum for $Co_{13}V^+$. This suggests an enhanced stability compared to the neighboring sizes for $Co_{12}V^+$, again under the condition that the photoabsorption cross-sections do not strongly vary from size to size in the investigated size range.

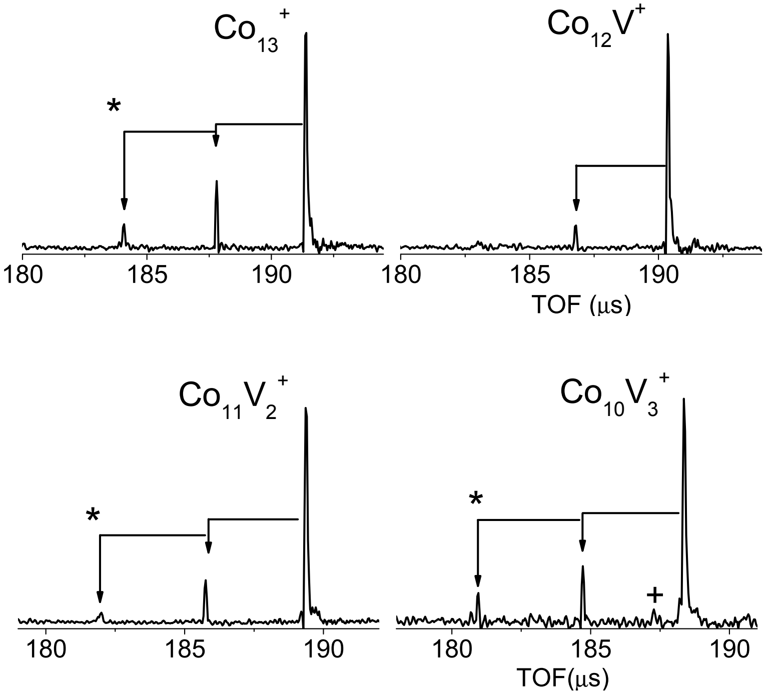

Figure 5.4: *Photofragmentation of $Co_{13-m}V_m^+$ ($m = 0-3$) with 77 mJ/cm^2 laser light. Dissociation channels (from parent to daughter) are indicated by arrows. Arrows correspond to neutral Co monomer loss. The '*' corresponds to the sequential neutral Co evaporation from the first generation daughter. The additional peak marked with '+' corresponds to transmitted $Co_9V_4^+$ clusters.*

In order to compare the relative stability of the 13-atom $Co_{13-m}V_m^+$ clusters, the intensities I_n of their remaining ions normalized to the original intensities are plotted in Fig. 5.6 for fluences of 54, 69 and 82 mJ/cm^2. It can been seen that the stability increases significantly from Co_{13}^+ to $Co_{12}V^+$, but decreases sharply for clusters with multiple vanadium dopant atoms. Similar tendencies observed at different fluences confirm the exceptional stability of $Co_{12}V^+$ compared to the studied neighboring sizes.

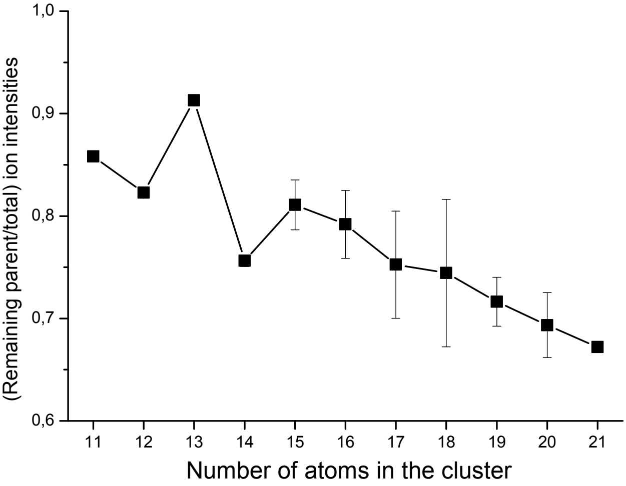

Figure 5.5: *Intensity ratios I_n of the remaining $Co_{n-1}V^+$ ($n = 11 - 21$) ions normalized to their original intensities at 75 mJ/cm^2. The statistical uncertainty of I_n is based on three independently measured data sets.*

5.3 Discussions

To explain the high stability of $\mathrm{Co}_{12}\mathrm{V}^+$ we return to the reactivity studies of $\mathrm{Co}_n\mathrm{V}^{0,+}$ with H_2. Both the neutral and cationic $\mathrm{Co}_{12}\mathrm{V}^{0,+}$ clusters showed a remarkably lower reactivity than the neighboring sizes [1,2]. The peculiar reactivity behavior is more likely attributed to the geometric structure than to the electronic structure of the clusters. This was confirmed by other studies in which it was shown that the ionization energies of $\mathrm{Co}_{n-m}\mathrm{V}_m$ clusters are not anti-correlated with their size-dependent reactivity [7]. In addition, photoelectron spectroscopy demonstrated that $\mathrm{Co}_{12}\mathrm{V}^-$ and Co_{13}^- have a very similar electronic structure [8]. These results confirm the importance of geometric structure to explain the reduced H_2 reactivity of $\mathrm{Co}_{12}\mathrm{V}^{0,+}$ clusters. A plausible explanation for the special reactivity behavior of $\mathrm{Co}_{12}\mathrm{V}^{0,+}$ is a highly symmetric I_h icosahedral cobalt cage structure with a central vanadium atom [1,2,5-9]. Although calculations for cation $\mathrm{Co}_{12}\mathrm{V}^+$ are not available, with the aforementioned picture on the reactivity of $\mathrm{Co}_{12}\mathrm{V}^{0,+}$ one might expect a similar structure for the neutral and the cationic clusters.

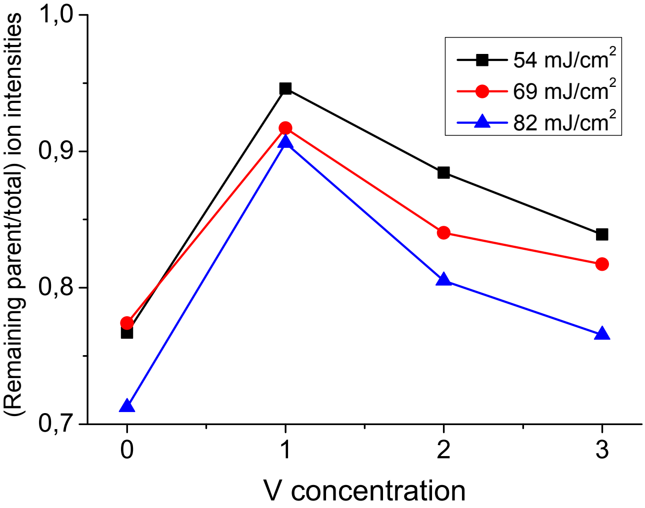

Figure 5.6: *Normalized intensity ratios I_n of $Co_{13-m}V_m^+$ ($m = 0-3$) clusters at 54, 69 and 82 mJ/cm^2.*

It is noteworthy to mention that a high symmetric structure has been predicted for Co_{13}^- based on its photoelectron spectra [30]. Although many clusters of this size have an icosahedral structure, numerous calculations have shown that Co_{13} favors a HCP geometry [17,31-33]. By exchanging one Co atom by one V atom in Co_{13}, the equilibrium structure is expected to change from HCP to an icosahedron [9,18]. Importantly, it brings about a significantly enhanced stability of Co_{12}V compared with Co_{13}, which is interpreted by the enhanced cohesive energy of the CoV dimer over that of Co_2. In the icosahedral Co_{12}V, the number of Co−V bonds is maximal and thus the stability in Co_{12}V is strengthened. For the doped $\text{Co}_{13-m}\text{V}_m^+$ with more than one V atom, it is expected that the favorable structure remains a (distorted) icosahedron with one V atom at the center site and the others at the surface [9]. This motif was predicted for the neutral Co_{11}V_2 and Co_{10}V_3 clusters [9] and is supported by the H_2 reactivity increase of $\text{Co}_{11}\text{V}_2^{0,+}$ and $\text{Co}_{10}\text{V}_3^{0,+}$ compared to $\text{Co}_{12}\text{V}^{0,+}$, respectively [1,2]. The V atom at the surface is likely the reactive center. Despite the presence of a vanadium atom at the surface, we did not observe the loss of vanadium dopant atoms. This can easily be understood by the stronger V−Co bond (theoretical values: 1.51 − 1.53 eV [9,18]) compared to the Co−Co bonds (theoretical value: 1.45 eV [9,18] and experimental value: 1.32 [27]). However, due to the stronger V−V binding (theoretical value: 1.81 eV [9] and experimental one: 2.47 eV [34]), the surface-doped V atoms distort the cluster geometry and, consequently, destabilize the structure. It results in a relatively lower stability of $Co_{13-m}V_m$ clusters when m goes from 1 to 4 [9], which is also observed for the cationic clusters as shown in Fig. 5.6.

5.4 Conclusions

The fragmentation pathways of mass selected $Co_{n-1}V^+$ ($n = 11 - 21$) and $Co_{13-m}V_m^+$ ($m = 0 - 3$) clusters are studied in photodissociation experiments using 532 nm laser light. All clusters dissociate via the loss of single Co atoms. Analysis of laser fluence dependence of the fragment intensities indicates that multiphoton absorption is required for both the primary and sequential fragmentation channels. $Co_{12}V^+$ appears to be the most stable system among the singly doped clusters. A significant enhancement of the stability is found when substituting one Co atom by a V atom in Co_{13}^+. These results corroborate the theoretical prediction on the exceptional stability due to the HCP-to-icosahedron structural transformation triggered by a single endohedral V substitution in Co_{13}.

References

1. S. Nonose, Y. Sone, K. Onodera, S. Sudo, and K. Kaya, J. Phys. Chem. **94**, 2746 (1990).
2. A. Nakajima, T. Kishi, T. Sugioka, Y. Sone, and K. Kaya, J. Phys. Chem. **95**, 6833 (1991).
3. G. C. Bond, Heterogeneous Catalysis (Clarendon Press, Oxford, 1987).
4. R. Ferrando, J. Jellinek, and R. L. Johnston, Chem. Rev. **108**, 845 (2008).
5. N. Fujima and T. Yamaguchi, J. Phys. Soc. Jpn. **61**, 1724 (1992).
6. Y. Jinlong, X. Chuanyun, X. Shangda and W. Kelin, Phys. Rev. B **48**, 12155 (1993).
7. K. Hoshino, T. Naganuma, K. Watanabe, Y. Konishi, A. Nakajima, and K. Kaya, Chem. Phys. Lett. **239**, 369 (1995).
8. A. Pramann, K. Koyasu, and A. Nakajima, J. Phys. Chem. A **106**, 2483 (2002).

9. S. Datta, M. Kabir, T. Saha-Dasgupta, and A. Mookerjee, Phys. Rev. B **80**, 085418 (2009).
10. I. M. L. Billas, A. Chatelain, and W. A. de Heer, Science **265**, 1682 (1994).
11. X. Xu, S. Yin, R. Moro, and W. A. de Heer, Phys. Rev. Lett. **95**, 237209 (2005).
12. M. B. Knickelbein, J. Chem. Phys. **125**, 044308 (2006).
13. F. W. Payne, W. Jang, J. W. Emmert, J. Deng, L. A. Bloomfield, Phys. Rev. B **75**, 094431 (2007).
14. S. Yin, R. Moro, X. Xu, and W. A. de Heer, Phys. Rev. Lett. **98**, 113401 (2007).
15. M. B. Knickelbein, Phys. Rev. B **75**, 014401 (2007).
16. S. Datta, M. Kabir, S. Ganguly, B. Sanyal, T. Saha-Dasgupta, and A. Mookerjee, Phys. Rev. B **76**, 014429 (2007).
17. S. Ganguly, M. Kabir, S. Datta, B. Sanyal, and A. Mookerjee, Phys. Rev. B **78** (2008) 014402.
18. N. Sheng, J. Wang, and L. Zhu, Chem. Phys. Lett. **467**, 114 (2008).
19. J. B. Jaeger, T. D. Jaeger, and M. A. Duncan, J. Phys. Chem. A **110**, 9310 (2006).
20. K. S. Molek, Z. D. Reed, A. M. Ricks, and M. A. Duncan, J. Phys. Chem. A **111**, 8080 (2007).
21. L. Schweikhard, K. Hansen, A. Herlert, M. D. Herraiz Lablanca, and M. Vogel, Eur. Phys. J. D **36**, 179 (2005).
22. N. Veldeman, E. Janssens, K. Hansen, J. De Haeck, R. E. Silverans, and P. Lievens, Faraday Discuss. **138**, 147 (2007).
23. J. S. Piligrim and M. A. Duncan, J. Am. Chem. Soc. **115**, 4395 (1993).
24. J. S. Piligrim and M. A. Duncan, J. Am. Chem. Soc. **115**, 9724 (1993).
25. B. W. Ticknor and M. A. Duncan, Chem. Phys. Lett. **405**, 214 (2005).
26. M. E. Geusic, M. F. Jarrold, T. J. McIlrath, R. R. Freeman, and W. L. Brown, J. Chem. Phys. **86**, 3862 (1987).

27. D. A. Hales, C. X. Su, L. Lian, and P. B. Armentrout, J. Chem. Phys. **100**, 1049 (1994).
28. K. Hansen, A. Herlert, L. Schweikhard, and M. Vogel, Phys. Rev. A **73**, 063202 (2006).
29. M. Vogel, K. Hansen, A. Herlert, L. Schweikhard, Phys. Rev. Lett. **87**, 013401 (2001).
30. S. R. Liu, H. J. Zhai, and L. S. Wang, Phys. Rev. B **64**, 153402 (2001).
31. A. N. Andriotis and M. Menon, Phys. Rev. B **57**, 10069 (1998).
32. C. D. Dong and X. G. Gong, Phys. Rev. B **78**, 020409(R) (2008).
33. M. J. Piotrowski, P. Piquini, and J. L. F. Da Silva, Phys. Rev. B **81**, 155446 (2010).
34. S. P. Walch, C. W. Bauschlicher, B. O. Roos, and C. J. Nelin, Chem. Phys. Lett. **103**, 175 (1983).

Chapter 6

Size-dependent stability of $Co_nO_m^+$ and $Co_{n-1}CrO_m^+$ clusters

The results presented in this chapter are based on:

Influence of chromium doping on the stability and structure of small cobalt oxide clusters
N. T. Tung, N. M. Tam, M. T. Nguyen, P. Lievens, and E. Janssens
Submitted.

Abstract

The stability of mass-selected pure cobalt oxide and chromium doped cobalt oxide cluster cations, $Co_nO_m^+$ and $Co_{n-1}CrO_m^+$ ($n = 2, 3$; $m = 2 - 6$ and $n = 4$; $m = 3 - 8$), has been investigated using photodissociation mass spectrometry. Oxygen-rich $Co_nO_m^+$ clusters ($m \geq n+1$ for $n = 2, 3$ and $m \geq n$ for $n = 4$) prefer to photodissociate via the loss of an oxygen molecule, whereas oxygen poorer clusters favor the evaporation of oxygen atoms. Substituting a single Co atom by a single Cr atom alters the dissociation behavior. All investigated $Co_{n-1}CrO_m^+$ clusters, except $CoCrO_2^+$ and $CoCrO_3^+$, prefer to decay by eliminating a neutral oxygen molecule. $Co_2O_2^+$, $Co_4O_3^+$, $Co_4O_4^+$, and $CoCrO_2^+$ are found to be relatively difficult to dissociate and appear as fragmentation product of several larger clusters, suggesting that they are particularly stable. The geometric structures of pure and Cr doped cobalt oxide species are studied using density

functional theory calculations. Dissociation energies for different evaporation channels are calculated and compared with the experimental observations. The influence of the dopant atom on the structure and the stability of the clusters is discussed.

6.1 Introduction

Transition metal oxides have been a long-standing topic of interest due to their huge potential for applications in catalysis, electronics and magnetic materials [1-5]. Since the last two decades, their corresponding gas phase clusters have been investigated extensively, showing a non-monotonic dependence of properties on the number of constituent atoms and the cluster composition, which results in intriguing chemical and physical properties [6-9].

In this regard, transition metal oxide clusters have artificially been designed to understand the interplay between, on one side, composition, cluster size, structure, shape and, on the other side, their physical and chemical properties. For example, the evolution of electronic structures as a function of composition and charge state of $MM\text{'}O_7^{2-}$ and $M_2O_7^{2-}$ (M, M' = Cr, Mo, W) clusters was studied using the photoelectron spectroscopy [10]. Singly Ti for V substituted $(V_2O_5)_{n-1}(VTiO_5)^-$ ($n = 2 - 4$) cluster anions were shown to have polyhedral caged structures similar to those of their isoelectronic counterparts, the neutral $(V_2O_5)_n$ clusters [11]. The electronic and geometric structures of $MoWO_y^-$ and $MoVO_y^-$ were compared to their pure analogs, $Mo_2O_y^-$, $W_2O_y^-$, and $V_2O_y^-$ ($y = 2 - 5$), using vibrationally resolved anion photoelectron spectroscopy [12, 13]. The electron distribution and the structures of $[(CeO_2)(VO_2)_{1-2}]^+$ and $[(Ce_2O_3)(VO_2)]^+$ clusters were discussed on the basis of infrared vibrational predissociation spectroscopy experiments [14].

Cobalt oxide species have been considered as one of the most fascinating systems, e.g., due to their capability to act as an efficient catalyst for water splitting and CO oxidation [15-18]. Cobalt oxide nanoparticles can also be used in magnetic storage devices and sensor applications [19-21]. Their stability, structures, chemical reactivities, ionization energies, dissociation energies and magnetic properties are engaging and challenging subjects [22-27]. Cobalt-chromium oxide systems, e.g., multiferroic spinel $CoCr_2O_4$, in which both ferroelectricity and ferromagnetism can occur simultaneously, have attracted attention due to their potential to produce a very large magnetoelectric effect [5, 28, 29]. Unfortunately, cobalt-chromium oxide clusters have not been investigated before.

Such studies could provide a better understanding of the interplay between stability, structure, magnetic, and electronic phenomena at the subnanometer size limit.

In this chapter, we set out to investigate the size- and dopant-dependent stability of $Co_nO_m^+$ and $Co_{n-1}CrO_m^+$ ($n = 2, 3$; $m = 2 - 6$ and $n = 4$; $m = 3 - 8$) clusters by means of laser dissociation and mass spectrometry. Density functional theory (DFT) calculations are performed for selected species to further explore the structures and dissociation energies of the clusters.

6.2 Experimental and theoretical methods

Details about the experimental setup are described in chapter 2. For oxide species, helium gas containing 1 % of O_2 is introduced into the source chamber through a pulsed valve after vaporization to initiate cluster formation.

DFT calculations are performed using the hybrid B3P86 functional [30, 31] in conjunction with the cc-pVTZ and cc-pVTZ-pp (pp stands for a set of pseudo-potentials) basis sets as implemented in the Gaussian 09 program [32]. Structural optimization is done at the B3P86/cc-pVTZ-pp level for Co and Cr and the B3P86/cc-pVTZ level for O. Relative energies of the isomers and dissociation energies are determined on the basis of single-point calculations performed at the optimized structures using the full electron cc-pVTZ basis set. The computational results presented in this chapter are mainly the work of Nguyen Minh Tam and Minh Tho Nguyen (KU Leuven, Department of Chemistry).

Table 6.1 shows benchmark data on dimers, illustrating the accuracy and the limitations of the computational approach. Calculated bond lengths (R_e), spin states (M), IPs, and DEs of CoO, CoO^+, CrO, Co_2^+, and Co_2, obtained using different functionals in conjunction with the cc-pVTZ and cc-pVTZ-pp basis sets, are compared with each other and with available experimental values. For metal-oxygen dimers, the computational results are in good agreement with the experimental values and there is almost no difference between the values obtained by cc-pVTZ and cc-pVTZ-pp basis sets. The calculated bond length of CoO is very close to the measured one. The DEs and IPs of oxide dimers, calculated using B3PW91 and PBEPBE, slightly underestimate and overestimate the experimental values, respectively, while those obtained by

Table 6.1: *Calculated bond lengths, spin states, dissociation energies, and ionization potentials of CoO, CoO^+, CrO, Co_2^+ and Co_2 dimers obtained using different functionals in conjunction with both cc-pVTZ and cc-pVTZ-pp (values in the parentheses) basis sets and comparison with available experimental values.*

Dimer	Method	R_e (Å)	M	DE (eV)	IP (eV)
CoO	B3P86	1.57	4	3.78 (3.72)	8.94 (8.90)
	B3LYP	1.59	4	3.60 (3.54)	8.42 (8.36)
	B3PW91	1.58	4	3.58 (3.52)	8.30 (8.27)
	PBEPBE	1.62	4	4.96 (5.06)	8.68 (8.81)
	Exp.	1.63 [33]	–	3.94 [34]	8.71 [35]
CoO^+	B3P86	1.61	5	3.00 (3.16)	
	B3LYP	1.63	5	2.88 (3.06)	
	B3PW91	1.62	5	2.86 (3.04)	
	PBEPBE	1.62	5	4.14 (4.26)	
	Exp.	–	–	3.24 [34]	
CrO	B3P86	1.60	5	4.38 (4.40)	8.85 (8.86)
	B3LYP	1.61	5	4.36 (4.40)	8.30 (8.32)
	B3PW91	1.61	5	4.10 (4.12)	8.29 (8.30)
	PBEPBE	1.61	5	5.20 (5.16)	8.14 (8.16)
	Exp.	–	–	4.38 [34]	–
Co_2^+	B3P86	2.39	2	2.12 (0.88)	
	B3LYP	2.37	2	2.12 (2.54)	
	B3PW91	2.25	2	2.06 (0.56)	
	PBEPBE	2.07	6	3.28 (3.52)	
	Exp.	–	–	2.76 [34]	
Co_2	B3P86	2.27	7 (3)	0.44 (0.84)	6.49 (8.31)
	B3LYP	2.17	7	0.40 (-0.78)	5.96 (4.57)
	B3PW91	2.15	7	0.34 (-0.82)	5.89 (6.39)
	PBEPBE	2.11	5	2.54 (2.20)	7.11 (6.69)
	Exp.	2.31	–	<1.32 [35], 0.7-1.4 [36]	6.26 [37]

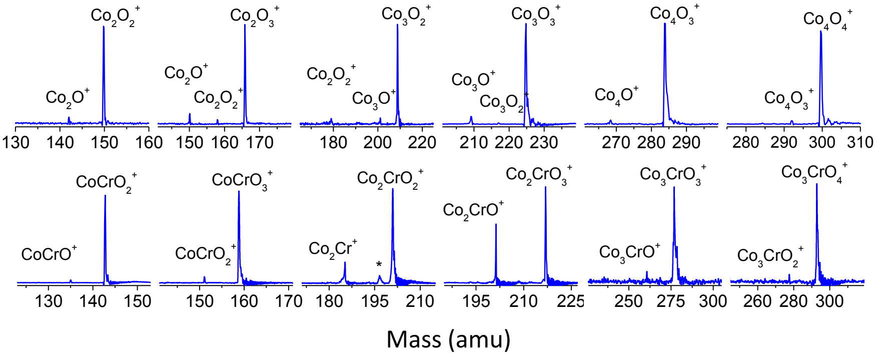

Figure 6.1: *Mass-selected photofragmentation spectra of $Co_nO_{2,3}^+$ and $Co_{n-1}CrO_{2,3}^+$ with 75 mJ/cm^2 of 355 nm laser light. The highest intensity peaks correspond to the remaining parent ions. The peak marked with the asterisk corresponds to transmitted $Cr_2O_6^+$ due to the limited resolution of the mass selector.*

B3P86 and B3LYP are in good agreement with the measurements. The ground-state spin configurations of the neutral and cationic CoO clusters also agree with a previous study [27].

For Co_2 and Co_2^+, the DEs and IPs calculated by cc-pVTZ and cc-pVTZ-pp basis sets are obviously different and depend strongly on the employed functional [38]. This strong functional dependence of the properties of Co_2 was also observed in a recent study of Buendia and Beltran [39]. The values obtained at the cc-pVTZ level are more consistent and in better agreement with the experimental data than those obtained by the cc-pVTZ-pp basis set.

Based on these benchmark data, the B3P86/pVTZ level was selected for the calculation of dissociation energies. The data also show that the DFT approach might be less accurate for describing the metal-metal bonds, but is reliable for metal-oxygen bonds. Since most of the clusters studied in this work only have metal-oxygen bonds (see further), we are confident that the used computational approach is suitable to predict the relative cluster stability.

6.3 Results and discussions

6.3.1 Photofragmentation channels

Figure 6.1 shows selected photofragmentation spectra of pure cobalt oxide and chromium doped cobalt oxide clusters. An overview of the identified dissociation channels of $Co_nO_m^+$ and $Co_{n-1}CrO_m^+$ ($m = 2-6$ for $n = 2, 3$ and $m = 3-8$ for $n = 4$) is given in Table 6.2. We could not mass-select and photofragment $Co_3CrO_6^+$ because of its low intensity. For all studied $Co_nO_m^+$ and $Co_{n-1}CrO_m^+$ clusters, the elimination of either an oxygen atom or an oxygen molecule is found to be the preferred dissociation channel. There is no evidence for evaporation of metal atoms, with the exception of $Co_3O_2^+$ for which the loss of a Co atom is observed as a parallel dissociation channel. Since the detector is unable to record neutral fragments, we can in principle not differentiate between the evaporation of an O_2 molecule or the consecutive evaporation of two O atoms, in which case the fragment is denoted as $[O_2]$. A similar argument is applied for $[O_4]$. In certain cases a laser fluence dependent measurement brought certainty about the direct evaporation of a O_2 molecule.

$Co_2O_2^+$ and $CoCrO_2^+$ are both found to dissociate via the loss of an oxygen atom. $Co_2O_3^+$ dissociates into Co_2O^+ and a small amount of $Co_2O_2^+$. At low laser fluence only the Co_2O^+ fragment is observed, which indicates the direct loss of an O_2 molecule rather than sequential evaporation of two O atoms. The alloy cluster $CoCrO_3^+$, on the other hand, preferentially dissociates via the loss of a single oxygen atom. The oxygen-rich clusters, $Co_2O_{4-6}^+$ and $CoCrO_{4-6}^+$, are found to dissociate via loss of $[O_2]$.

Evaporation of $[O_2]$ is the only recorded dissociation channel of the oxygen rich $Co_3O_{5,6}^+$ and the alloy $Co_2CrO_{2-6}^+$ clusters. The dissociation behavior of the oxygen poorer $Co_3O_{2-4}^+$ clusters is different. $Co_3O_2^+$ dissociates via two parallel channels: O and Co atom evaporation, with similar intensities. $Co_3O_3^+$ also decays via two parallel channels, with the loss of O_2 as preferred channel over atomic O evaporation. $Co_3O_4^+$ fragments solely by eliminating oxygen atoms.

Photodissociation spectra of the clusters with four metal atoms show a similar behavior as the smaller sizes. All studied doped clusters, $Co_3CrO_m^+$ with $m = 3-8$, fragment via the loss of $[O_2]$. The pure cobalt oxide species behave differently. $Co_4O_3^+$ loses $[O_2]$, while $Co_4O_4^+$ evaporates an O atom. $Co_4O_5^+$ has two parallel evaporation channels, corresponding to the loss of O and O_2, with $Co_4O_3^+$ being the most intense fragment.

Table 6.2: *Evaporation channels and fragment ions resulting from photodissociation of* $Co_nO_m^+$ *and* $Co_{n-1}CrO_m^+$*. The most intense fragment is listed first. The slash is used for determined parallel channels. The lost neutrals with brackets indicate channels that can either be direct evaporation or subsequent evaporations.*

Parent cluster	Fragment ion	Evaporation channel	Parent cluster	Fragment ion	Evaporation channel
$Co_2O_2^+$	Co_2O^+	O	$CoCrO_2^+$	$CoCrO^+$	O
$Co_2O_3^+$	Co_2O^+, $Co_2O_2^+$	O_2, O	$CoCrO_3^+$	$CoCrO_2^+$	O
$Co_2O_4^+$	$Co_2O_2^+$	[O_2]	$CoCrO_4^+$	$CoCrO_2^+$	[O_2]
$Co_2O_5^+$	$Co_2O_3^+$	[O_2]	$CoCrO_5^+$	$CoCrO_3^+$	[O_2]
$Co_2O_6^+$	$Co_2O_2^+$	[O_4]	$CoCrO_6^+$	$CoCrO_4^+$	[O_2]
$Co_3O_2^+$	Co_3O^+/$Co_2O_2^+$	O/Co	$Co_2CrO_2^+$	Co_2Cr^+	[O_2]
$Co_3O_3^+$	Co_3O^+, $Co_3O_2^+$	O_2, O	$Co_2CrO_3^+$	Co_2CrO^+	[O_2]
$Co_3O_4^+$	$Co_3O_3^+$	O	$Co_2CrO_4^+$	$Co_2CrO_2^+$, Co_2Cr^+	[O_2], [O_4]
$Co_3O_5^+$	$Co_3O_3^+$	[O_2]	$Co_2CrO_5^+$	$Co_2CrO_3^+$	[O_2]
$Co_3O_6^+$	$Co_3O_4^+$	[O_2]	$Co_2CrO_6^+$	$Co_2CrO_4^+$	[O_2]
$Co_4O_3^+$	Co_4O^+	[O_2]	$Co_3CrO_3^+$	Co_3CrO^+	[O_2]
$Co_4O_4^+$	$Co_4O_3^+$	O	$Co_3CrO_4^+$	$Co_3CrO_2^+$	[O_2]
$Co_4O_5^+$	$Co_4O_3^+$, $Co_4O_4^+$	O_2, O	$Co_3CrO_5^+$	$Co_3CrO_3^+$	[O_2]
$Co_4O_6^+$	$Co_4O_4^+$	[O_2]	-	-	-
$Co_4O_7^+$	$Co_4O_5^+$, $Co_4O_3^+$	[O_2], [O_4]	$Co_3CrO_7^+$	$Co_3CrO_5^+$	[O_2]
$Co_4O_8^+$	$Co_4O_4^+$	[O_4]	$Co_3CrO_8^+$	$Co_3CrO_6^+$	[O_2]

In summary, the photodissociation spectra show that the substitution of a single Co by a Cr atom in $Co_nO_m^+$ has an influence on the preferred evaporation channel. Whereas all $Co_{n-1}CrO_m^+$ clusters (except $CoCrO_{2,3}^+$) prefer to decay by elimination of [O_2] units, several pure $Co_nO_m^+$ clusters evaporate atomic oxygen.

The present results for the pure $Co_nO_m^+$ can be compared with previous experimental dissociation studies. This comparison is summarized in Table 6.3. Collision-induced dissociation of oxygen-equivalent $Co_nO_n^+$ and oxygen-deficient $Co_nO_{n-1}^+$ ($n = 2$–5) clusters was studied by Freas and coworkers [23]. Johnson *et al.* reported the influence of stoichiometry and charge state on the structure of $Co_nO_m^{-,0,+}$ ($n = 1, 2$ and $m = 2 - 6$) [27]. Recently, photodissociation investigations of $Co_nO_m^+$ ($n = 4 - 9$, $m = 4 - 17$) clusters by Dibble *et al.* demonstrated the high stability of $Co_4O_4^+$ [40]. It was also suggested that $Co_nO_m^+$ dissociates preferentially via the loss of O_2 and that fragment ions with a 1:1 stoichiometry are favored [40]. Under the experimental conditions of these earlier studies, nevertheless, multiple fragment ions are found in most cases, causing ambiguity to identify sequential/parallel dissociation channels. In addition, it is also difficult to determine whether the losses of observed larger neutral fragments result from a single dissociation or multiple consecutive ones. Possibly, in these studies higher laser fluences were used or the clusters initially had a higher internal energy. In the present study, the preferred dissociation channels of $Co_nO_m^+$ and $Co_{n-1}CrO_m^+$ clusters can clearly be distinguished and there is no evidence for the occurrence of multiple subsequent evaporation events.

6.3.2 Relative stability information

As discussed in the literature, mass spectrometry alone does not always reflect relative stabilities of clusters [40-46]. The intensities of clusters, as produced in the source, is determined not only by relative stabilities but also by growth conditions (e.g., temperature of the cluster source, partial pressure of the inert gasses used for the condensation, etc.) and size-dependent ionization energies. In the present photofragmentation experiments, wherein clusters are first mass-selected and then exposed to laser light, the process tends to terminate at

Table 6.3: *Comparison of the* $Co_nO_m^+$ *dissociation channels observed in the present study with results available in literature. The most intense channel, if applicable, is listed in bold.*

Parent clusters	This work	Others
$Co_2O_2^+$	O	O, O_2, CoO, **CoO_2** [23]
		O, O_2 [27]
$Co_2O_4^+$	[O_2]	O_2, O_4 [27]
$Co_2O_6^+$	[O_2]	O_2, O_4, O_5, CoO_2, CoO_4 [27]
$Co_3O_2^+$	**O**, Co	Co, **CoO**, Co_2O_2 [23]
$Co_3O_3^+$	O, [**O_2**]	O, O_2, CoO, **CoO_2**, Co_2O_2, Co_2O_3 [23]
$Co_4O_3^+$	[O_2]	**Co**, CoO, Co_2O_2, Co_3O_3 [23]
$Co_4O_4^+$	O	**CoO**, CoO_2, Co_2O_2, Co_2O_3, Co_3O_4 [23]
		Co, CoO, CoO_2 [40]
$Co_4O_5^+$	O, **O_2**	O, **O_2**, CoO_2 [40]
$Co_4O_6^+$	[O_2]	**O_2**, CoO_2 [40]
$Co_4O_7^+$	[O_2]	O_2, O_3, O_4, **CoO_4** [40]

fragment ions with an enhanced stability. High internal energy of the clusters after photoabsorption allows the clusters to explore (on average) the most stable structural configuration. The data listed in Table 6.2 show that $Co_2O_2^+$, $Co_4O_3^+$, and $Co_4O_4^+$ are produced frequently as fragment of larger clusters, implying that they are relatively stable. Specifically, $Co_2O_2^+$ is a fragment of $Co_2O_3^+$, $Co_2O_4^+$, $Co_2O_6^+$, and $Co_3O_2^+$. $Co_4O_3^+$ is a daughter ion of $Co_4O_4^+$, $Co_4O_5^+$, and $Co_4O_7^+$, while dissociation of $Co_4O_5^+$, $Co_4O_6^+$, and $Co_4O_8^+$ terminates at $Co_4O_4^+$. The enhanced stability of $Co_4O_4^+$ was also observed in Ref. [40].

Qualitative stability information can also be obtained from the relative intensities of fragment to parent signals. Provided that the photoabsorption cross-sections do not strongly vary in the investigated size range, it is expected that the more stable clusters tend to remain more intense after fragmentation [41, 42]. The proposed enhanced stability of $Co_2O_2^+$, $Co_4O_3^+$, and $Co_4O_4^+$ is consistent with this argument. It should also be mentioned that a high fluence (> 50 mJ/cm^2) was needed to fragment $CoCrO_2^+$, which implies that this also is a relatively stable cluster size. Most of the other clusters could be fragmented at a fluence threshold of about 20 mJ/cm^2. Alternatively, $Co_2CrO_2^+$ and $Co_2CrO_3^+$ could easily be fragmented, implying that they might be relatively less stable than their pure counterparts, $Co_3O_2^+$ and $Co_3O_3^+$.

6.3.3 Structures of the $Co_nO_m^+$ and $Co_{n-1}CrO_m^+$ clusters

The preferred dissociation channels can provide hints about the structures of the clusters, e.g., whether oxygen prefers integrating into the metallic framework or being weakly absorbed on the surface [40, 46]. Possibly the atomic oxygen loss evaporation channel implies that $Co_nO_m^+$ with $m \leq n+1$ for $n = 2, 3$ and $m \leq n$ for $n = 4$ have structures in which oxygen atoms bridge the metal atoms. The [O_2] loss channel of the oxygen-rich species might imply that they have weakly absorbed O_2 units. The preferred loss of [O_2] for most Cr-doped species suggests that doping may modify the metal-oxygen framework. Since $CoCrO_3^+$ favors the loss of an O atom to form the stable $CoCrO_2^+$, one might postulate that the third O atom in $CoCrO_3^+$ is not bridging the Co and Cr atoms. Structural argumentation based on photodissociation experiments, however, has to be treated with care. The high photoexcitation energy may cause structural permutation before fragmentation. During this process the clusters explore all possibilities of getting the energetically most favorable dissociation channel. In this context, DFT computations provide additional information for structural determination.

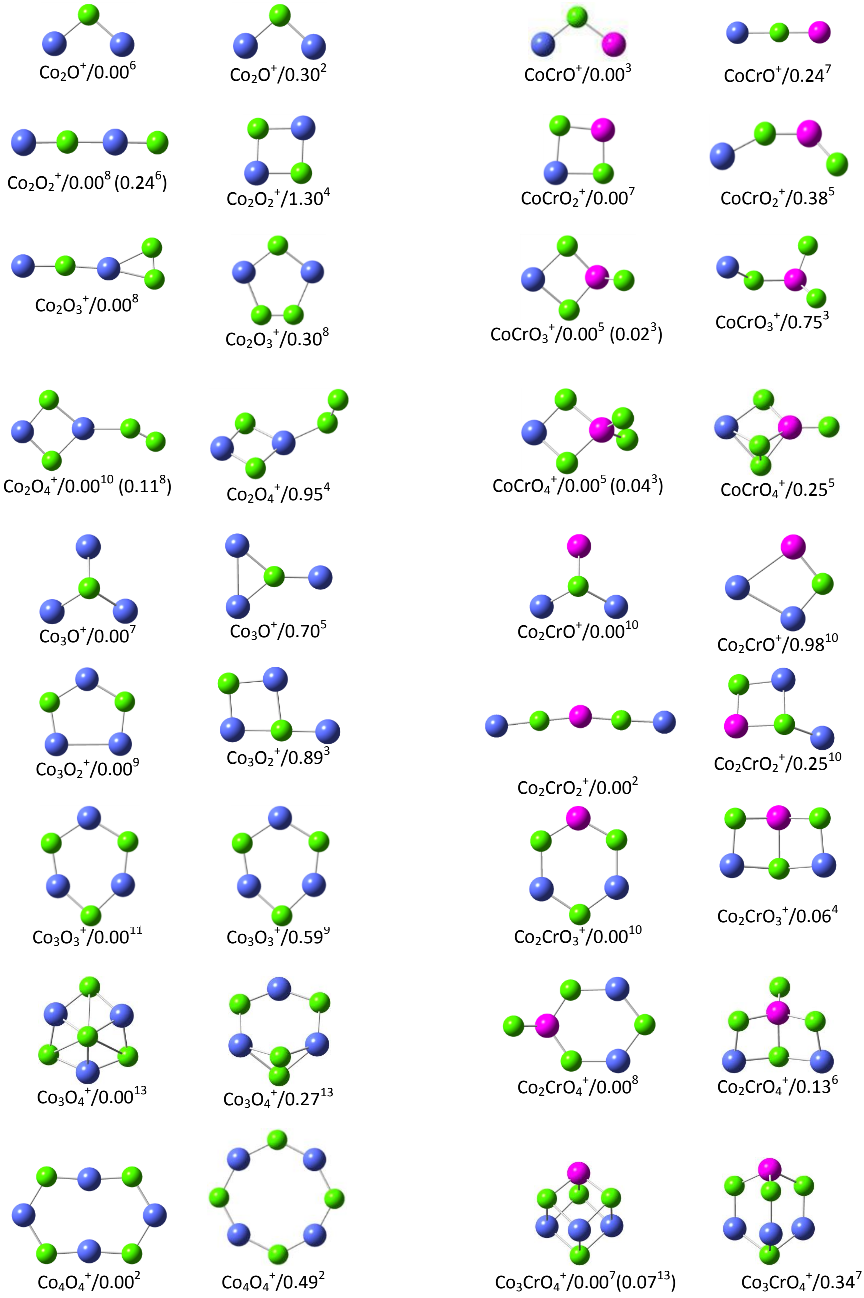

Figure 6.2: *Optimized structures, relative energies (in eV), and spin multiplicities (superscript) of computed lowest-energy isomers of* $Co_nO_m^+$ *and* $Co_{n-1}CrO_m^+$ *(m=1-4 for n=2,3 and m=4 for n=4).*

The optimized structures of energetically low-lying isomers of $Co_nO_m^+$ and $Co_{n-1}CrO_m^+$ ($m = 1 - 4$ for $n = 2, 3$ and $m = 4$ for $n = 4$) and relative energies with respect to the obtained ground states are shown in Fig. 6.2. In what follows, the terms triplet, quartet, quintet ... refer to the spin multiplicity $(2S + 1)$ of the clusters.

Co_2O^+ and $CoCrO^+$ have triangular equilibrium structures in which the O atom is located between the metal atoms with spin sextet and triplet states, respectively. For $Co_2O_2^+$, a linear Co-O-Co-O MES is found with an octet spin state. $CoCrO_2^+$ prefers a septet ring structure with O atoms bridging the metal atoms. Other low-energy isomers of $Co_2O_2^+$ and $CoCrO_2^+$ are linear and quasi-linear structures with relative energies of 0.24 and 0.38 eV, respectively. The ring $Co_2O_2^+$ is less stable with a relative energy of 1.30 eV. The linear MES obtained for $Co_2O_2^+$ is unexpected in comparison with previous predictions for $Co_2O_2^{0,+}$, where ring structures were found to be most stable [22, 27]. A linear Co-O-Co attached to two oxygen atoms, in octet spin state, is found for MES of $Co_2O_3^+$. The next isomer is a five-membered ring structure, which has an octet state and is 0.30 eV higher in energy than the MES. $CoCrO_3^+$ has a structure composed of a $CoCrO_2^+$ ring with an additional O atom attached to the Cr site and can exist in either a quintet (MES) or a triplet spin state (+0.02 eV). A second isomer is located 0.75 eV higher in energy and is in a triplet state. The most stable form of $Co_2O_4^+$ is a ring, in decet (MES) and octet (+0.11 eV) spin states, with an additional O_2 unit. The MES of $CoCrO_4^+$ also has a ring unit, but in this case the two oxygen atoms are bonded atomically to the Cr atom.

A high symmetric structure in which the oxygen atom is located at the center of a metallic triangle is the lowest-energy isomer of both Co_3O^+ and Co_2CrO^+. The next isomer of Co_3O^+ with a relative energy of 0.70 eV is formed by the MES of Co_2O^+ with an additional Co atom connected to the O atom. The next isomer of Co_2CrO^+ has a distorted rectangular structure (+0.98 eV). While $Co_3O_2^+$ prefers a five-membered planar ring structure in nonet spin states, a linear MES in doublet spin state is found for $Co_2CrO_2^+$. Low energy isomers, 0.89 eV and 0.25 eV less stable than the MES, are formed by attaching a Co atom to the rectangular rings of $Co_2O_2^+$ and $CoCrO_2^+$, respectively. $Co_3O_3^+$ and $Co_2CrO_3^+$ both have ring structures, where each O atom is bridging two metal atoms. The ring motive also is present in the geometries of $Co_3O_4^+$ and $Co_2CrO_4^+$, which are formed by $Co_3O_3^+$ a $Co_2CrO_3^+$ rings with an oxygen atom located on top and on the side, respectively.

Two degenerate planar eight-membered rings in doublet states are obtained for $Co_4O_4^+$. The incorporation of a chromium dopant atom induces a complete geometric restructuring. $Co_3CrO_4^+$ prefers 3D structures, in which the most stable form is a cube in either a septet (MES) or a 13-et spin state (+0.07 eV). The next isomer is 0.34 eV less stable.

In summary, $Co_nO_m^+$ with $m \leq n+1$ for $n = 2, 3$ and $n, m = 4$ have structures with oxygen-metal bonds and attached oxygen atoms in good agreement with the suggested structures based on the experimental dissociation pathways. The experimentally observed $[O_2]$ loss of $Co_2O_4^+$ is also supported by the predicted ring-based ground-state structure with weakly bonded O_2 unit. The structural difference between a linear-like $Co_2O_3^+$ and a ring structure with an absorbed O atom for $CoCrO_3^+$ is reflected in the preferred dissociation channels (evaporation of O_2 molecule and an O atom, respectively). Similarly, different experimentally observed dissociation behavior for pairs of pure $Co_nO_m^+$ clusters and Cr doped clusters, such as, $Co_3O_2^+$ and $Co_2CrO_2^+$, $Co_3O_4^+$ and $Co_2CrO_4^+$, and $Co_4O_4^+$ and $Co_3CrO_4^+$, can be linked to their different geometrical structures.

Table 6.4: *Calculated dissociation energies (in eV) to remove atomic oxygen, DE(O), molecular oxygen, DE(O_2), and a Co or Cr atom, DE(Co) and DE(Cr). The experimentally preferred dissociation channels are listed for comparison. Channels involving clusters with metal-metal bonds are marked with* †.

Parent clusters	DE(O)	DE(O_2)	DE(Co)	DE(Cr)	Preferred fragments
$Co_2O_2^+$	3.31	$2.95^\dagger$	4.29	–	O
$Co_2O_3^+$	3.49	1.27	4.72	–	O_2
$Co_2O_4^+$	3.32	1.28	4.74	–	$[O_2]$
$CoCrO_2^+$	4.88	$5.58^\dagger$	5.15	6.28	O
$CoCrO_3^+$	4.34	3.69	5.88	7.56	O
$CoCrO_4^+$	2.98	1.79	5.99	7.24	$[O_2]$
$Co_3O_2^+$	$4.73^\dagger$	$4.23^\dagger$	$3.93^\dagger$	–	O/Co
$Co_3O_3^+$	5.48	4.68	5.92	–	O_2
$Co_3O_4^+$	2.33	$2.28^\dagger$	4.93	–	O
$Co_2CrO_2^+$	$5.57^\dagger$	$6.38^\dagger$	3.04	5.03	$[O_2]$
$Co_2CrO_3^+$	5.40	5.44	4.10	6.95	$[O_2]$
$Co_2CrO_4^+$	4.37	4.24	5.49	7.99	$[O_2]$

6.3.4 Dissociation energies

The calculated dissociation energy required to remove atomic oxygen [DE(O)], molecular oxygen [DE(O_2)], a Co and a Cr atom, [DE(Co)] and [DE(Cr)], from the cobalt oxide clusters and their Cr-doped counterparts are listed in Table 6.4. The expected error margin of the current DFT functional on thermodynamic parameters is about ±0.3 eV. Dissociation channels involving species with metal-metal bonds are marked with †, which are likely less accurate given the current description of metal-metal bonds at the applied DFT level (cfr. the discussion on the benchmark data for dimers in section 6.2). It is expected from detailed balance theory that the evaporative rate constant $k_n(E)$ depends strongly on the dissociation energy [47, 48]. The preferred evaporation channel thus corresponds to the channel with the lowest dissociation energy.

The values in Table 6.4 indicate that the Cr doped species are relatively more stable than the pure cobalt oxide clusters. In particular, Cr doping significantly enhances the stability of $Co_3O_4^+$. At least 4.24 eV is needed to fragment $Co_2CrO_4^+$, while only 2.28 eV is needed for dissociation of $Co_3O_4^+$. This enhanced stability of $Co_{n-1}CrO_m^+$ compared to $Co_nO_m^+$ could be partially explained by the larger binding energy of CrO (4.36±0.3 eV) than that of CoO (3.98±0.14 eV) [34].

For $n = 2$ species, the calculations indicate that $Co_2O_3^+$, $Co_2O_4^+$, and $CoCrO_4^+$ prefer to dissociate by loss of an oxygen molecule. This implies that the experimental observations indeed correspond to the loss of O_2, rather than the consecutive evaporation of two O atoms. Also the experimentally observed atomic O evaporation from $CoCrO_2^+$ is confirmed by the calculations. For $Co_2O_2^+$ and $CoCrO_3^+$, the calculations indicate that evaporation of molecular oxygen is the most facile dissociation channel, while the experiments show atomic oxygen evaporation. The relative energy differences between DE(O) and DE(O_2) is for these clusters however comparable to the computational error margin.

For the $n = 3$ species, the calculations predict that $Co_3O_2^+$, $Co_2CrO_2^+$, and $Co_2CrO_3^+$ prefer dissociating via the loss of a Co atom, other species favor evaporation of either an oxygen atom or an oxygen molecule. The evaporation of a Co atom for $Co_3O_2^+$ is in line with the experimental observations, where the loss of a Co and an O atom are observed as parallel channels. Also the observed O_2 loss channels for $Co_3O_3^+$ and $Co_2CrO_4^+$ are confirmed by the calculations. The calculated energy difference between DE(O) and DE(O_2) for $Co_3O_4^+$ is much smaller than the error margin, which implies that the calculations support the experiments. However, discrepancies are found between the measured ([O_2] loss) and calculated (Co loss) most facile dissociation channels of $Co_2CrO_2^+$ and $Co_2CrO_3^+$. Such differences could be due to kinetic-controlled processes, where an activation energy is needed to initiate dissociation. The presence of a possible energy barrier has not been taken into account in the present calculations. It should also by remarked that a high daughter/parent intensity ratio is observed for $Co_2CrO_3^+$ (see Fig. 6.1), while this cluster is predicted to have a relatively high DE. This likely implies that the photoabsorption efficiency of this cluster is high at 355 nm.

Finally, there is an inherent shortcoming in the energetic treatment of metal-metal bonds using DFT methods. It will be more challenging to overcome, in particular for larger size species. In this context, the overall agreement between calculated dissociation energies and experimental observations in the present work is quite satisfactory.

6.4 Conclusions

We have investigated the stability of pure cobalt oxide and chromium doped cobalt oxide clusters $Co_nO_m^+$ and $Co_{n-1}CrO_m^+$ ($n = 2, 3$; $m = 2 - 6$ and $n = 4$; $m = 3 - 8$), by means of photodissociation experiments in combination with DFT calculations. Substitution of a Co by a Cr atom alters the dissociation behavior. Pure cobalt oxide clusters with a high oxygen content favor splitting off molecular oxygen if $m \geq n + 1$ for $n = 2, 3$ and $m \geq n$ for $n = 4$. Clusters with a lower oxygen content prefers to evaporate atomic oxygen. For chromium doped species, [O_2] unit evaporation is found to be the only lowest energy dissociation channel for all clusters, except $CoCrO_2^+$ and $CoCrO_3^+$.

Most clusters have structures in which the number of metal-oxygen bonds is maximized. The influence of the dopant atom seems to be strongest for $CoCrO_3^+$, $Co_2CrO_2^+$, $Co_2CrO_4^+$, and $Co_3CrO_4^+$, suggesting a different growth mechanism compared with the undoped cobalt oxide clusters. These structural changes generally are supported by corresponding changes in their dissociation behavior. The calculated most facile dissociation channels are in good agreement with the experimental observations. The calculated dissociation energies suggest an enhanced stability of the Cr doped clusters over their pure counterparts. Detailed comparison between experimental dissociation behavior and computational data show that $Co_2O_2^+$, $CoCrO_2^+$, $Co_4O_3^+$, and $Co_4O_4^+$ are particularly stable.

References

1. V. E. Henrich and P. A. Cox, *The Surface Science of Metal Oxides* (Cambridge University Press, Cambridge, 1994).
2. G. A. Samorjai, *Introduction to Surface Chemistry and Catalysis* (Wiley Interscience, New York, 1994).
3. P. A. Cox, *Transition Metal Oxides* (Clarendon, Oxford, 1992).
4. C. N. Rao and B. Raveau, *Transition Metal Oxides* (Wiley, New York, 1998).
5. W. Eerenstein, N. D. Mathur, and J. F. Scott, Nature **442**, 759 (2006).
6. G. R. Patzke, Y. Zhou, R. Kontic and F. Conrad, Angew. Chem., Int. Ed. **50**, 826 (2011).
7. J. A. Alonso, Chem. Rev. **100**, 637 (2000).
8. J. Garcia-Barriocanal, A. Rivera-Calzada, M. Varela, Z. Sefrioui, M. R. Diaz-Guillen, K. J. Moreno, J. A. Diaz-Guillen, E. Iborra, A. F. Fuentes, S. J. Pennycook, C. Leon and J. Santarnaria, ChemPhysChem **10**, 1003 (2009).
9. K. R. Asmis, Phys. Chem. Chem. Phys. **14**, 9270 (2012).
10. H. J. Zhai, X. Huang, T. Waters, X. B. Wang, R. A. J. O'Hair, A. G. Wedd, and L. S. Wang, J. Phys. Chem. A **109**, 10512 (2005).
11. E. Janssens, G. Santambrogio, M. Brummer, L. Woste, P. Lievens, J. Sauer, G. Meijer, and K. R. Asmis, Phys. Rev. Lett. **96**, 233401 (2006).
12. N. J. Mayhall, D. W. Rothgeb, E. Hossain, K. Raghavachari, and C. C. Jarrold, J. Chem. Phys. **130**, 124313 (2009).
13. J. E. Mann, D. W. Rothgeb, S. E. Waller and C. C. Jarrold, J. Phys. Chem. A **114**, 11312 (2010).
14. L. Jiang, T. Wende, P. Claes, S. Bhattacharyya, M. Sierka, G. Meijer, P. Lievens, J. Sauer, and K. R. Asmis, J. Phys. Chem. A **115**, 11187 (2011).
15. M. W. Kanan and D. G. Nocera, Science **321**, 1072 (2008).

16. D. A. Lutterman, Y. Surendranath, and D. G. Nocera, J. Am. Chem. Soc. **131**, 3838 (2009).

17. M. D. Symes, Y. Surendranath, D. A. Lutterman, and D. G. Nocera, J. Am. Chem. Soc. **133**, 5174 (2011).

18. C. J. Jia, M. Schwickardi, C. Weidenthaler, W. Schmidt, S. Korrhonen, B. M. Weckhuysen, and F. Schuth, J. Am. Chem. Soc. **133**, 11279 (2011).

19. V. Skumryev, S. Stoyanov, Y. Zhang, G. Hadjipanayls, D. Givord, and J. Nogues, Nature **423**, 850 (2003).

20. P. Poizot, S. Laruelle, S. Grugeon, L. Dupont, and J. M. Tarascon, Nature **407**, 496 (2000).

21. M. J. Benitez, O. Petracic, H. Tuysuz, F. Schuth, and H. Zabel, Eur. Phys. Lett. **88**, 27004 (2009).

22. S. Yin, W. Xue, X. L. Ding, W. G. Wang, S. G. He, and M. F. Ge, Int. J. Mass Spec. **281**, 72 (2009).

23. R. B. Freas, B. I. Dunlap, B. A. Waite, and J. E. Campana, J. Chem. Phys. **86**, 1276 (1987).

24. G. V. Chertihin, A. Citra, L. Andrews, and C. W. Bauschlicher, Jr., J. Phys. Chem. A **101**, 8793 (1997).

25. A. Pramann, K. Koyasu, A. Nakajima, and K. Kaya, J. Phys. Chem. A **106**, 4891 (2002).

26. F. Liu, F. X. Li, and P. B. Armentrout, J. Chem. Phys. **123**, 064304 (2005).

27. G. E. Johnson, J. U. Reveles, N. M. Reilly, E. C. Tyo, S. N. Khanna, and A. W. Castleman, Jr., J. Phys. Chem. A **112**, 11330 (2008).

28. Y. Yamasaki, S. Miyasaka, Y. Kaneko, J. P. He, T. Arima, and Y. Tokura, Phys. Rev. Lett. **96**, 207204 (2006).

29. Y. J. Choi, J. Okamoto, D. J. Huang, K. S. Chao, H. J. Lin, C. T. Chen, M. van Veenendaal, T. A. Kaplan, and S. W. Cheong, Phys. Rev. Lett. **102**, 067601 (2009).

30. A. D. Becke, J. Chem. Phys. **98**, 5648 (1993).

31. J. P. Perdew, Phys. Rev. B **33**, 8822 (1986).

32. M. J. Frisch *et al.*, *Gaussian 09, Revision B.01*, Gaussian, Inc., Wallingford CT, 2009.

33. E. Uzonova, G. St Nikolov, and H. Mikosch, J. Phys. Chem. A **106**, 4104 (2002).
34. Y. R. Luo, *Comprehensive Handbook of Chemical Bond Energies* (CRC Press: Boca Raton, FL, 2007).
35. D. A. Hales, C. X. Su, L. Lian, and P. B. Armentrout, J. Chem. Phys. **100**, 1049 (1994).
36. L. M. Russon, S. A. Heidecke, M. K. Birke, J. Conceicao, M. D. Morse, and P. B. Armentrout, J. Chem. Phys. **100**, 4747 (1994).
37. E. K. Parks, T. D. Klots, B. J. Winter, and S. J. Riley, J. Chem. Phys. **99**, 5831 (1993).
38. The negative DE values of Co_2 using B3LYP and B3PW91 with cc-pVTZ-pp imply that the reaction could be in exothermic. The dissociation is obviously prevented by a transition state. Otherwise, the dimer minimum cannot be located, and the atoms are repulsive giving the dissociated products.
39. F. Buendia and M. Beltran, Comput. Theoret. Chem. **1021**, 183 (2013).
40. C. J. Dibble, S. T. Akin, S. Ard, C. P. Fowler, and M. A. Duncan, J. Phys. Chem. A **116**, 5398 (2012).
41. S. Bhattacharyya, T. T. Nguyen, J. De Haeck, K. Hansen, P. Lievens, and E. Janssens, Phys. Rev. B **87**, 054103 (2013).
42. N. T. Tung, E. Janssens, S. Bhattacharyya, and P. Lievens, Eur. Phys. J. D **67**, 41 (2013).
43. J. B. Jaeger, T. D. Jaeger, and M. A. Duncan, J. Phys. Chem. A **110**, 9310 (2006).
44. K. S. Molek, Z. D. Reed, A. M. Ricks, and M. A. Duncan, J. Phys. Chem. A **111**, 8080 (2007).
45. K. S. Molek, T. D. Jaeger, and M. A. Duncan, J. Chem. Phys. **123**, 144313 (2005).
46. K. S. Molek, C. Anfuso-Cleary, and M. A. Duncan, J. Phys. Chem. A **112**, 9238 (2008).
47. L. Schweikhard, K. Hansen, A. Herlert, M. D. Herraiz Lablanca, and M. Vogel, Eur. Phys. J. D **36**, 179 (2005).
48. N. Veldeman, E. Janssens, K. Hansen, J. De Haeck, R. E. Silverans, and P. Lievens, Faraday Discuss. **138**, 147 (2007).

Chapter 7

Development of magnetic deflection experiment

Pursuing the understanding of the size- and constituent-dependent magnetism of bimetallic clusters needs an appropriate equipment. In this chapter, we present the design, implementation, and first results of a new magnetic deflection system coupled to a binary cluster source and a HRTOF/MS. Although this part is condensed into one chapter, the actual process has consumed a major part of the experimental work, including countless times of trials and errors.

Despite the fact that free cluster magnetism is studied mainly using the Stern-Gerlach magnetic deflection technique, only a few setups have been developed and used so far because of the technical complexity and highly sensitive operation. We start by giving an overview of existing setups, their main features and limitations. Then the basic criteria of the initial design of the Leuven magnetic deflection setup are defined. The subsequent discussion will focus on how to establish an inhomogeneous magnetic field with a uniform gradient using the two-wire field theory. Accurate 3D simulations are performed to obtain detailed information about the magnetic deflector. For the realization, a position sensitive detector and vacuum chambers were purchased. A vacuum compatible beam chopper was constructed. Beam collimators and the magnetic deflector are built in house by our technical workshop. Close attention had to be paid for aligning the whole system which is crucial for observing tiny beam deflections. Before being extracted, clusters travel about 1.8 m where they should be precisely guided through 0.3 mm×3.0 mm collimators and the magnet poles to reach the center of the ionization area. In the last section, the first results on the magnetic deflection setup are presented.

7.1 Design

7.1.1 Existing magnetic deflection setups

The magnetic deflection apparatuses developed by D. M. Cox and coworkers at Exxon Research and Engineering Company [1], W. A. de Heer and P. Milani at the Lausanne cluster group [2], and L. A. Bloomfield and coworkers at University of Virginia [3] are the setups on which the first measurements of magnetic properties of free clusters were performed. Later, molecular-beam magnetic deflection setups were constructed in the groups of J. A. Becker at the Rheinische Friedrich-Wilhelm-Universität Bonn [4], M. B. Knickelbein at Argonne National Laboratory [5], and R. Schäfer at TU Darmstadt [6]. W. A. de Heer also rebuilt an electric/magnetic deflection setup with significant improvements when he moved to Georgia Institute of Technology [7]. Most recently, another free cluster magnetic deflection setup was developed by A. Kirilyuk at Radboud University of Nijmegen. To our knowledge, currently only

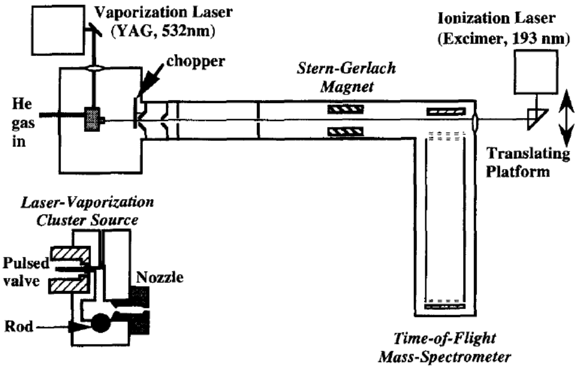

Figure 7.1: *Schematic overview of the Lausanne magnetic deflection apparatus (not to scale). The distance from the source to the mass spectrometer is about 2.4 m* [2].

the setups in Darmstadt, Georgia, and Nijmegen are still operational.

Although each setup has its own features, the general principles do resemble one another. Figure 7.1 shows schematically the Lausanne magnetic deflection setup [2]. Clusters are produced by vaporization of the metal target using a pulsed laser. The metal vapor is quenched in an inert carrier gas and condenses into clusters. The cluster source can be cooled to liquid-nitrogen temperature. After the mixture is ejected into the vacuum as a supersonic cluster beam, it is selected by a chopper for controlling dwell time and measuring cluster velocity. The cluster beam is collimated with 0.7 mm slits and deflected by means of an inhomogeneous 125 mm-long Stern-Gerlach field with a field gradient up to 270 T/m. The clusters enter the TOF/MS where they are photoionized with light from a pulsed UV laser source. The ionized clusters are accelerated perpendicularly to the molecular beam direction, then drift through a flight tube at the end of which they are detected with an ion detector.

Deflections of the clusters can be measured either by PSTOF/MS or by PIL across the beam (0.5 mm×10 mm). PSTOF detection is accomplished by appropriately adjusting the potentials [2]. With this method, the spatial distribution of the deflected and undeflected cluster beams can be recorded simultaneously with an accuracy of 0.2 mm over the entire detectable mass range. This is an important improvement over the traditional scanning methods, where either a slit in front of the mass spectrometer is swept across the beam or a narrow aperture of the excimer lasers is scanned across the beam in the

Table 7.1: *Overview of the main features of the selected existing magnetic deflection setups.*

Group	Lausanne	Virginia	Argonne	Georgia
Lowest source temperature	77 K	63 K	68 K	20 K
Magnet type	Rabi	Quadrupole	Quadrupole	Rabi
Chopper	yes	yes	no	yes
Collimator	yes	yes	yes	yes
Max field gradient	270 T/m	360 T/m	210 T/m	440 T/m
Typical cluster velocity	1500 m/s	-	-	300 m/s
Magnet length	125 mm	254 mm	305 mm	125 mm
Free drift length	1000 mm	1183 mm	900 mm	800 mm
Type of detection[†]	PIL, PSTOF/MS	PIL	PSTOF/MS	PSTOF/MS
Instrumental strength	71.7 Tm	202 Tm	132 Tm	95 Tm

[†] PIL and PSTOF/MS mean positioning ionization laser and position-sensitive TOF/MS, respectively.

extraction chamber. The transmission is then recorded as a function of the slit/excimer position.

Table 7.1 summarizes the main features (available in literature) of some of the magnetic deflection setups, which are selected based on their groundbreaking contributions to this field. It is clear from Eq. 1.10 that the deflection for a given mass is governed by various parameters such as: the field gradient dB/dz, the length of the magnet L, the length of the free-drift region D, and the cluster velocity v. The cluster velocity can range from 500 m/s to 1500 m/s, typically depending on source configurations, cluster sizes, and source temperature. Other parameters are instrumentally determined. The deflection strength of each setup, therefore, can be described by introducing an instrumental parameter K defined as $K = (L^2 + 2LD)dB/dz$. With a given cluster system, a larger K allows to detect clusters with a smaller magnetic moment/mass ratio. However, from

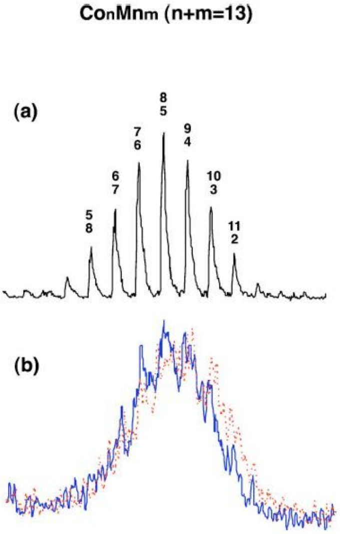

Figure 7.2: *TOF profiles for* Co_nMn_m $(n + m = 13)$ *recorded in the Argonne magnetic deflection setup. (a) High mass-resolution mode. Mass peaks are labeled according to* ${}^{n}_{m}$. *(b) Position sensitive mode (and then lower mass resolution). Solid trace, deflection field off. Dashed trace, deflection field on* $(B = 0.40$ *T,* $dB/dz = 82$ *T/m)* [8].

the earliest setups until the recent ones, the value of K has not been enhanced much since increasing K implies more difficulties in magnet fabrication, system alignment, and lower cluster production.

Not only the instrumental parameter but also the detection techniques are essential for deflection measurements. In the PSTOF/MS mode, the deflections of clusters are determined by quantitatively comparing the field on vs field off peak profiles. The spatial distribution of clusters is obtained indirectly in the time-domain at the cost of a reduced mass resolution. Figure 7.2 shows mass spectra of $\mathrm{Co}_n\mathrm{Mn}_m$ clusters recorded using the high mass-resolution mode and the position-sensitive mode for comparison [8]. With the mass spectrometer operated in high mass-resolution mode, the $\mathrm{Co}_n\mathrm{Mn}_m$ mass peaks are resolved, while operating in position-sensitive mode significantly reduces the mass resolution of the instrument. This mass-resolution reduction implies that PSTOF/MS is only possible to measure and analyze the deflection of a limited size range of clusters. This drawback can be overcome by employing the PIL method.

For PIL detection, a narrow ionization laser beam propagates antiparallel to the cluster beam and ionizes only those clusters that are deflected a specific distance from the undeflected beam center. Alternatively, a movable slit is positioned in the molecular beam path prior to the TOF ionization region. In both configurations, the mass spectrometer can be operated in high-resolution mode. By recording the resulting mass spectra at a range of positions relative to the beam center, one can obtain a complete deflection profile for each of the cluster sizes present in the beam. However, the use of PIL method has several limitations. Besides the requirement of precisely positioning the slit/ionization laser, it seriously increases the measuring time for a complete deflection profile, which in addition requires that the cluster production is stable over a long period.

7.1.2 The two-wire field theory

In this section, we discuss how to achieve a magnetic field that is inhomogeneous but has a constant gradient over the cross section where the clusters pass through. The initially used deflection field proposed by Stern and Gerlach has a disadvantage that the gradient strongly varies over the cross section of the atomic beam [9]. Already in 1933, a solution was suggested by I. I. Rabi: the two-wire field can produce an inhomogeneous magnetic field in combination with a uniform gradient [10]. The two-wire field is generated by two straight, parallel

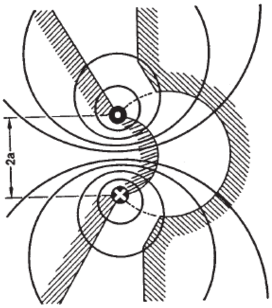

Figure 7.3: *Two-wire field. The dashed areas, of circular cylindrical form, indicate the pole pieces and the solid lines show the magnetic field of a two-wire system using currents in opposite directions. The distance from each wire to the center of the poles is a* [11].

wires carrying equal currents in opposite directions. However, the maximum achievable field strength and field gradient are limited by the maximum current that can be sent through the wires. Since superconducting magnets were not available at that time, the two-wire field was approximated by the use of a Rabi-type magnet. The pole faces of this magnet are cylindrical surfaces, resembling the equipotential surfaces of the two-wire system [11]. An alternative practical solution based on the two-wire field is a quadrant of a quadrupole field introduced by D. McColm in 1966 [12]. It consists of a hyperbolic pole face and a pole face built by the quadrant of a quadrupole. In the following, we discuss the theoretical background of inhomogeneous magnetic fields based on the two-wire field theory.

As discussed in section 1.3, assuming that the particles enter the magnetic field length L and that $\partial B/\partial z$ is constant, the particles follow a parabolic flight path and are deflected more or less strongly in the direction of the magnetic field according to their different velocities of entry. First of all, we will discuss how to establish an inhomogeneous magnetic field and the space in which $\partial B/\partial z$ is constant must be determined accurately.

The inhomogeneous field and uniform gradient are achieved by the two-wire system as shown in Fig. 7.3. The gradient can be calculated rather than measured. The system consists of two parallel wires, having currents in opposite

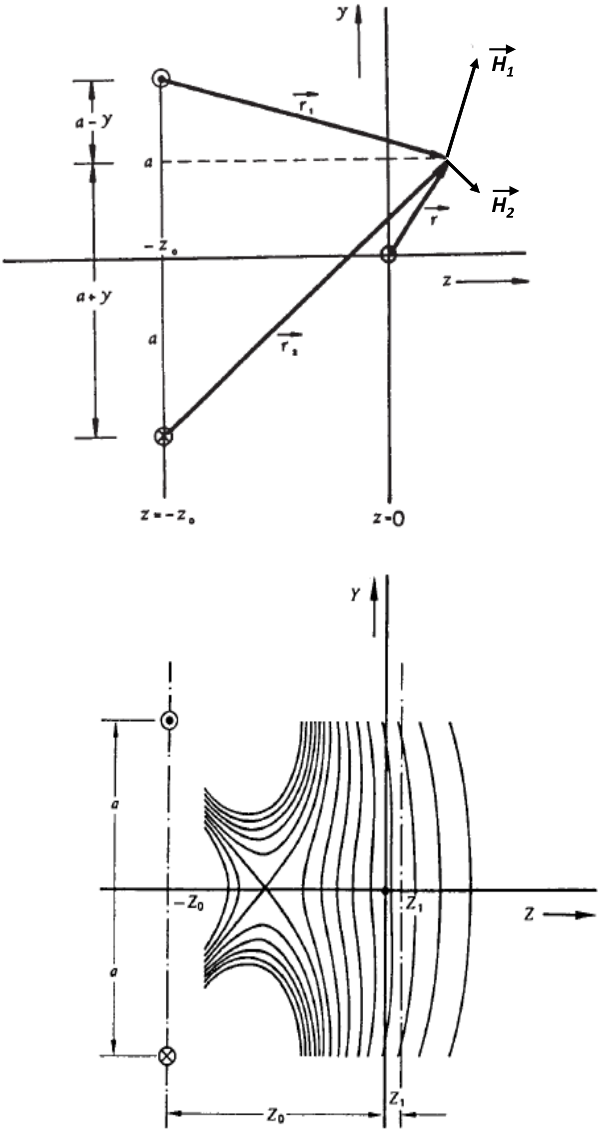

Figure 7.4: *(Top) Definition of the coordinates that are relevant for the two-wire system and (bottom) lines of equal magnetic field strength, demonstrating a constant field inhomogeneity along the* y *axis for* $z = z_1$ [11].

directions. The magnetic field $\overrightarrow{H}$, therefore, consists of two components, $\overrightarrow{H_1}$ and $\overrightarrow{H_2}$ as shown in Fig. 7.4:

$$\overrightarrow{H}(\overrightarrow{r}) = \overrightarrow{H_1}(\overrightarrow{r_1}) + \overrightarrow{H_2}(\overrightarrow{r_2}) \tag{7.1}$$

Each of the two conductors contributes to the field as follows:

$$\overrightarrow{H_i}(\overrightarrow{r_i}) = \frac{\overrightarrow{I_i} \times \overrightarrow{r_i}}{2\pi r_i^2}, (i = 1, 2) \tag{7.2}$$

where $\overrightarrow{I_1} = \overrightarrow{-I_2}$ is the current generating the magnetic fields. Hence, at the point $\overrightarrow{r}$

$$\overrightarrow{H}(\overrightarrow{r}) = \frac{\overrightarrow{I}}{2\pi} \times \left(\frac{\overrightarrow{r_1}}{r_1^2} - \frac{\overrightarrow{r_2}}{r_2^2} \right) \tag{7.3}$$

The value of the magnetic field strength is obtained by squaring this expression. Remembering in the subsequent calculation that $\overrightarrow{r_1}$ and $\overrightarrow{r_2}$ lie in a plane at right angles to $\overrightarrow{I}$, one finally obtains:

$$H = \frac{I}{\pi} \frac{a}{r_1 r_2} \tag{7.4}$$

with a is the distance from each wire to the plane $y = 0$. The gradient of H can be calculated, using

$$r_1^2 = (a - y)^2 + (z + z_0)^2 \tag{7.5}$$

and

$$r_2^2 = (a + y)^2 + (z + z_0)^2 \tag{7.6}$$

as

$$\frac{\partial H}{\partial z} = -\frac{Ia(z + z_0)}{\pi} \frac{(r_1^2 + r_2^2)}{r_1^3 r_2^3} \tag{7.7}$$

The surfaces of constant field inhomogeneity are shown in Fig. 7.4. To a good approximation, the equal-field-strength surfaces in the neighborhood of $z = z_1$ are regarded as planes. We must now find the plane $z = z_1$, in which the equipotential surfaces are as flat as possible, and how far this plane lies from the plane containing the wires, i.e. $z = z_0$. To do this, the length of the element path $(z_0 + z_1)$ will be determined, subjected to the condition that in the neighborhood of $y = 0$, $\partial H/\partial z$ is independent of y. Assuming that y^2 is small compared to $(z_0 + z_1)^2$ or a^2, the field gradients are found to be

$$\left| \frac{\partial H}{\partial z} \right|_{z_1} = \frac{2Ia(z_0 + z_1)}{\pi[(z_0 + z_1)^2 + a^2]^2} \tag{7.8}$$

The condition of a uniform $\partial H/\partial z$ along the y direction at $z = z_1$ turns out

$$\frac{\partial}{\partial y}\left(\partial H/\partial z\right) = 0 \tag{7.9}$$

We then get:

$$2a^2 - (z_0 + z_1)^2 = 0, \tag{7.10}$$

from which the distance from the plane containing the two wires to that of the uniform gradient is as

$$z_1 + z_0 = a\sqrt{2}. \tag{7.11}$$

Calculations show that the field inhomogeneity (or the gradient uniformity) starts to decrease with increasing y from $y \simeq 2a/3$.

In practice, only H can be measured, and not $\partial H/\partial z$. Hence it is useful to find a relation between the field and gradient in the plane $z = z_1$ which, to a good approximation, does not depend on y in the neighbourhood of $y = 0$. We have

$$\left|\frac{\partial H}{\partial z}\right|_{z_1} = \frac{2\sqrt{2}I}{9\pi a^2} \tag{7.12}$$

with $I = (3a^2\pi/a)H$ at $z = z_1$. It turns out that

$$\left|\frac{\frac{\partial H}{\partial z}}{H}\right|_{z_1} = \frac{2\sqrt{2}}{3a} \tag{7.13}$$

This ratio depends on the parameter a only, which is a constant. The field strength is thus related to the field gradient:

$$\frac{\partial H}{\partial z} = 0.9428\frac{H}{a}. \tag{7.14}$$

7.1.3 Rabi-type and quadrupole-like magnets: detailed simulations

Detailed simulations are carried out to further understand and evaluate the performance of the inhomogeneous magnetic field using Rabi-type and quadrupole-like magnets. The results presented in this section are mainly the work of Bert Masschaele and Herbert De Gersem (KU Leuven - KULAK) [13]. For the optimization of the magnet poles, the 2D simulation software FEMM was used [14]. In order to achieve the uniform gradient field, the pole shapes are optimized with FEMM, using the toolkit Octave-FEMM, an interface between

FEMM and Matlab or Octave. A Matlab program was written to sweep the pole shape parameters and to calculate the magnetic field density. After optimization of the poles in 2D, the 3D simulation software CST STUDIO SUITE was used to study the electromagnetic fields for the entire magnet, including the return yoke and the edge fields at the entrance and exit of the magnet [15].

Electromagnetic simulations

Figure 7.5 shows a drawing of the quadrupole-like and Rabi-type magnets with the definition of the geometrical variables of the poles. The quadrupole-like design is based on the quadrupole magnet of the Darmstadt setup [6]. Table 7.2 lists the parameters describing the geometry for two sets of the pole designs. Each set consists of two Rabi-type (or quadrupole-like) poles, which are designed to produce a weak and a stronger gradient field. The geometric parameters of the magnet poles are optimized to achieve the high field gradient and to maximize the gradient homogeneity. The homogeneous area of gradient fields is 3.0 mm by 0.3 mm. The latter dimension is in the deflection direction. Figure 7.6 presents the contour plots for the field magnitude and field gradient in the central pole gap of the weak Rabi magnet. Because of the symmetry of the magnet poles, only half the beam area in the lateral axis is shown. The black solid lines indicate the homogeneous area of gradient fields. A field magnitude of 0.91±0.03 T and a field gradient of 210±10 T/m are achieved at the current of 3000 A·turns. The inhomogeneity of the gradient is of the order of ±5% for the beam area of 3.0 mm by 0.3 mm [16].

Table 7.2: *Values for the parameters after optimization of the uniform gradient field (unit coordinates and distances in millimeter). The coordinates are defined with respect to the origin x-y in Fig. 7.5.*

	Quadrupole-like			Rabi-type	
Pole set	weak	strong	Pole set	weak	strong
r_pole	4.74	7.11	R_concave	3.333	5
alpha	35^o	40^o	Center concave	(-2;0)	(-3;0)
p1	(-2.86;2.72)	(-4.66;4;57)	p1	(-1.59;3.31)	(-2.38;4.96)
p2	(-4.96;20)	(-17.61;20)	p2	(-1.59;5.31)	(-2.38;6.96)
p3	(-1.5;3.5)	(-3.5;6.5)	p3	(17;20)	(17;20)
p4	(-1.5;5.5)	(-3.5;8.5)	R_convex	2.666	4
p5	(17;20)	(17;20)	Center convex	(-4;0)	(-6;0)
center	(-6.74;0)	(-10.11;0)	p4	(-17;20)	(-17;20)
w_pole	40	40	p5	(-4;2.666)	(-6;4)
length	200	200	length	200	200

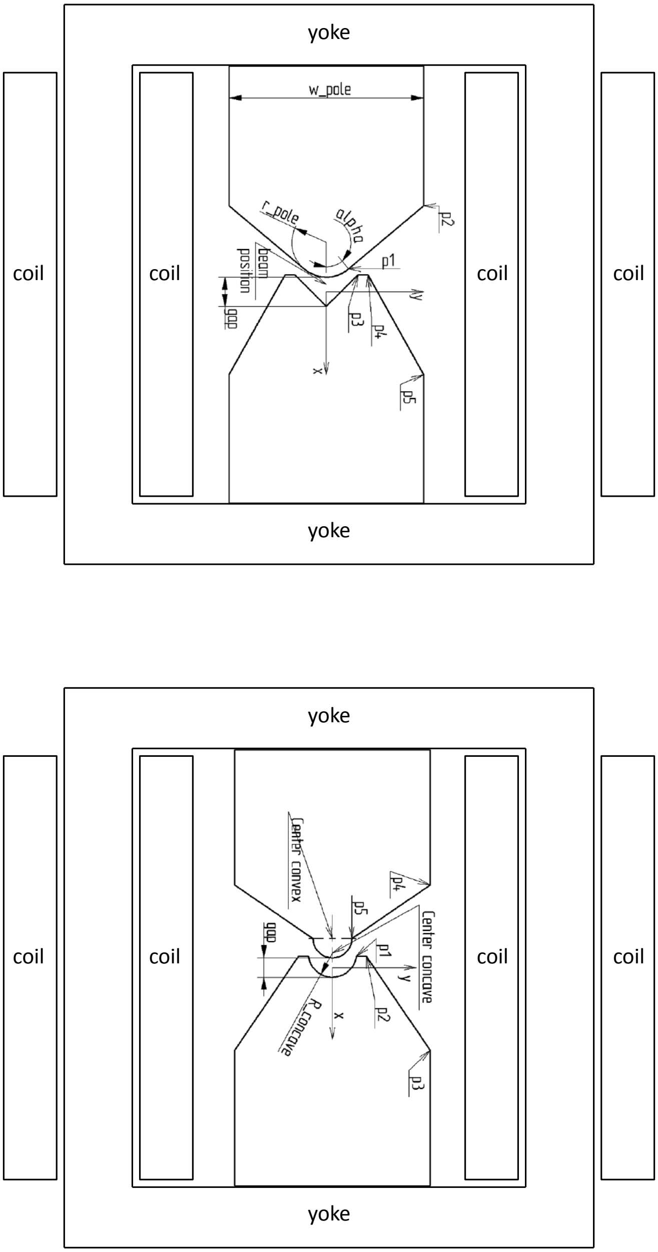

Figure 7.5: *(Top) Quadrupole-like and (bottom) Rabi-type magnets with geometric parameters of the poles.*

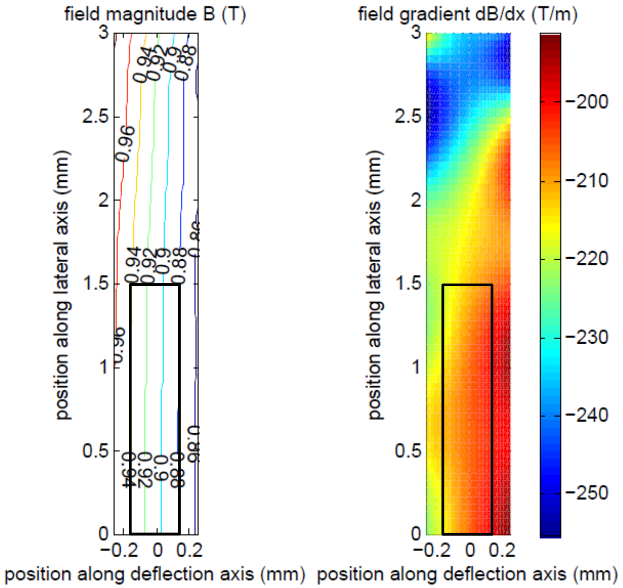

Figure 7.6: *(Left) The field magnitude and (right) field gradient of the weak Rabi magnet in the central pole gap for a current of 3000 A·turns. The black solid lines indicate the homogeneous area of gradient fields. Because of the symmetry of the magnet poles, only half the beam area in the lateral axis is shown.*

Figure 7.7 shows the result of the simulated field gradients in the homogeneous area as a function of the current in the coils for the two pairs of weak and strong magnets. It is seen that in the high current regime the Rabi-type magnets produce a lower field gradient than the quadrupole-like one for both sets of poles. Moreover, the saturation of the iron in the Rabi-type poles starts already at a lower current than the quadrupole-like poles. To reach a high field gradient (400 T/m), one will have to operate the magnet in saturated conditions.

From the simulations we find that the weak magnets saturate at around 2800 A·turns and the stronger ones at 2000 A·turns. In section 7.2.5, the I-B curve of realized magnets is will be discussed and compared to the simulations.

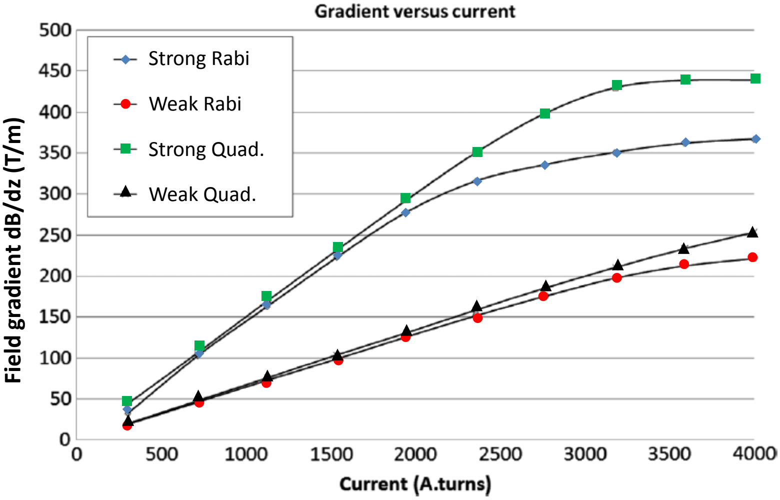

Figure 7.7: *The field gradient in the homogeneous area as a function of the current in the coils for the two studied magnet sets.*

Electrical properties and heating

A high current is required to reach the strong field gradient up to 400 T/m. The non-negligible resistance of the copper wires will generate heat in the coils. This deposited heat can be removed by adding water cooling to the coils. One technique which is often used in magnet designs, is to use the hollow water carrying cooling tubes as electrical windings. For our design, to reach 400 T/m, the coils have to carry a current of 3000 A·turns. The coils are connected in series.

Typically for free cluster experiments, the magnet can be operated in pulsed mode, for example, measuring alternatingly with and without magnetic field. This requires low inductance values. With the low frequency time domain solver of CST EM STUDIO, one can estimate the effects due to eddy currents in the iron for a rectangular pulse applied to the coils. The magnetic field at the center of the magnet was calculated for an operating frequency of 1 Hz. The simulation gives a value for the relaxation time due to the eddy currents up to 0.5 s to reach the full field state. This means that for a repetition rate of 10 Hz, the magnet would only achieve about 85% of the full field state, implying that the magnet cannot work in saturated conditions.

Table 7.3: *Calculated beam deflection d with respect to the parameter D for Ag atoms by the strong Rabi-type and strong quadrupole-like magnets at 3000 A·turns.*

D (m)	d (mm) Rabi-type	d (mm) Quadrupole-like
0.0	0.36	0.43
0.5	2.19	2.63
1.0	4.02	4.82

Mechanical deformations

It is known that a material could respond to a magnetic field by changing shape. After studying the electromagnetic properties of the magnet, a mechanical simulation of the magnet was made. This was done with T-FLEX, a software including Finite Element Analysis tools to study the thermal and mechanical properties [17]. With T-FLEX one can calculate the deformation of the magnet due to the magnetic force. From the mechanical simulation, it was concluded that for the proposed design the deformations are of the order of one micrometer. Since this deformation is much less than the precision of the machining, its influence on the behavior of the magnet can be neglected.

7.1.4 Deflection tracking

Further estimation of the particle deflection is carried out. We considered the beam deflections of silver atoms by the strong Rabi-type magnet and strong quadrupole-like magnet operating at 3000 A·turns with respect to the position of the detection screen. The silver atoms are assumed to have an initial speed $v = 1000$ m/s. The transverse speed is assumed to be eliminated by the collimators. The deflection d is calculated using Eq. 1.10 with $\mu_z = \pm 1/2\ \mu_B$ and $m_{Ag} \simeq 1.7767 \cdot 10^{-25}$ kg. The length L of the magnet is 0.2 m. As shown in Table 7.3, the deflection is small at the end of the magnets and increases linearly with D. For the given parameters, the quadrupole-like magnet has a higher gradient (420 T/m) than the Rabi-type magnet (350 T/m). Consequently, the beam will, for the given geometric designs, be deflected about 19% more in the quadrupole-like field than in the Rabi-type one.

Table 7.4: *Intrinsic beam width according to the distance between the skimmer and the farthest slit. Assuming that the detection screen is placed 1000 mm downstream the farthest slit, which has an aperture of 0.3 mm in the z direction.*

Skimmer-slit distance (mm)	Intrinsic beam width (mm)
300	±0.66
400	±0.50
500	±0.40
600	±0.33

Position-sensitive resolution

The possibility to differentiate two slightly different deflected peaks depends rather on the FWHM (peak width) than on the instrumental deflection strength. The peak width is determined by the size of the cluster beam in the z direction. Sizing the cluster beam is often done, in a compromise with the signal intensity, by using a collimation system. The collimation system consists of at least two slits to achieve a well collimated cluster beam. The second slit is needed for obtaining a parallel beam, eliminating the initial velocity of the clusters in the z direction before they are deflected by the magnetic field. Since the homogeneous area of the field gradient is small, i.e. 0.3 mm by 3.0 mm [cfr. simulations], the cross-section of the cluster beam has to be equal or smaller than that. For illustration, simulated beam deflections of Ag_{11} clusters, assuming they behave like classical particles with a fixed magnetic moment, are shown in Fig. 7.8 for beam widths of 1.0 and 0.5 mm. The beam profile is assumed to be Lorentzian. The deflection of Ag_{11} is 11 times smaller than that of silver atoms because of their larger mass. One can see that two deflected peaks almost overlap for FWHM = 1.0 mm while they are partially separated if FWHM = 0.5 mm. Obviously, high position-sensitive resolution is essential for detecting the deflection of heavy clusters and/or clusters having small magnetic moments.

A simple estimation of the intrinsic beam width according to the distance between the skimmer and the farthest slit is shown in Table 7.4. With a given slit-detection screen distance, increasing the skimmer-slit distance will decrease the beam deviation at the detection screen. However, increasing the skimmer-slit distance will result in a reduction of signal intensity and alignment difficulties. Therefore, positioning of the collimators must be considered in compromise with optimization of signal intensity as well as the complexity of system alignment.

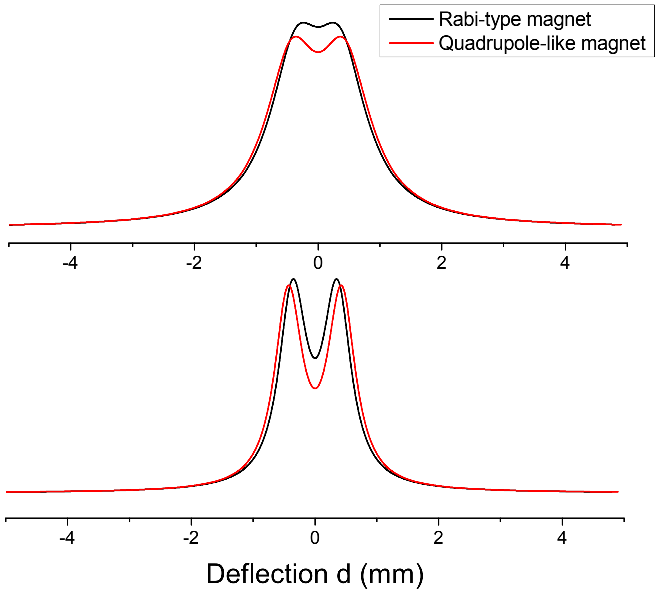

Figure 7.8: *Simulated beam deflection of* Ag_{11} *clusters, that would behave as classical particles with a fixed magnetic moment of 1* μ_B*, for FWHM = 1.0 mm (top) and 0.5 mm (bottom). The detection screen is placed 1.0 m from the magnet. The gradients are 350 T/m and 420 T/m for the Rabi-type and quadrupole-like magnet, respectively.*

Velocity selection

While the size of the cluster beam in the z direction defines the intrinsic position-sensitive resolution, the cluster velocity is crucial for the width of deflected peaks. Upon leaving the source the clusters travel with quite different velocities. For a certain cluster size, slow clusters will experience the magnetic field during a longer time, and consequently, have a greater deflection compared to that of the fast ones. As a consequence of Eq. 1.10, clusters with different velocities will be deflected differently, resulting in a broadening of deflected peaks. Therefore, not only the cluster velocity must be known precisely for extracting the $\langle \mu_z \rangle$ value, but also the velocity differences need to be minimized in order to obtain a high deflection resolution. As discussed in 7.1.1, the cluster velocity is

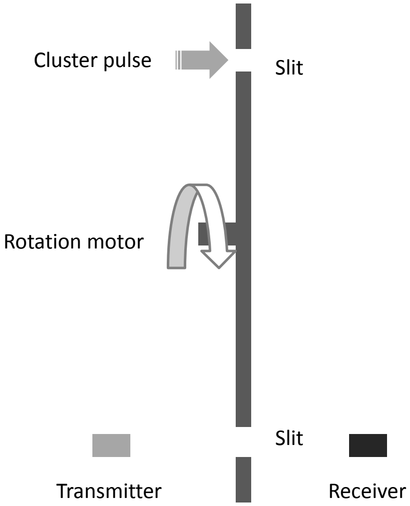

Figure 7.9: *A schematic drawing of the chopper with the photodiode transmitter and receiver.*

conventionally estimated by timing the ablation lasers and the extraction field [18]. Velocity selection is partly realized by controlling the overlap cross-section of the cluster beam and the excimer laser. However, since the resident time of the clusters inside the formation chamber is not known exactly, this gives a relative uncertainty on the velocity of about ±10% [19]. It also gives a spread since clusters with different velocities may arrive at extraction at the same time if they have left the source at different moments.

To overcome this problem, a chopper was used to select a thin slice of cluster pulses [20]. A schematic drawing of a simple chopper is shown in Fig. 7.9. It consists of a rotatable metallic blade with two small apertures coupled to a photodiode. In practice, the number and size of the apertures can be varied depending on the chopping frequency and the desired length and width of the cluster slices. In Fig. 7.9, two apertures are placed in the opposite position so that when the first aperture chops the cluster beam, the other is also opened allowing a signal from the photodiode transmitter to the receiver. Using the

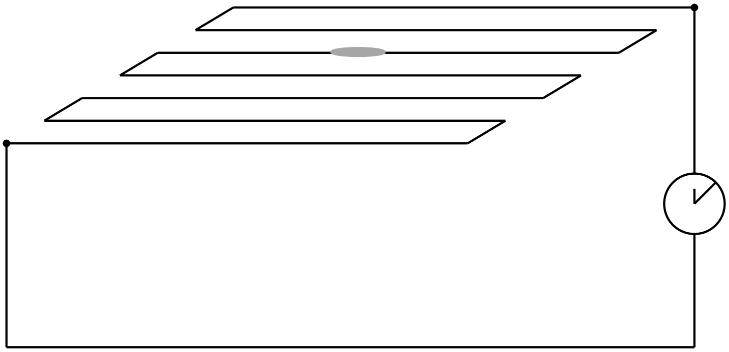

Figure 7.10: *Sketch of the delay-line method. The gray spot indicates the signal. The black dots indicate the ends of the line.*

feedback from the photodiode, one can synchronize the chopper with the laser ablation. Measuring the time interval from the chopper to the extraction gives a very accurate determination of the cluster velocity (an uncertainty of about 1.5% can be achieved [7]). Moreover, precisely timing the chopper allows to select thin cluster slices in which the cluster velocities are almost identical.

7.1.5 Two dimensional imaging of position and time-of-flight

One of the remaining challenges for the existing setups is simultaneously achieving high-resolution mass spectra and deflection profile of clusters as discussed in 7.1.1. For this purpose, we use a delay-line position-sensitive detection coupled to the TOF/MS. This method has proven to be an effective approach for charged particles in order to achieve position information by using an additional wire anode in conventional MCP read-out systems [21], delivering two (or three) dimensional imaging of position(s) and flight time, in particular, for collision experiments and electric deflection experiments [22,23].

The operating principle of the delay-line technique is presented in Fig. 7.10. The basic idea is to take advantage of the delay for a signal induced somewhere on this line to propagate in both directions towards the ends. A position determination can be performed by measuring the time difference between the arrival of the signal at both ends of the line. For two-dimensional position-sensitive imaging, the second delay-line has to be implemented with perpendicular orientation to the first one. Note that delay line detectors are single counting devices. The complete device works linearly with the number of incoming electrons. The detection principle limits the maximum detectable count rates at least due to the maximum delay of the meanders.

Effect of the extraction-reflectron alignment

When the delay-line position-sensitive detector is coupled to the TOF/MS, the influence of the extraction-reflectron alignment on the position-sensitive detection must be considered. Figure 7.11 presents the motion of two identical clusters having different initial kinetic energies in a simple TOF. If two clusters leave the extraction towards the reflectron, their velocities can be split into three components: one along the TOF axis, v_y, one along the initial beam axis, v_x, and one parallel to the deflection axis, v_z. Inside the reflectron, the electrostatic field of the reflectrons only affects v_y, resulting in a parabolic motion of the clusters. In the ideal case, the clusters always exit the reflectron at the same z position regardless their relative velocities if the extraction optics plane is parallel to the reflectron plane. This is because $v_z = 0$. If there is a small angle α between the extraction optics and the reflectron, v_z is not zero any more. The clusters still exit the reflectron at the same z position if the initial velocities of two clusters are equal (and their v_z are equal too).

Nevertheless, a real cluster beam enters the HRTOF with different velocities due to the spread in the position perpendicular to the extraction optics [24]. The initial velocities of the clusters can be expressed as

$$v = \sqrt{\frac{2E_p}{m}} \tag{7.15}$$

with E_p the potential energy in the extraction field, which is given by

$$E_p = \frac{q\Delta V_{extraction} s_0}{l_{extraction}} \tag{7.16}$$

where q is the electric charge of the clusters and $\Delta V_{extraction}$ is the electric potential difference in the extraction optics. s_0 describes the relative starting position in the extraction and $l_{extraction}$ is the length of the extraction field.

Clusters having a larger velocity will penetrate deeper and exit the reflectron in a higher z plane compared to the slower ones. Consequently, the initial beam

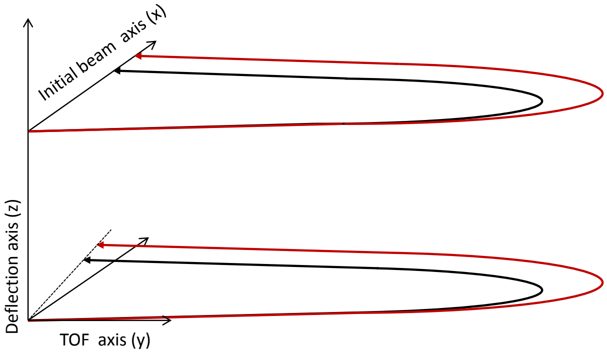

Figure 7.11: *Cluster motion in the simple TOF: (top) the extraction optics and the reflectron are parallel, and (bottom) the extraction optics is on an angle compared to the reflectron. The initial cluster beam and the TOF axis are in a plane perpendicular to the extraction.*

width will be expanded. This broadening δ depends directly on v_z and the time spent in the reflectron:

$$\delta = v_z t - v_z^{'} t^{'} \tag{7.17}$$

where v_z and $v_z^{'}$ are the velocities of the clusters with zero ($s_0 = l_{extraction}$) and non-zero ($s_0 < l_{extraction}$) starting position in the extraction. $t = v_y/a$ and $t^{'} = v_y^{'}/a$ are the corresponding times spent in the reflectron where they have an acceleration $a = q\Delta V_{reflectron}/ml_{reflectron}$. Then we get a beam broadening

$$\delta = (v^2 - v^{'2})\frac{sin\alpha\ cos\alpha}{a}. \tag{7.18}$$

A typical estimate for two clusters of the same mass with a difference of 6 mm in starting position, $\Delta V_{reflectron} = 7.5$ kV, $\Delta V_{extraction} = 8.6$ kV, and $\alpha = 1^o$ gives $\delta = 1.2$ mm. The velocity difference due to the spread in the cluster beam position along the extraction field is unavoidable. To eliminate this effect, close attention needs to be paid for the alignment to keep α close to zero.

Effect of the electrostatic field

Above we have discussed about the beam broadening caused by the imperfectness of the extraction-reflectron alignment. Another possible source which can widen the beam in the deflection direction is the inhomogeneous electrostatic field of the extraction/reflectrons. In particular, at the entrance of the electrostatic field there are inhomogeneities because of the presence of the extraction/reflectron grids. Near the surface of a grid, the perpendicular component of the electric field is non-zero, which might induce an acceleration in the z direction depending on the arrival position of ions. The maximum velocity deviation is [24]

$$\Delta v_z = Gg\frac{|q\Delta E|}{mv_y} \tag{7.19}$$

where g is the grid pitch, ΔE is the electric field difference, and $G = 0.144$ is a parameter obtained from literature [25]. To check how much the clusters are influenced by the grids, Δv_z can be multiplied by the flight time from the extraction/reflectron till the detector. A typical estimate of the maximum position deviation by the extraction grid for Pb atoms ($g = 0.112$ mm, $q\Delta E =$167 eV/mm, and $v_y = 40$ mm/μs) is about 1 mm at the first reflectron position.

Additionally, the field inhomogeneity can also result from mechanical inaccuracies during the construction and/or assembly of the reflectrons and HRTOF chamber. In addition, possible field distortions due to deposited material and charging effects cannot be excluded.

7.1.6 Initial design of the Leuven magnetic deflection setup

We have discussed the fundamentals of magnetic deflection measurements and possible issues which can limit the experimental accuracy. With this in mind, we now formulate the main criteria for the novel magnetic deflection setup in Leuven.

- Firstly, the design should be compatible to the Leuven cluster source. The use of the dual-target dual-laser vaporization source will be an advantage over the existing setups for studying magnetic properties of binary species.
- For simultaneously achieving high position-sensitivity and mass resolution, a novel solution is to couple a magnetic deflection system to the HRTOF mass spectrometer. The magnetic deflection system has to consist of a beam shaper, a magnetic deflector, a field-free deflection path, and a position-sensitive detector mounted on the HRTOF. The position-sensitive resolution is determined by the magnetic deflection system, while the mass resolution is defined by the HRTOF setup. This approach causes a small cluster beam broadening in the HRTOF as aforementioned so that the alignment and calibration must be done with great care.

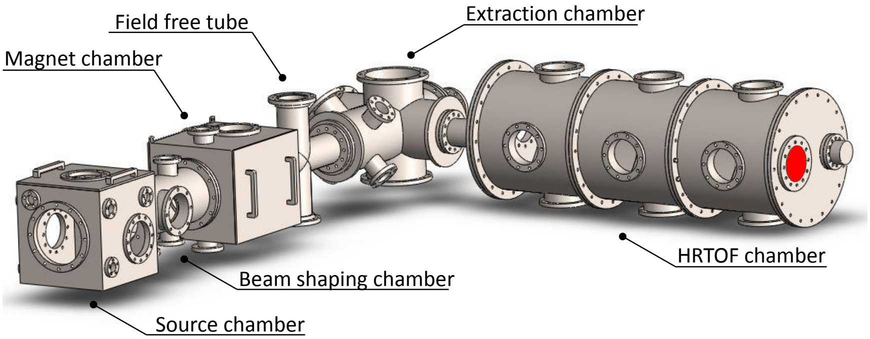

Figure 7.12: *Overview of the vacuum chambers of the magnetic deflection setup.*

- Finally, the setup must be designed in such an open way that the deflection strength (the instrumental parameter K, see section 7.1.1) can be improved subsequently for different cluster systems. For the first target of our measurements, K is estimated to be between 50 and 100 Tm.

7.2 Realization

In this section, we give a detailed technical description of the magnetic deflection setup in Leuven. This setup is an extension of the HRTOF mass spectrometer [24]. The extension includes new vacuum chambers, a beam chopper, beam collimators, and a magnetic deflector, which were built in-house with custom-made components. A position-sensitive detector was purchased. Hereafter we first give an overview of the setup and discuss the vacuum components and housing, followed by a detailed description.

7.2.1 Overview of the setup

Figure 7.12 shows a drawing of the magnetic deflection setup. The system can be divided into six functional parts: the source chamber, the beam shaping chamber, the magnet chamber, the field free tube, the extraction chamber, and the TOF chamber. The source chamber contains the dual-target dual-laser vaporization cluster source. The clusters are formed in the source block and the cluster beam expands into the beam shaping chamber via the skimmer. In the beam shaping chamber, the cluster pulses are chopped into thin slices and then collimated by the first collimator 20 cm downstream. The second collimator is placed in the magnet chamber, 20 cm away from the first one, and shapes the cluster beam again before it enters the magnetic field. The neutral species with magnetic moments are deflected by the inhomogeneous magnetic field and go into the field-free tube, which is separated from the magnet chamber by a 1.5 cm-diameter diaphragm. In the field-free tube, the deflection increases linearly until reaching the extraction chamber. The length of the field-free path is approximately 80 cm. In the extraction chamber, clusters are extracted from the beam by the electrostatic deflection. Hereto postionization (157-nm excimer laser) is needed since only charged clusters can be electrostatically accelerated. When the setup is operating in the magnetic deflection mode, the second reflectron is not used. The magnetic deflection is measured by the position-sensitive detector mounted at the position of the second reflectron. For the photofragmentation measurements, the second reflectron is turned on and the photofragmentation spectrum is recorded at the final position by a MCP detector.

7.2.2 Vacuum housing

Vacuum chambers

The source chamber, the extraction chamber, and the HRTOF chamber have been well documented in Ref. [24]. In short, the *source chamber* is a cubic box with a hinged lid for maximal accessibility. The hinged lid contains a DN-160 viewport to inspect the target holder position and motion during operation. The *extraction chamber* is based on a DN-200 six-cross. It also has a DN-200 viewport on the top to monitor the positioning of the extraction optics. A DN-63 MgF_2 window is mounted opposite to the free-drift tube for optimal transmission of 157 nm excimer laser light along the cluster beam axis. The extraction chamber is separated from the HRTOF chamber by a manual vacuum valve. The *HRTOF chamber* is composed of three 600 mm long cylindrical tubes. The chamber is closed at both sides by identical flanges. Each flange contains a small port that connects either to the extraction optics or the detector and a large port for mounting the reflectrons. To further maximize the flexibility of the HRTOF, each reflectron also has a DN-100 port in the center, which can be used for mounting a detector.

For the magnetic deflection measurements, the HRTOF setup is extended with the beam shaping chamber, the magnet chamber, and the field-free tube. These chambers were made of high quality 316L stainless steel and provided by

VACOM Vacuum Components and Metrology BVBA.

The *beam shaping chamber* is a cylindrical chamber based on a 430 mm-long DN-160 cylinder with six ports. A DN-160 port in the middle of the side of the tube holds a turbo pump. Two DN-40 ports are used for mounting the first collimator, while a DN-100 port at the bottom holds the chopper. Two DN-100 viewports on the side opposite to the pump are for viewing the position of the chopper and the first collimator.

The *magnet chamber* is a 395×368×410 mm^3 cube connected to the beam shaping chamber via a DN-160 port. The front and back side of the chamber can be entirely opened and closed by two square plates. Each plate is sealed with a rubber O-ring placed in a trapezoidal groove so that the O-ring stays on the plate when it is removed. Two DN-40 ports on top and bottom are used to mount the second collimator. A DN-160 viewport is placed on top of the chamber. On one of the side square plates, two DN-63 ports are added. These ports are used for water cooling and feedthrough of the current of the electromagnet. This plate also has a DN-160 port which is used for manual translations of the magnet without having to disconnect the water and electrical feedthroughs.

The *field-free chamber* is a four-way cross DN-100 tube (400×280 mm^2). It is connected to the DN-160 ports of the magnet chamber and the extraction chamber by two reducer flanges.

The whole setup is mounted on two identical support tables built of high-tensile aluminum profiles. One supports the HRTOF chamber and the other is for the rest of the setup. A 10 cm-long flexible bellow is used to connect the HRTOF and the extraction chamber. The level of the tables can be adjusted using feet screws. Each table has four wheels for transportation.

Vacuum pumps

The setup is vacated by five turbo pumps and two rotary pumps. The total vacuum volume can be divided into four parts. The first volume is the source chamber. The second volume consists of the beam shaping and the magnet chamber. The field-free tube and the extraction chamber form the third volume. Each of these three volumes is vacated by one turbomolecular pump (Leybold Turbovac 600C), but they share a high power water-cooled rotary pump (Alcatel

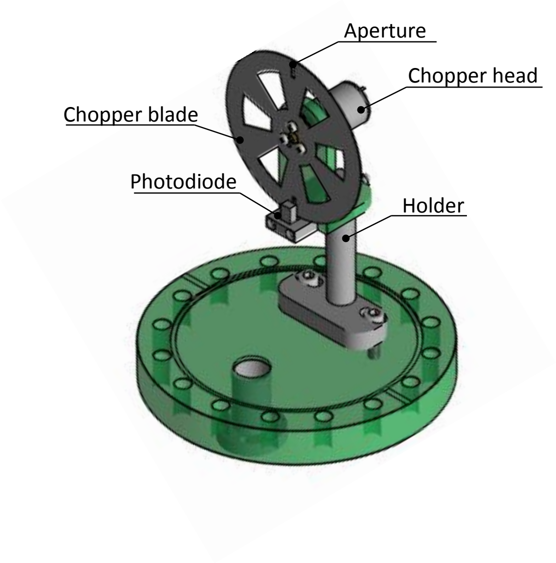

Figure 7.13: *Schematic drawing of the beam chopper.*

A100L). The fourth volume is the HRTOF chamber, which is pumped by two turbomolecular pumps (Leybold Turbovac 600C and Agilent V-551 Navigator) and another prepump (Edwards XDS 35i).

Four full-range pressure gauges (Leybold PenningVac PTR90) are installed at the source chamber, the magnet chamber, the extraction chamber, and the HRTOF chamber. Base pressures are 10^{-8} mbar for the entire setup. In practice, the setup can be pumped down to 10^{-6} mbar within 5 minutes, and the base pressure can be achieved after 8-10 hours due to microleaks and degassing processes. Venting with nitrogen or argon protects the magnet from water absorption and reduces the time to reach the base pressure.

7.2.3 Beam chopper

For the velocity selection and measurement, a vacuum-compatible chopper is implemented. Figure 7.13 illustrates the KU Leuven home-built chopper. The chopper system consists of a photodiode, a chopper head, a chopper blade, and a control unit. The chopper blade is made of copper. The chopper head and photodiode are fixed by a holder, which is mounted on a DN-100 flange. The length of the holder is adjustable (range ±5 cm). The chopper head is a

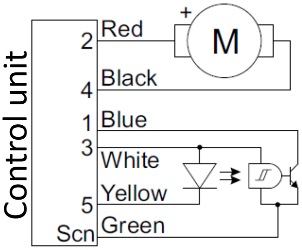

Figure 7.14: *Simplified electronic diagram of the chopper. The colors refer to the colors of the wires in the socket* [26].

cylindrical DC ironless brush motor (Portescap 22V28) using sleeve bearings with a maximal velocity of 7600 rpm (without load). The motor commutation system is made of precious metal for vacuum compatibility. The absence of an iron core is an advantage, resulting in a low rotor inertia and no cogging. The motor speed, therefore, depends rather on the supply voltage and the load torque than on the limitation of iron losses. The photodiode (OPTEK OPB970N11) is a photologic integrated circuit switch, which includes a photo-transmitter and -sensor, providing TTL electrical outputs.

The control unit (Scitec Instruments 300CD) connects to the motor and the photodiode via an electrical feedthrough with six connections as shown in Fig. 7.14. Power to the control unit, the motor, and the photodiode is controlled by an ON/OFF switch located on the control unit and indicated by a red LED indicator above the switch. The motor is fed by a 12 V source (red and black) while the photo-transmitter and -receiver are powered by a 5 V socket (white and yellow). When the photodiode sends a signal to open the logic switch, a 5 V reference signal will be sent to the control unit for frequency measurement (blue and green). A 5-digit screen on the control unit shows the measured chopping frequency with a resolution of 0.01 Hz. A test pattern “88888” is initially displayed when the control unit is switched on and then changes to “0.00” indicating that it is ready for operation. A BNC socket on the front panel provides reference signals, synchronized with the chopping frequency.

The home-made blade is a 0.5 mm thick disk with a diameter of 90 mm. The disk contains 6 openings that are created to reduce the mass of the disk. Two small rectangular apertures (2 mm×8 mm) close to the outer border, through which clusters can pass, are placed opposite to each other (half a circle apart). The distance from the blade to the skimmer is about 160 mm. The calculated and measured opening times of the aperture are given in Table 7.5. The opening time is measured by the photodiode. As the chopping aperture passes in front of the photodiode, the light flux falling on the detector is proportional to the exposed area of the photo-sensor. The measured opening time is the FWHM of the recorded signal.

Table 7.5: *Calculated and measured opening time of the chopping aperture.*

Chopping frequency (Hz)	Chopping period (ms)	Calculated open time (ms)	Measured opening time (ms)
10.00	100	1.60	1.594
20.00	50	0.80	0.792
50.00	20	0.32	0.364
100.00	10	0.16	0.184
200.00	5	0.08	0.084

The chopper can be operated either in the internal or external mode selected by an INT/EXT switch on the control unit. In the *external mode*, a voltage is applied to the chopper via the input socket mounted in the front panel. The chopping frequency increases linearly with the externally applied voltage. The maximally applied voltage is 12 V with a corresponding input impedance of 20 kΩ. For the *internal mode*, the chopping frequency is governed via an internal voltage by turning the control dial. In both cases, the indicated operating frequency in the digital screen is real-time measured by counting transmitted signals as recorded by the photodiode. The frequency can be measured over either a 1-second or a 10-second period by a switch located on the front panel of the control unit.

7.2.4 Beam collimators

The cluster beam is shaped by two identical home-made collimators, installed 450 mm and 650 mm downstream the skimmer. The first collimator is mounted on the beam shaping chamber, while the second one is placed in the magnet chamber. The collimator is a stainless steel box with a rectangular aperture in the center as shown in Fig. 7.15. The aperture's width is fixed at 3 mm, while the height is defined by two movable stainless steel knives. The knives are

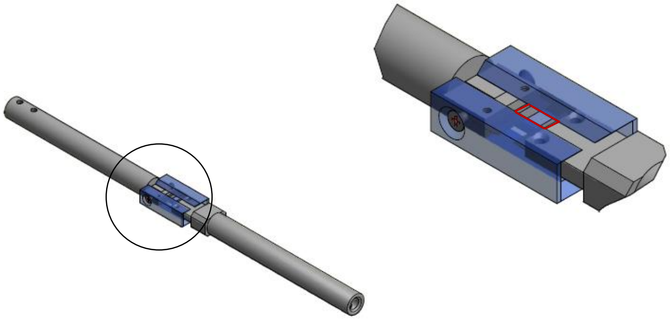

Figure 7.15: *The beam collimator and a zoom. The rectangular aperture is indicated by red lines.*

independently positioned by two linear feedthroughs (MDC, BLM 275-1) with a translation precision of 0.025 mm. This mechanism allows a fine control of both the width and the position of the aperture. The knives are connected to the feedthroughs via screw-gutter systems. Horizontal translation is provided by sliding the collimators along the gutter manually.

7.2.5 Magnetic deflector

Overview

Figure 7.16 presents the actual photo of the home-built magnetic deflector. The design is based on the simulations described in section 7.1.3 and was discussed in internal reports [16,27,28]. The magnetic deflector consists of a pair of magnet poles, the current carrying coils, the yokes, and the top/bottom plates. Dimensions of the magnetic deflector are given in Table 7.6. The yokes and the poles are connected to the plates by screws. The poles are designed to be replaceable with minor effect on the alignment of the magnet. The yokes, the poles, and the plates are made of ARMCO 99.85% pure iron (AK Steel International) which has a saturation field of 2.15 T. The relative permeability is 516 at H = 25A/cm; 146 at H = 100 A/cm; 54 at H = 300 A/cm. The coercive field is 110 A/m. The mass of the poles is about 4.7 kg. The entire magnetic deflector has a mass of 26.4 kg.

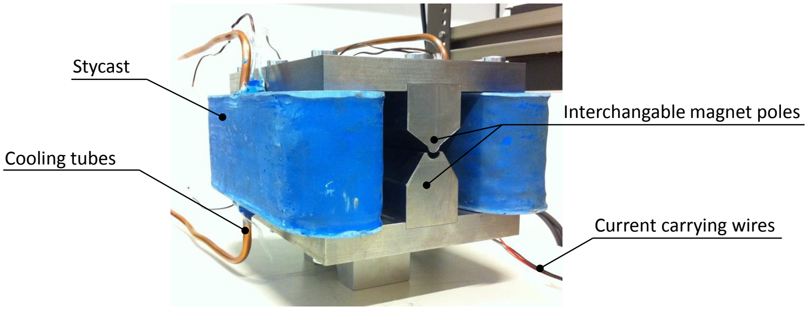

Figure 7.16: *The magnetic deflector.*

The schematic overview of the coils is presented in Fig. 7.17. From the inner to the outer side, one has the yoke, the current carrying copper wires, and the hollow copper tubes that carry the coolant water. The copper wires have a rectangular cross-section (2.24 mm×1.25 mm). The coils consist of 8 layers of wires and 33 turns per layer (or 264 windings). The cooling tubes have an outer diameter of 6.1 mm and a wall thickness of 1.5 mm. There are 9 windings of cooling tube around the coils. Wires and tubes are electrically isolated by Stycast insulation with a thermal conductivity of 1 W/mK. The thickness of the insulation between successive wire layers is about 0.4 mm and a bit more between wires and tubes.

Two sets of the magnet poles have been made according to the simulated designs presented in section 7.1.3. Both are of Rabi type but they differ in the field strength. Detailed dimensions of the pole sets, named strong Rabi and weak Rabi, are given in Table 7.2. At a current of 3000 A.turns, the strong Rabi is expected to produce a gradient of 345 T/m, while the weak Rabi gives a

Table 7.6: *Dimensions (mm) of the magnetic deflector.*

Component	Height	Width	Length
Yoke	80	20	200
Plates	20	150	200
Coils	80	62	240
Poles	47	40	200

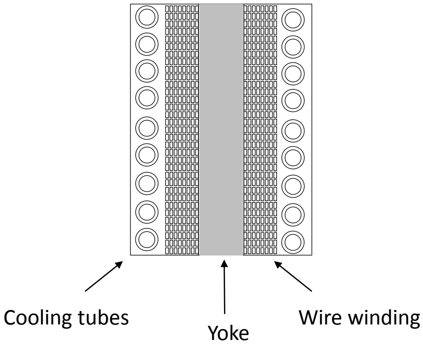

Figure 7.17: *Schematic cross-section view of the current carrying coils composed of a yoke, Cu wire windings, and cooling tubes.*

field gradient of 180 T/m. The dimension and position of the homogeneous gradient area is predetermined from simulations and reexamined by calibrating the magnet alignment. Other pole sets of the quadrupole-like geometry, which are designed to have a gradient of 435 T/m, will be made in the future.

Measured magnetic field

The magnet is operated by a power supply (TTi, CPX400SP) providing a current up to 11.5 A (corresponding to 3036 A·turns). Figure 7.18 shows the magnetic field between the magnet poles measured by a Tesla meter as a function of the applied current in the range of 0-10 A. Note that the field strength depends on the vertical position of the probe. Unfortunately, the measurement probe cannot be positioned very accurately because the size of probing tips is comparable to the gap size. Thus, the measured magnetic field is rather an average than a single-point value. Accurate values of the field and the gradient in the deflection area will only be known by calibrating the deflection measurement (as to be discussed in 7.3). However, the saturation behavior of the measured magnetic fields is in good agreement with the simulations (cfr. Figure 7.7). A nice linear current dependency for the weak Rabi is observed for currents up to 10 A (corresponding to 2640 A·turns). The strong Rabi starts to saturate for current values above 8 A (corresponding to 2112 A·turns). The measured remanence upon reducing the current back to zero is small (about 10 mT) [29].

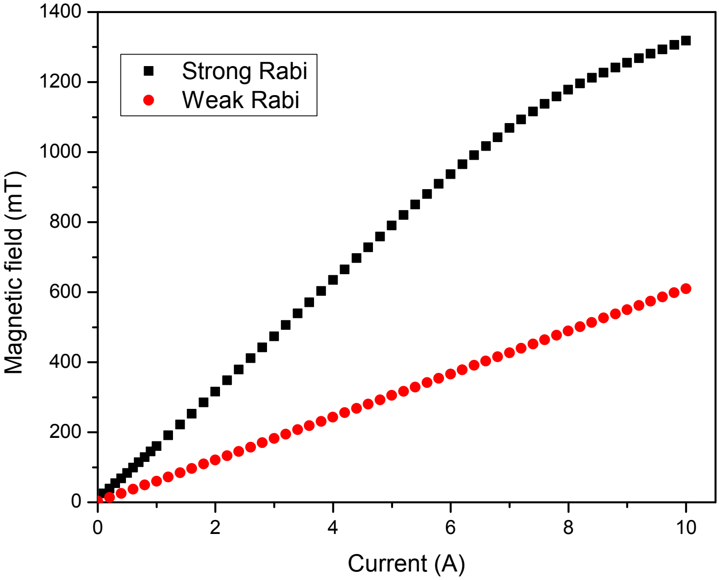

Figure 7.18: *Magnetic field measured between the magnet poles for the weak Rabi and strong Rabi poles as a function of the current through the coils.*

Cooling efficiency

The cooling efficiency has been evaluated with a constant current of 10 A. The water pressure is kept in the range of 3-4 bar. When the magnet is operated, the temperature of the magnet starts to increase from room temperature (about 21 ^{o}C) and gets saturated at around 26-27 ^{o}C after 60 minutes with water cooling on. The temperature of the cooling water is stablized at 17-18 ^{o}C. If the water cooling is off, the magnet temperature rises rapidly. The temperature measured at the iron top plate is 39 ^{o}C after 30 minutes without cooling.

7.2.6 Postionization

For postionization of neutral clusters, an excimer laser (Coherent Excistar^{TM} XS200) is employed. Excimer means “excited dimer”, which typically refers to a diatomic molecule of an inert gas atom and a halide atom. In the excimer laser, these gaseous dimers (ArF or F_2) are excited by collisions in a high density gas tube. The de-excitation of excited diatomic molecules releases the excitation energy via VUV photons. Since the ground state of the excimer molecules is intrinsically unstable, it is easy to obtain the population inversion between the ground state and the excited state.

The Excistar^{TM} XS200 can be used at two configurations corresponding to ArF and F_2 gas, providing laser light of 193 nm (6.4 eV) and 157 nm (7.9 eV), respectively. The laser output is sent along the cluster beam axis via a DN40 UV grade window mounted on the extraction chamber. For 157 nm laser light, N_2 purge gas needs to be used to reduce the light absorption in the air. The maximum energy is 200 mJ per pulse for 193 nm and 1.8 mJ per pulse for 157 nm laser light. The original beam profile is 3 mm by 7 mm. A 20 mm-diameter MgF_2 cylindrical plano-concave lens with a focal length of -100 mm is used to achieve a beam area of 3 mm by 30 mm (the later dimension is in the direction of the magnetic deflection) at the center of the extraction optics. For both configurations, the laser runs at a repetition frequency of 10 Hz, controlled by the Stanford delay generator.

7.2.7 Position sensitive detection

Overview

The simultaneous recording of position and arrival time is realized by a delay-line MCP detection system (Surface Concept 1D-DLD43). It consists of a delay-line detector unit, a pulse processing unit, a time-to-digital converter unit, and a high-voltage supply. The detector unit is mounted on a DN100 flange with feedthroughs for high-voltage supply and signal transfer. The pulse processing unit is directly connected to the detector unit via BNC sockets. The signal is amplified, sharpened, and discriminated to turn the analogue pulses from the detector into digital pulses used for the time-to-digital converter. This unit also has time reference input channels for the synchronization by an external time reference signal. The external signal can be either a low-voltage TTL signal or an analogue pulse. Output from the pulse processing unit is sent to the time-to-digital converter via a HDMI interface, which serves as a stop-watch for arrival time measurements. The measurement results, in terms of time differences and sums, are transferred to the PC via a USB 2.0 interface. Further data processing and presentation on the PC are realized by an end-user software.

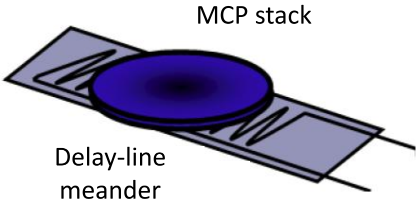

Figure 7.19: *Schematic drawing of the delay-line detector head* [30].

Delay-line MCP detector

Figure 7.19 shows a schematic drawing of the basic assembly of the DLD detector. The detector head is composed of a standard Chervon MCP array for pulse amplification and a one-dimensional delay line structure. The MCP anode is positioned behind the MCP stack, which typically amplifies incoming electrons by 10^7 times. The amplified electron cloud hits the DLD meander where it induces electrical pulses by capacitive coupling in the delay line. The pulses are traveling to both ends of the meander within a time determined by the hitting position. The arrival time at both ends of the meander relative to an external repetitive clock generates the time coordinate. The maximum count rate in the twofold coincidence measurement is 2.8×10^6 counts per second. The maximum dark count rate (without ion source) is 2 counts per second. The active width in the detection direction is 43 mm with 1024 channels, corresponding to a resolution of 0.04 mm. The non-resolving detection width is 30 mm, limited by the dimension of the meander delay line detector.

The operation voltage is determined by monitoring the detection efficiency when increasing the voltage to compensate the gain degradation. Figure 7.20 presents the so-called measured MCP curve, plotting the detected count rate as a function of the operation voltage. The MCP curve starts increasing from 1700 V and rises linearly up to 1900 V. At 1900 V, the MCP curve starts to show saturation. The slope change at 1900 V indicates the start of the working area. In our experiments, the operation voltage is a bit higher, around 1950 V.

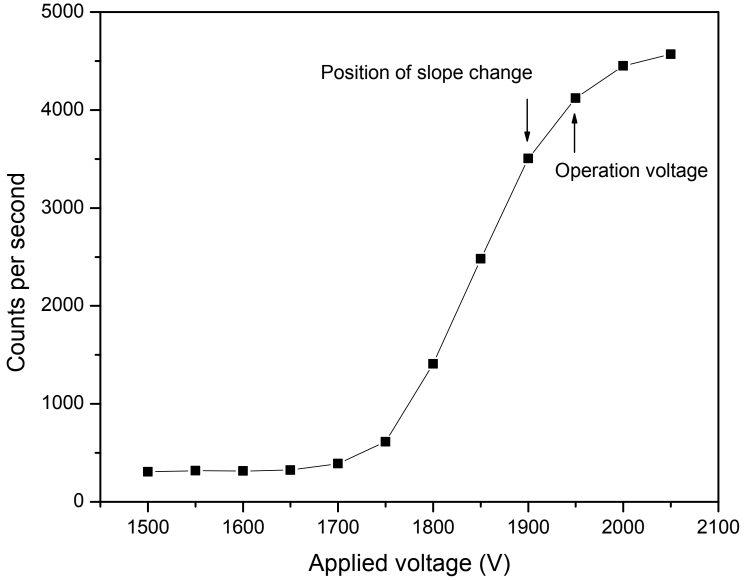

Figure 7.20: *Typical MCP curve of the 1D-DLD43 detector showing the dependence of the count rate on the applied voltage over the microchannel plates.*

Time-resolved position-sensitive detection

For magnetic deflection measurements, time-resolved position-sensitive detection is performed. In this mode, the delay line detector measures all events in temporal reference to an external clock. The operating scheme of this mode is schematically illustrated in Fig. 7.21. When a time reference signal in the form of a low-voltage TTL pulse is sent to the time reference input channel of the signal-processing unit, the detector starts recording. This reference is usually defined by the moment clusters are accelerated in the extraction optics. The time of flight is calculated by using the arrival times of pulses at the ends of the DLD meander. The results correspond to t[time-of-flight] = t[offset] + t[hit] - t[reference], where t[hit] - t[reference] is the time-of-flight in a given experiment. The device immanent constant, t[offset], is known from cable lengths, electronics propagation times, etc. The arrival times of pulses per event at the ends of the

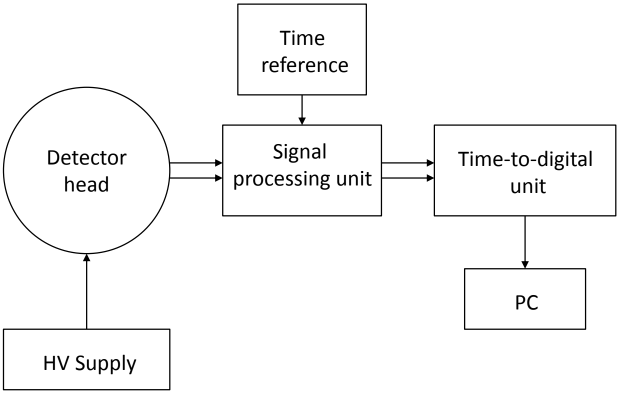

Figure 7.21: *Connection scheme of the 1D-DLD43 detector system.*

DLD meander are subtracted in order to extract a position in x. The position and time of each event are determined within a time window up to 29 ms. The software allows either to group all measured events in a full-time histogram or to select one or multiple narrow time regions of interest.

7.2.8 Setup alignment

Since the clusters travel over a long flying path (7.5 m in total) with a small cross-section of 0.3 mm by 3 mm, the setup needs to be aligned systematically and very carefully. The alignment procedure is as follows. We first establish a beam axis based on two points: the gas valve and the center of the ionization window, using theodolite measurements. The distance from the gas valve to the center of the ionization window is 2.1 m. The nozzle and the skimmer are then aligned with the above axis. Next, the 0.3 mm gap of the collimator mounted on the magnet chamber is aligned on the beam axis. The other collimator is aligned based on the signal intensity during experiments. After that, the beam should be sent through the 20 cm-long magnet. A pair of 1 mm-diameter help-pieces is installed at the entrance and the exit position of the magnet to determine the deflection area. Finally, the chopper is inserted and aligned using a focused laser beam sent from the ionization window to the nozzle. Since the actual size of the uniform gradient is smaller than the diameter of the help-pieces, further fine-alignments need to be done based on the recorded deflection during magnetic deflection experiments (as discussed in Section 7.3.3).

As discussed in Section 7.1.5, a small angle α between the extraction optics and the reflectron gives rise to a non-zero v_z value. Therefore, close attention must be paid for aligning the extraction optics and the reflectrons. One should keep in mind that only if α is zero, the clusters will leave the reflectron at the same position regardless of their velocities. By tilting the extraction optics and/or the reflectron until the recorded beam position does not depend on the extraction voltage, α will approach zero. For simplicity, the alignment is done with each reflectron in turn.

7.3 First results

In this section, we report preliminary tests performed with the magnetic deflection setup. Clusters are produced, velocity-selected, collimated, and time-resolved position-sensitive detected in the HRTOF. The magnetic deflections of Cr atoms are measured. The three objectives of the new instrument, as outlined in section 7.1.6, are realized.

7.3.1 Time-resolved position-sensitive measurements

As discussed in Section 7.1.1, it is important to maintain the intrinsic mass resolution of the TOF during position-sensitive measurements. The Leuven magnetic deflection setup uses a position-sensitive detector to simultaneously record the time and position information of clusters. The performance of the position-sensitive detector was characterized by tests on different species, such as vanadium oxide clusters, gold oxide clusters, cobalt oxide clusters, and silver clusters.

First, we discuss the performance of the position-sensitive detector in terms of mass resolution. Figure 7.22 shows a typical mass spectrum of neutral V_nO_m clusters (top) and a zoom of the signal for V_5O. To form oxide species, we used the high-purity helium backing gas mixed with 1% oxygen. The neutral clusters travel about 1.8 m before being ionized in the center of the extraction. The ionized clusters are accelerated orthogonally into the TOF chamber by a voltage pulse of 5 kV on the extraction plate. In the TOF chamber, the clusters are reflected by the first and reach the position-sensitive detector mounted at the position of the second reflection. For a given angle of the extraction optics,

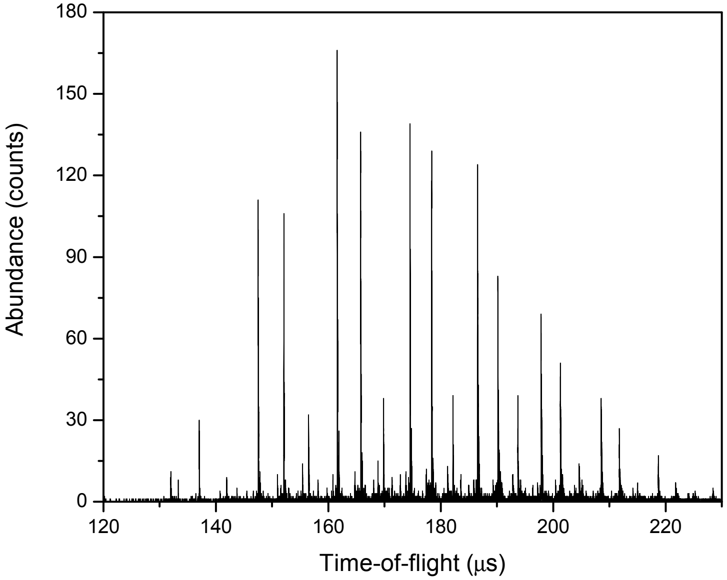

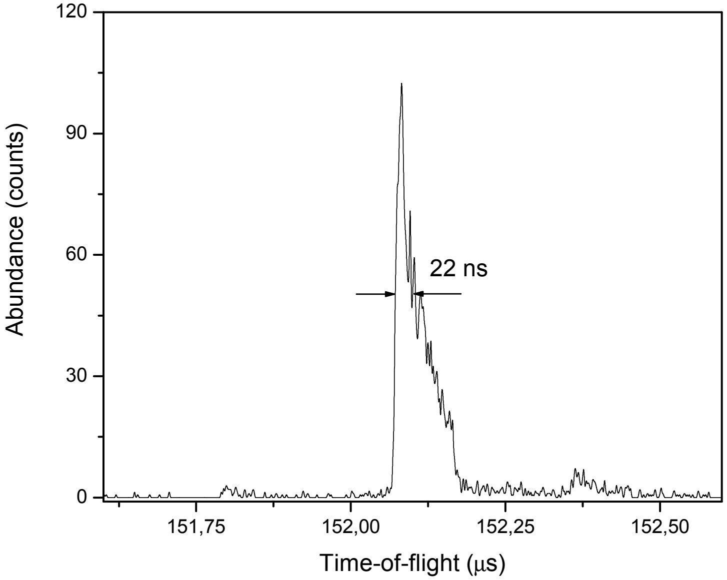

Figure 7.22: *(Top) Mass spectrum of vanadium oxide clusters (V_nO_m; $n = 4-11$, $m = 1-5$) recorded by the position-sensitive detector. (Bottom) Detail of the V_5O peak showing a mass resolution of about 3400.*

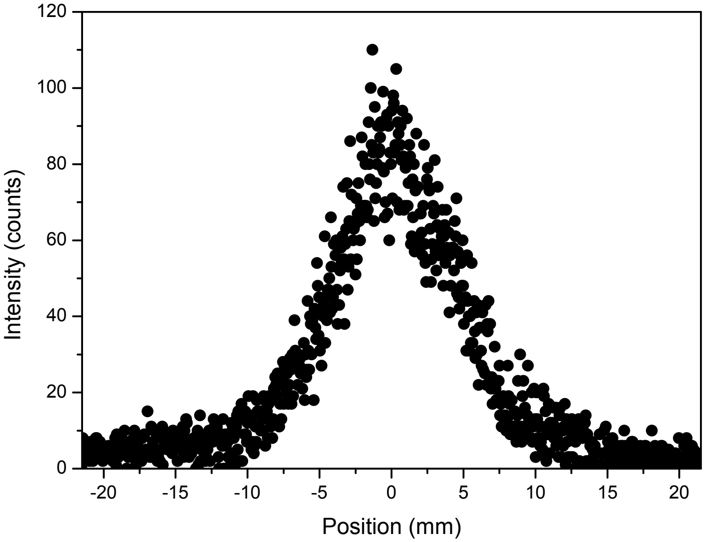

Figure 7.23: *A typical position-sensitive spectrum of* V_nO_m *clusters.*

only a given mass range is observable. To see larger clusters, the extraction plate needs to be tilted. The mass range measured with the position-sensitive detector is about 500 amu. The mass resolution achieved from this spectrum is about 3400, which is similar to what we have discussed in Section 2.1.3.

The corresponding position-sensitive spectrum of $\mathrm{V}_n\mathrm{O}_m$ clusters along the deflection direction is shown in Fig. 7.23. The ionization energy is 0.5 mJpp@157 nm. The width of the cluster beam is about 9.5 mm. Although the spectrum is recorded without the beam collimators, the beam width is still limited by the pole gap (6 mm) of the magnet before reaching the extraction. Data are collected during 3000 cycles over 1024 delay-line channels of the detector (corresponding to an active area of 43 mm). The position-sensitive resolution is 0.042 mm (as discussed in section 7.2.7).

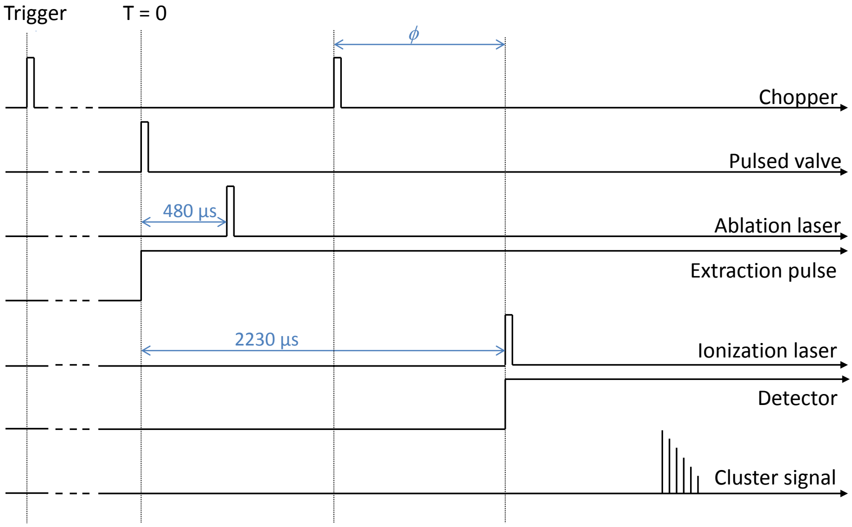

Figure 7.24: *Typical schematic diagram describing the relative timing for velocity-selective experiments.*

7.3.2 Velocity measurement

The magnetic deflection experiments require an accurate measurement of the velocity and a limited velocity spread since the magnitude of the magnetic deflection depends on the velocity squared (Eq. 1.10). Details about the chopper are described in section 7.2.3. The chopper can operate at a frequency of either 100 Hz or 200 Hz. In the velocity-selective mode, the output reference signal from the chopper is used to trigger the cluster production, that way synchronizing the chopper rotation with the setup timing.

Figure 7.24 shows a typical example of the relative time sequence for velocity-selected experiments. The chopping frequency is 100 Hz. A frequency divider is employed to reduce the output frequency of the chopper to 10 Hz, which is then used to trigger the setup. Following the trigger from the chopper, the pulsed valve is opened as the first event in the time sequence. A Nd:YAG laser ablates the target at about 480 μs after the first event. The photoionization laser is triggered about 2230 μs after opening the pulsed valve to ionize the

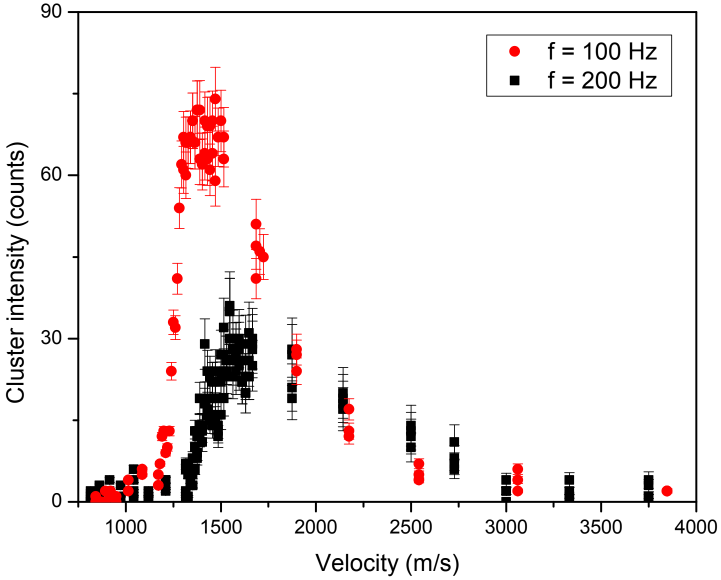

Figure 7.25: *Typical velocity distribution of Pb clusters measured at chopping frequencies of 100 Hz and 200 Hz.*

velocity-selected clusters. The ionization time can be varied between 900 and 2800 μs, depending on the ablation time and the cluster size range of interest. The extraction electrodes provide a constant field to select neutral clusters only. Finally, the position-sensitive detector is externally triggered at the same time as the ionization. The arrival time and position of the velocity-selected clusters are recorded. In the velocity-selective measurements, the ablation time and ionization time are fixed. By changing the relative time ϕ between the opening of the chopper and the triggering of the ionization laser, the cluster velocity is determined.

Figure 7.25 presents typical velocity distributions of Pb clusters with respect to the velocity measured at chopping frequencies of 100 Hz and 200 Hz. The data are collected from three independent sets. For each measurement, the signal is accumulated in 3000 cycles. For both configurations, clusters have a velocity spread from about 1200 to 3000 m/s. Most of the clusters travel at about 1400-1700 m/s. The differences (intensity and lower limit) of velocity distributions at 100 Hz and 200 Hz mainly come from the longer opening time of the chopper at 100 Hz (184 μs) compared to that at 200 Hz (84 μs). These opening times also result in a velocity uncertainty, which decreases with decreasing the cluster velocity. A typical uncertainty for a velocity of 1600 m/s and a chopping frequency of 200 Hz is ±68 m/s.

7.3.3 First results: magnetic deflection of Cr atoms

Following the tests on the position-sensitive detection and velocity selection, the first magnetic deflection experiments are performed. The main purposes of these experiments are i) to calibrate the field gradient of the actual magnet and ii) to give a proof of principle of the instrument. We chose Pb and Cr atoms as test objects because of the following reasons: the total magnetic moment of the Pb atom is zero ($^3P_0$) while the Cr atom has a high total magnetic moment ($^7S_3$); in addition, the ionization energies of Pb (7.4 eV) and Cr atoms (6.67 eV) are lower than the photon energy of the F_2 excimer laser (7.9 eV).

These atoms are light, and they are accelerated nearly perpendicular into the HRTOF chamber, which results in a serious reduction of the signal intensity detected at the final position. Moreover, the influence of the extraction and reflectron grids on the beam broadening can be negligible for large cluster sizes but is considerable for atoms, especially for Cr atoms (cfr. Eq. 7.19). Therefore, the position-sensitive measurement of Pb and Cr atoms is performed at the linear position (the red part in Fig. 7.12) to maximize the signal and to avoid the broadening effect of the grids in the reflectrons.

Table 7.7: *Calculated deviations of Pb and Cr atoms due the electrostatic field of the extraction grids (cfr. Eq. 7.19). The distance from the center of the extraction optics to the detector is 2.5 m.*

Parameters	Pb atom	Cr atom
G	0.144	0.144
g (mm)	0.112	0.112
$\lvert q\Delta E\rvert$ (eV/mm)	167	167
m (kg)	3.42×10^{-25}	8.26×10^{-26}
time-of-flight (μs)	46.64	24.70
v_y (mm/μs)	53.6	101.2
deviation (mm)	1.10	1.27

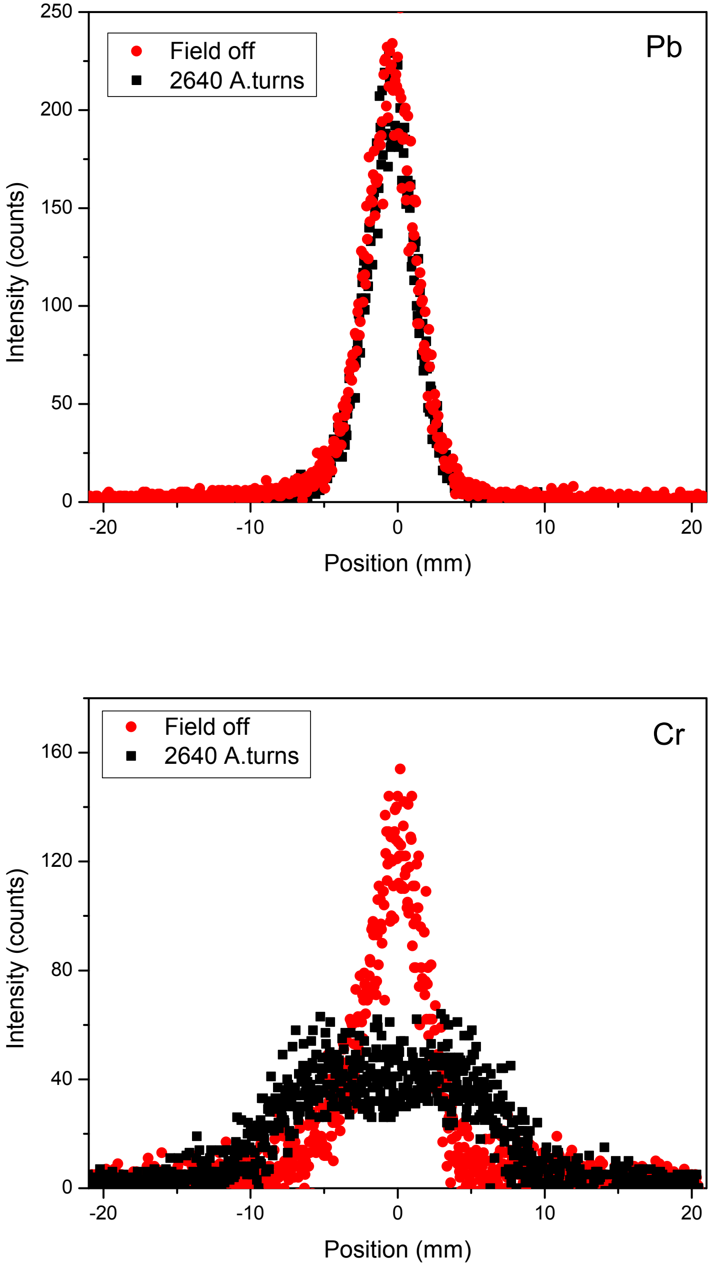

Figure 7.26: *Position-sensitive measurements of Pb (top) and Cr atoms (bottom) at 2640 A·turns: a magnetic deflection is observed for Cr atoms while the magnetic field shows no influence on Pb atoms.*

Pb and Cr atoms are produced in the cluster source and velocity-selected by a chopping frequency of 200 Hz. The velocity of atoms is selected at 1600 m/s to maximize the recorded signal. The atom beam is then collimated with a cross-section of 0.3 mm by 3.0 mm (the first dimension along the deflection direction). The beam travels 1.1 m from the second collimator to the center of the extraction, where it is ionized by the 157 nm excimer laser with a fluence of 1 $\mathrm{mJ/cm^2}$. The beam width at the center of the extraction is estimated to be about 1.2 mm (corresponding to a skimmer-slit distance of 0.5 m, cfr. Table 7.4). It should be mentioned that a fine-alignment is needed to assure that the beam passes through the homogeneous area of the field gradient. For this reason, the magnetic deflection experiments are performed with the beam scanned in the deflection direction. The incident beam is shifted by shifting the opening window of the collimators. In practice, the beam is swept with steps of 0.05 mm until a symmetric deflection is achieved.

Figure 7.26 presents the position-sensitive spectra of Pb (top) and Cr atoms (bottom), respectively, with a current through the electromagnet of 0 (field off) and 2640 A·turns (field on). While the magnetic field shows no influence on Pb atoms, Cr atoms are symmetrically deflected. The deflection of the Cr atoms is expected to split up in seven beamlets according to J_z (projections of J on the z axis) but the current resolution (the intrinsic width of the atom beam) does not allow to separate these. The strongest deflection of the Cr atoms measured with 2640 A·turns is 7.2±0.1 mm. The beam widths of Pb and Cr atom signals (with the field off) are 3.2 mm and 3.7 mm, respectively. This broadening is essentially due to the electrostatic effect of the extraction grids, which is larger for lighter atoms. Using Eq. 7.19, deviations of Pb and Cr are calculated and shown in Table 7.7. The influence of the extraction grids on the beam-width broadening is stronger for Cr than for Pb atoms. Taking the effect of the extraction grids into account, the estimated beam widths of Pb (the intrinsic peak width is 1.2 mm and the width broadening is 1.10 mm) and Cr atoms (the intrinsic peak width is 1.2 mm and the width broadening is 1.27 mm) are in good agreement with our observation.

The deflection of Cr atoms is further measured at different applied currents for the gradient calibration. Figure 7.27 illustrates the evolution of the deflection as a function of the applied current (magnetic field). It can be clearly observed that the deflection increases with increase of the current. A fitting procedure is applied to extract the field gradient from the measured deflections. For this purpose, Eq. 1.10 can be written as:

$$\frac{dB}{dz} = \frac{2dmv^2}{(L^2 + 2LD)\langle\mu_z\rangle} \tag{7.20}$$

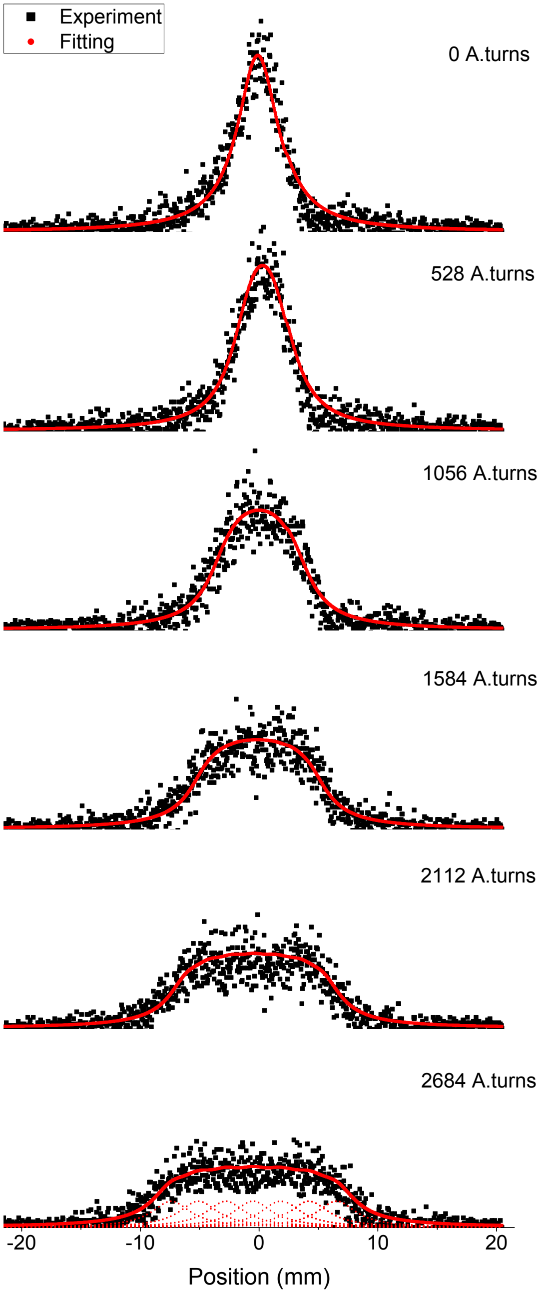

Figure 7.27: *Evolution of the magnetic deflection of Cr atoms as a function of the applied current through the electromagnet. The black squares are experimental results and the red circles are fitting data. Seven beamlets (red dotted lines) that add up to the total fitting deflection pattern are shown for the current of 2684 A.turns. All measurements are plotted in the same scale.*

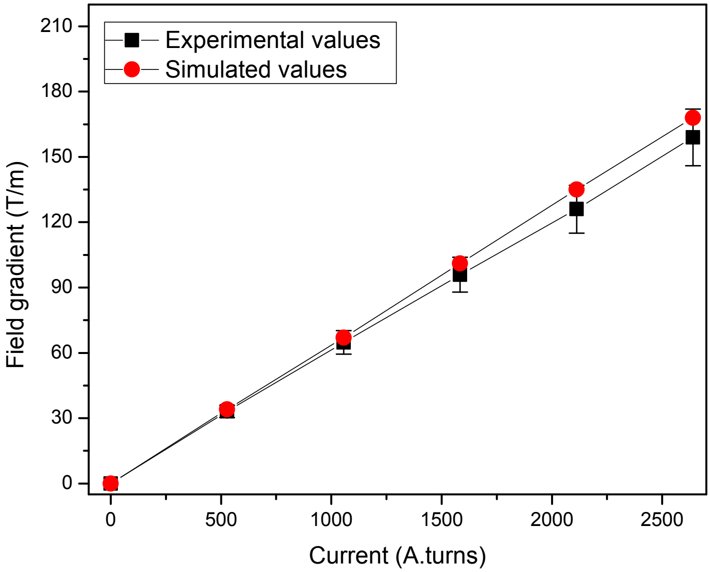

Figure 7.28: *Comparison between the simulated and experimental values (via Eq. 7.20) of the field gradient with respect to applied currents through the electromagnet.*

where $\langle \mu_z \rangle = g_J J_z \mu_B$ with g_J the Landé factor and μ_B the Bohr magneton. $J_z = 0$ for the Pb atom and -3,-2,-1,0,1,2,3 for the Cr atom. The deflection d is retrieved using a deconvolution process. By inserting the instrumental parameters ($L = 0.2$ m and $D = 0.8$ m), the mass and velocity of the atoms ($m_{Cr} = 8.26 \times 10^{-26}$ and $v = 1600 \pm 68$ m/s), and the measured deflection d in Eq. 7.20, the field gradient can be experimentally determined.

The experimentally obtained and simulated gradients are plotted in Fig. 7.28. Table 7.8 gives the fitting results compared to the simulated data. In good agreement with the simulation, a linear behavior of the field gradient is observed from 0 to 2640 A·turns. The simulated values of the field gradient are the same within the accuracy with those deduced from the experiments. At a current of 2640 A·turns, the simulated gradient is 168 T/m while the calibrated value is 159±13 T/m, which corresponds to an instrumental strength K of 57±5 Tm. The error values result mainly from the uncertainty of the velocity measurement.

To reduce this factor, the speed of the clusters and/or the opening time of the chopper should be reduced.

7.4 Conclusions

A novel magnetic deflection setup was designed and implemented in the KU Leuven cluster laboratory. Preliminary tests were performed to characterize the main features and to demonstrate the proof of principle of the setup. Three criteria were realized:

- The design is compatible with the Leuven cluster source.
- The magnetic deflection setup is coupled to the HRTOF with a position-sensitive detector to simultaneously measure the time (mass) and position (magnetism) information of clusters.
- The instrumental parameter K is up to 57±5 Tm.

Magnetic deflection experiments were successfully carried out using atomic beams of Cr and Pb. The symmetric magnetic deflection of Cr atoms was clearly observed as a function of increasing the magnetic field gradient, showing a good agreement with simulations.

At the current stage, the initial requirement for an instrumental strength K of 100 Tm has not yet been reached. Meanwhile, a new pair of magnet poles is already designed, fabricated and is ready to be installed. With this new design of magnet poles, the instrumental strength parameter of the Leuven magnetic

Table 7.8: *Experimental determination of the field gradient based on the magnetic deflection of Cr atoms.*

Current (A·turns)	Maximal deflection (mm)	Experimental gradient (T/m)	Simulated gradient (T/m)
0	0±0.1	0±1	0
528	1.5±0.1	33±3	34.0
1056	2.9±0.1	65±6	67.0
1584	4.4±0.1	96±8	101.0
2112	5.7±0.1	127±11	135.0
2640	7.2±0.1	159±13	168.0

deflection setup will be increased up to a value of 150 Tm. These new magnet poles will be installed in the near future but this must be carried out with great care since the area of the uniform gradient is even smaller than that of the current set of magnet poles. Another effort will be to check whether the beam widening effect of the extraction grids will be smaller for larger sizes as predicted. For experiments where high mass-resolution is not vital, the use of single reflectron stage might be more practical.

It will be more efficient for magnetic deflection if positions of different arrival times (corresponding to different cluster sizes) can be measured simultaneously. For this purpose, a (home-made) labview programme will be needed to inspect and analyze the data directly from the detector readout. There is also a need for performing temperature-dependent measurements by upgrading the cluster source with a cryogenic cooling system.

Nevertheless, there is no reason to wait for these above upgrades as the instrument is ready for observing new experimental output. The deflection measurements on clusters might already be realized during the submission of this thesis.

References

1. D. M. Cox, D. J. Trevor, R. L. Whetten, E. A. Rohlfing, and A. Kaldor, Phys. Rev. B **32**, 7290 (1985).
2. W. A. de Heer and P. Milani, Rev. Sci. Instrum. **62**, 670 (1991).
3. J. P. Bucher, D. C. Douglass, and L. A. Bloomfield, Phys. Rev. Lett. **66**, 3052 (1991).
4. T. Hihara, S. Pokrant, and J. A. Becker, Chem. Phys. Lett. **294**, 357 (1998).
5. M. B. Knickelbein, Phys. Rev. Lett. **86**, 5255 (2001).
6. U. Rohrmann, S. Schäfer, and R. Schäfer, J. Phys. Chem. A **113**, 12115 (2009).
7. X. Xu, *The magnetism of free cobalt clusters measured in molecular beams*, PhD thesis (Georgia Institute of Technology, Georgia, 2007).
8. M. B. Knickelbein, Phys. Rev. B **75**, 014401 (2007).
9. W. Gerlach and O. Stern, Z. Phys. **9**, 353 (1922).

10. I. I. Rabi and V. W. Cohen, Phys. Rev. **43**, 582 (1933).
11. PHYWE, *Physics laboratory experiments*, (PHYWE SYSTEME GMBH, Gottingen, 2008).
12. D. McColm, Rev. Sci. Instrum. **37**, 1115 (1966).
13. B. Masschaele, T. Roggen, H. De Gersem, E. Jansens, and T. T. Nguyen, IEEE Trans. Appl. Superconduct. **22**, 3700604 (2012).
14. D. Meeker, FEMM: Finite Element Method Magnetics, [Online]. Available: http://www.femm.info /wiki/HomePage.
15. CST: Computer Simulation Technology [Online]. Available: http://www.cst.com (accessed: January, 2011).
16. B. Masschaele, internal report on January 13, 2011.
17. T-FLEX: Mechanical 2D and 3D Parametric Design Solutions [Online]. Available: http://www.tflex.com.
18. W. A. de Heer, P. Milani, and A. Chatelain, Phys. Rev. Lett. **65**, 488 (1990).
19. M. B. Knickelbein, J. Chem. Phys. **115**, 5957 (2001).
20. I. M. L. Billas, J. A. Becker, A. Chatelain, and W. A. de Heer, Phys. Rev. Lett. **71**, 4067 (1993).
21. S. Bouneau, P. Cohen, S. Della Negra, D. Jacquet, Y. Le Beyec, J. Le Bris, M. Pautrat, and R. Sellem, Rev. Sci. Instrum. **74**, 57 (2003).
22. J. Rius i Riu, M. Stankiewicz, A. Karawajczyk, and P. Winiarczyk, Nucl. Instr. Meth. Phys. Res. A **477**, 360 (2002).
23. M. Abd El Rahim, R. Antonie, L. Arnauld, M. Barbaire, M. Broyer, Ch. Clavier, I. Compagnon, Ph. Dogourd, J. Maurelli, and D. Rayane, Rev. Sci. Instrum. **75**, 5221 (2004).
24. J. De Haeck, *Mass spectrometric developments and a study of lithium doped silicon and germanium clusters*, PhD thesis (KU Leuven, Leuven, 2011).
25. T. Bergmann, T. P. Martin, and H. Schaber, Rev. Sci. Instrum. **60**, 347 (1989).
26. Scitec Instrument 300CD Manual.
27. B. Masschaele, internal report on March 15, 2011.

28. B. Masschaele and H. De Gersem, internal report on April 4, 2011.

29. S. Vandezande, P. Mispelter, and E. Janssens, internal report on August 22, 2012.

30. Surface Concept 1D-DLD43 Manual.

Chapter 8

General conclusions and perspectives

One of the long-term goals of cluster science research is to synthesize chemically inert, particularly stable cluster species with specific properties that can be used as advanced materials in nanotechnology applications. Bimetallic clusters are promising as building blocks of these advanced materials, since they offer possibilities to engineer their stability, magnetism, and other properties by manipulating size, shape, and composition. In this regard, numerous studies of (transition) metal doped simple metal clusters as a function of size and composition have provided a wealth of data with wide-ranging interest in various areas of physics and chemistry. Nevertheless, a more challenging question, that is how the cluster stability and magnetism develop in more complex systems, such as transition metal doped transition metal clusters, has not been well understood. This thesis work intends to provide a better understanding of such questions.

8.1 Bimetallic cluster stability

Inheriting the success of the recent development of the high resolution time-of-flight mass spectrometer, the first goal of this thesis is to provide new experimental insights in the stability of binary (transition) metal clusters using the mass-selective photofragmentation technique.

We studied bimetallic (Pb_nAl^+, Co_nTM^+, with $n = 7 - 18$ and TM = Ti, V, Cr, Mn) and bimetallic oxide ($Co_{n-1}CrO_m^+$ with $n = 1 - 4$ and $m = 2 - 8$) clusters experimentally using photofragmentation mass spectrometry and investigated some selected species computationally by density-functional theory. The size- and composition-dependent cluster properties, more in particular the dissociation behavior, stability, structure, and bond strength are investigated. Relative stabilities of the clusters are extracted from the size-dependent photofragmentation spectra. Constraints imposed by the statistical model combined with the available measured laser fluence-dependent photofragmentation spectra are used to bracket dissociation energies. Cluster structures and dissociation energies of some selected sizes are calculated for comparison.

The main conclusions of this study are:

- The relative stability and dissociation behavior of bimetallic clusters are dopant-dependent and generally governed by dimer binding energies.
- Exceptionally stable 13-atom clusters can be created by introducing an appropriate dopant atom.

In particular, the smallest Pb_nAl^+ ($n = 7 - 11$) clusters favor atomic Pb evaporation, whereas the preferred dissociation pathway of the larger ones ($n = 12 - 16$) involves Pb_2 and Pb_3 fragments. $Pb_{10}Al^+$ and $Pb_{12}Al^+$ are produced as the fragments of all larger clusters. The measured laser fluence dependence of the fragment intensities implies that the primary fragments are produced from single absorption processes for both 532 nm and 355 nm laser light.

For Co_nTM^+ clusters, the measured laser fluence dependence of the fragment intensities shows that multi-photon absorption processes are likely to take place for 532 nm laser light. The evaporation of a Co atom is the most facile dissociation channel for Ti and V doped species. In contrast, for TM = Cr and Mn the split-off of the dopant atom is seen to be the preferred dissociation channel with an exception for $Co_{13}Cr^+$. It is suggested that Ti and V substitutions enhance the stability of Co clusters whereas Co_nCr^+ and Co_nMn^+ clusters are less stable than the Co_{n+1}^+ counterparts. The dopant-dependent relative stabilities of Co_nTM^+ clusters can be explained by the relative binding energies of Co−TM.

For $\mathrm{Co}_n\mathrm{O}_m^+$ and $\mathrm{Co}_{n-1}\mathrm{CrO}_m^+$ ($n = 2, 3$; $m = 2 - 6$ and $n = 4$; $m = 3 - 8$), substitution of a Co by a Cr atom alters the dissociation behavior. Pure cobalt oxide clusters with a high oxygen content favor splitting off molecular oxygen if $m \geq n + 1$ for $n = 2, 3$ and $m \geq n$ for $n = 4$. Clusters with a lower oxygen content prefer to evaporate atomic oxygen. For chromium doped species, $[\mathrm{O}_2]$ unit evaporation is found to be the only lowest energy dissociation channel for all clusters, except for CoCrO_2^+ and CoCrO_3^+. Most oxide species have structures in which the number of metal-oxygen bonds is maximized. The influence of the dopant atom is strongest for CoCrO_3^+, $\mathrm{Co}_2\mathrm{CrO}_2^+$, $\mathrm{Co}_2\mathrm{CrO}_4^+$, and $\mathrm{Co}_3\mathrm{CrO}_4^+$, suggesting a different growth mechanism compared with the undoped cobalt oxide clusters. These structural changes are supported by corresponding changes in their dissociation behavior. Detailed comparison between experimental dissociation and computational data shows that $\mathrm{Co}_2\mathrm{O}_2^+$, CoCrO_2^+, $\mathrm{Co}_4\mathrm{O}_3^+$, and $\mathrm{Co}_4\mathrm{O}_4^+$ are particularly stable.

It is interesting that the stabilities of 13-atom species are significantly enhanced by a proper dopant atom. The frequent appearance of $\mathrm{Pb}_{12}\mathrm{Al}^+$ as the fragment of larger clusters suggests its high stability. Moreover, the dissociation energy of $\mathrm{Pb}_{12}\mathrm{Al}^+$ is considerably higher than that of the neighboring cluster sizes. Exceptional fragmentation behavior of $\mathrm{Co}_{13}\mathrm{Cr}^+$ among $\mathrm{Co}_n\mathrm{Cr}^+$, which prefers dissociating via loss of a Co atom rather than via loss of a Cr atom, suggests an enhanced stability of the $\mathrm{Co}_{12}\mathrm{Cr}^+$ over Co_{13}^+. The laser fluence dependence of the fragment intensities indicates that $\mathrm{Co}_{12}\mathrm{V}^+$ is the most stable system among the singly TM doped clusters. A significant enhancement of the stability is found when substituting one Co atom by a V atom in Co_{13}^+.

8.2 Development of a Stern-Gerlach magnetic deflection setup

The magnetism of free clusters has been investigated essentially using the Stern-Gerlach magnetic deflection technique. Nevertheless, only a few setups have been developed so far with challenges in studying magnetic properties of bimetallic clusters. The second goal of this thesis is devoted to develop a new Stern-Gerlach magnetic deflection setup. By using a unique combination of a binary cluster source, a magnetic deflection system, and a time-resolved position-sensitive detector, it is possible to measure the magnetic deflection of bimetallic clusters.

Extensive simulations are performed to obtain detailed information about the magnetic deflector, intrinsic beam width, and beam deflection. Based on this, the requirements for the Leuven magnetic deflection setup were defined. The design had to be compatible with the Leuven cluster source. The use of the dual-target dual-laser vaporization source is an advantage over the existing setups for studying magnetic properties of binary species. To maintain the intrinsic mass resolution during position-sensitive measurements, the Leuven magnetic deflection system is coupled to the HRTOF mass spectrometer, where the time (mass) and position (magnetism) information is measured simultaneously by a position-sensitive detector. The setup was designed in such an open way that the deflection strength K can be improved subsequently for different cluster systems.

A number of experimental tests were performed to characterize the instrument. Clusters were produced in the Leuven cluster source, traveled through a 7.5-m long flight path to be detected by the position-senstivie detector. The cluster velocity was measured with an uncertainty of about 4 %. The magnetic deflection of Cr atoms was measured successfully. The three objectives of the new setup are realized. The current instrumental strength K is 57±5 Tm, which allows to measure the magnetic deflection of small clusters. This parameter can be improved by a new set of magnet poles, that is designed to increase the field gradient up to 400 T/m (with K of 140 Tm). Given the success in design and realization of the current Rabi poles, achieving a deflection strength K above 150 Tm with the new pole set is straightforward. This will allow the instrument to probe the magnetism of cluster systems with a small magnetic moment/mass ratio.

8.3 General conclusions and outlook

Throughout this thesis we have contributed to the state-of-the-art of cluster science in a number of ways:

- Investigation of the stability, dissociation behavior, bonding, and possible structure of complex bimetallic clusters by means of mass-selective photofragmentation experiments.
- Examination and demonstration of the enhancement of the cluster stability by doping.
- Development of a new magnetic deflection setup, which is able to measure the magnetic properties of binary cluster species in the gas phase with a high deflection sensitivity and a high mass resolution at the same time.

When looking to the future, each part of this work offers promising possibilities for further research. The enhanced stability of 13-atom species corroborates the theoretical prediction: a structural transformation to the stable icosahedron can be triggered by introducing an appropriate dopant atom in the center of the host clusters. The investigations of the size- and dopant-dependent stability can be extended to other transition metal clusters using the mass-selective photofragmentation technique in combination with the unimolecular decay theory. The dissociation energies and geometrical structures can be further explored by density functional theory. This will give a comprehensive picture of the exceptional stability of 13-atom species, which are very important input for magnetic deflection experiments.

The development of the Leuven magnetic deflection setup offers new possibilities for studying magnetism of binary clusters. For example, the interaction of magnetic impurities with normal metals in the ultimate small size limit can be probed by studying the magnetism of neutral noble metal clusters doped with a single magnetic atom with magnetic deflection experiments. This will allow to trace the occurrence of the Kondo effect in a range from a few up to several tens of atoms, and, in particular, to detect the smallest size from where it shows up. That size then implicitly defines a lower limit for the extent of the Kondo cloud. On the other hand, interesting size specific (opto-) electronic and magnetic properties may emerge both for silicon and germanium, by proper metal atom doping, in particular for magnetic dopant atoms such as Co, Cr, and Mn. Recent predictions have shown that metal-encapsulated stable tubular silicon and germanium clusters can serve as building blocks of nanotubes. Using magnetic atoms, such systems would form the ultimate one-dimensional magnetic nanowire. Therefore, it would be interesting to study the evolution with size of the magnetism of tubular species with one-atom Co, Cr, and Mn encapsulated nanowires.

The ongoing trend towards miniaturization of technological components has motivated envisaging the use of smaller and smaller nanoparticles as functional building blocks for new nanostructured materials. Bimetallic clusters are well suited for this purpose and the quest for particularly stable bimetallic cluster species with specific properties therefore becomes a long sought-after goal of cluster science. In this regard, the stability studies of bimetallic clusters and the development of a new magnetic deflection setup can serve as a solid step toward the in-depth understanding of the evolution of cluster properties as well as the perspective of novel nanostructured materials.

List of publications

PUBLICATIONS RELATED TO THE THESIS SCOPE

- **Design of a strong gradient magnet for the deflection of nanoclusters**
B. Masschaele, T. Roggen, H. De Gersem, E. Janssens, and N. T. Tung
IEEE Transactions on Applied Superconductivity **22**, 3700604 (2012).

- **Mass-selected photofragmentation studies of $\mathbf{AlPb}_n^+$ clusters: Evidence for the extraordinary stability of $\mathbf{AlPb}_{10}^+$ and $\mathbf{AlPb}_{12}^+$**
S. Bhattacharyya, N. T. Tung, J. De Haeck, K. Hansen, P. Lievens, and E. Janssens,
Physical Review B **87**, 054103 (2013).

- **Photofragmentation of mass-selected vanadium doped cobalt cluster cations**
N. T. Tung, E. Janssens, S. Bhattacharyya, and P. Lievens
European Physical Journal D **67**, 41 (2013).

- **Improved field post-processing for a Stern-Gerlach magnetic deflection magnet**
H. De Gersem, B. Masschaele, T. Roggen, E. Janssens, N.T. Tung
Int. J. Num. Model. **27**, 472 (2014).

- **Dopant dependent stability of transition metal doped cobalt cluster cations**
N. T. Tung, E. Janssens, and P. Lievens
Applied Physics B **114**, 497 (2014).

- **Influence of Cr doping on the stability of $\mathbf{Co}_n\mathbf{CrO}_m^+$ clusters**

N. T. Tung, N. M. Tam, M. T. Nguyen, E. Janssens, and P. Lievens
submittted.

OTHER PUBLICATIONS

- **Triple negative-permeability in hybridized cut-wire-pair metamaterials**
V. T. T. Thuy, D. T. Viet, N. V. Hieu, V. D. Lam, Y. P. Lee, and N. T. Tung
Optics Communications **283**, 4303 (2010).

- **Quasi-dark mode in a metamaterial for analogous electromagnetically-induced transparency**
V. T. T. Thuy, N. T. Tung, J. W. Park, Y. H. Lu, J. Y. Rhee, and Y. P. Lee
Journal of Optics **12**, 115102 (2010).

- **Strong tie between cut-wire pair and continuous wires in combined structure**
J. W. Park, N. T. Tung, V. T. Thuy, V. D. Lam, and Y. P. Lee
Optics Communications **284**, 919 (2011).

- **Comment on "Antisymmetric resonant mode and negative refraction in double-ring resonators under normal-to-plane incidence"**
N. T. Tung
Physical Review E **83**, 038601 (2011).

- **Characterization and electromagnetic response of a phi-shaped metamaterial**
N. T. Tung, J. W. Park, V. T. T. Thuy, P. Lievens, Y. P. Lee, and V. D. Lam
European Physical Journal B **81**, 263 (2011).

- **Computational studies of a cut-wire pair and combined metamaterials**
N. T. Tung, P. Lievens, Y. P. Lee and V. D. Lam
Advances in Natural Sciences: Nanoscience and Nanotechnology **2**, 033001 (2011).

- **Broadband negative permeability by hybridized cut-wire pair metamaterials**
N. T. Tung, D. T. Viet, B. S. Tung, N. V. Hieu, P. Lievens, and V. D. Lam
Applied Physics Express **5**, 112001 (2012).

- **Thermally tunable magnetic metamaterial at THz frequencies**
B. S. Tung, N. V. Dung, B. X. Khuyen, N. T. Tung, P. Lievens, Y. P. Lee, and V. D. Lam
Journal of Optics **15**, 075101 (2013).

SCIENTIFIC CONFERENCE/SCHOOL CONTRIBUTIONS

- **Left-handed transmission in simple cut-wire pair metamaterials**
N. T. Tung
European School on Nanosciences and Nanotechnologies 2010
August 22-September 11, 2010, Grenoble, France.

- **Title left-handed behavior by multiple-plasmon resonances in single-atom metamaterials**
N. T. Tung, P. Lievens, and V. D. Lam
The 5th International Workshop on Advanced Materials Science and Technology
November 9-12, 2010, Hanoi, Vietnam.

- **Photofragmentation of mass-selected vanadium doped cobalt cation clusters**
N. T. Tung, E. Janssens, B. Soumen, J. De Haeck, and P. Lievens
The 16th International Symposium on Small Particles and Inorganic Clusters ISSPIC XVI
July 8-13, 2012, Leuven, Belgium.

- **Photofragmentation of mass-selected cobalt oxide cation clusters**
N. T. Tung, E. Janssens, and P. Lievens
The 6th International Workshop on Advanced Material Science and Nanotechnology
October 30- November 3, 2012, Ha Long, Vietnam.

- **Broadband negative permeability using hybridized metamaterials**
N. T. Tung, D. T. Viet, B. S. Tung, N. V. Hieu, P. Lievens, and V. D. Lam
The 6th International Workshop on Advanced Material Science and Nanotechnology
October 30- November 3, 2012, Ha Long, Vietnam.

- **Influence of dopant Cr atom on the dissociation behavior and relative stability of bimetallic oxide clusters $\mathbf{CoCrO}_m^+$**

N. T. Tung, E. Janssens, N. M. Tam, N. M. Tho, and P. Lievens
Symposium on Size Selected Clusters 2013
Mar 3-8, 2013, Davos, Switzerland.

Curriculum vitae

Nguyen Thanh **TUNG**

- **1983, August 18** Born in Hanoi, Vietnam

- **2001-2006** Bachelor in Engineering Physics
Hanoi University of Science and Technology, Vietnam

- **2007-2009** Master in Physics
Hanyang University, South of Korea

- **2010-2014** Ph.D. candidate in Physics
KU Leuven, Belgium

FACULTY OF SCIENCES
DEPARTMENT OF PHYSICS AND ASTRONOMY
CLUSTERS AND LASER SPECTROSCOPY
Geel Huis, Kasteelpark Arenberg 11 - bus 2100
3001 Leuven
thanhtung.nguyen@fys.kuleuven.be
http://www.fys.kuleuven.be/class